Investigation of all-flavour neutrino fluxes with the IceCube detector using the cascade signature

D I S S E R T A T I O N

zur Erlangung des akademischen Grades

doctor rerum naturalium
(Dr. rer. nat.)
im Fach Physik

eingereicht an der
Mathematisch-Naturwissenschaftlichen Fakultät
der Humboldt-Universität zu Berlin

von
Dipl.-Phys. Arne Schönwald

Präsident der der Humboldt-Universität zu Berlin:
Prof. Dr. Jan-Hendrik Olbertz

Dekan der Mathematisch-Naturwissenschaftlichen Fakultät:
Prof. Dr. Elmar Kulke

Gutachter:
1. Prof. Dr. Hermann Kolanoski
2. Prof. Dr. Marek Kowalski
3. Prof. Dr. Sebastian Böser

Tag der mündlichen Prüfung: 18.12.2015

Abstract

This thesis presents a search for the diffuse astrophysical neutrino flux in 335 days of IceCube data. IceCube is a 1 km^3 neutrino detector located at the South Pole, consisting of 86 strings, each equipped with 60 Digital Optical Photomultipliers (DOMs), frozen in the ice. The detector was still in construction when the data used in this analysis was taken, therefore only 59 strings were available (IC59).
The analysis presented here is sensitive to all three neutrino flavors. Neutrinos interacting with nuclei in the ice produce charged particles which emit Cherenkov light. This light is recorded by the DOMs and used for the event reconstruction. These neutrino events must be extracted from the huge background of atmospheric muons, which is 10^8 times more common than neutrino events at trigger level. Finally, atmospheric and astrophysical neutrinos need to be distinguished statistically, based on the reconstructed neutrino energies.
To obtain a robust prediction of atmospheric muon events at the final level of the event selection, a huge simulation sample of atmospheric muons has been produced. This analysis was the first to achieve a livetime of more than one year of simulated atmospheric muon events with $E \geq 10$ TeV.
A first analysis counting the number of events with an energy $E > 38$ TeV found 8 events with energies between 39 TeV and 67 TeV for a background prediction of 3.6 ± 0.3 events. This excess was further investigated with a maximum likelihood fit with an energy threshold of 10 TeV. No astrophysical neutrino flux was required to describe the excess in the data. Instead, it was absorbed by a higher normalization of the atmospheric neutrino flux. If no constraints from independent measurements or models of the atmospheric neutrino flux are applied, a 90% upper limit on the all-flavor astrophysical neutrino flux of $E^2\Phi_{astro,\,ul} = 1.7 \cdot 10^{-8}\mathrm{GeVs}^{-1}\mathrm{sr}^{-1}\mathrm{cm}^{-2}$ in the energy range of 20 TeV $\leq E \leq$ 3.0 PeV can be derived. This upper limit is considerably lower than earlier IceCube limits, and lower than the astrophysical neutrino flux discovered later. However, the atmospheric flux that is obtained in the same fit is considerably higher than model predictions based on recent measurement. If the atmospheric flux is constrained to the range of these model predictions, the upper limit is $E^2\Phi_{astro,\,ul} = 3.2 \cdot 10^{-8}$ $\mathrm{GeVs}^{-1}\mathrm{sr}^{-1}\mathrm{cm}^{-2}$, which is compatible with the astrophysical neutrino flux finally detected by IceCube using two years of data from the completed IceCube detector.

Zusammenfassung

Das Ziel dieser Dissertation ist die Suche nach dem astrophysikalischen Neutrinofluss in einem IceCube-Datensatz bestehend aus 335 Tagen. IceCube ist ein 1 km^3 großer Neutrinodetektor, welcher sich am Südpol befindet und aus 86 in das Eis eingefrorenen Trossen besteht, von denen jede mit 60 Digitalen Optischen Photomultipliern (DOM) bestückt ist. Der Detektor befand sich noch in der Konstruktionsphase, daher bestand er nur aus 59 Trossen (IC59), als die Daten für diese Analyse gewonnen wurden.
Die hier behandelte Analysemethode ist empfindlich für alle drei Neutrinoarten. Wenn Neutrinos mit den im Eis vorhandenen Atomkernen wechselwirken, werden geladene Teilchen erzeugt, welche Tscherenkow-Strahlung aussenden, die dann von den DOM registriert und zur Rekonstruktion der Neutrinowechselwirkung verwendet wird. Diese Neutrinoereignisse müssen aus einem großen Untergrund von atmosphärischen Myonen, der 10^8 mal mehr Myonen als Neutrinos auf Trigger-Level enthält, gefiltert werden. Atmosphärische und astrophysikalische Neutrinos können nur auf statistischem Wege auf der Grundlage ihrer rekonstruierten Energien unterschieden werden.
Um eine verlässliche Vorhersage für atmosphärische Myonen in der finalen Filterstufe zu erreichen, wurde eine große Anzahl von Myonen simuliert. Die vorgestellte Analyse war die erste, welche eine livetime von über einem Jahr für die Simulation von atmosphärischen Myonen erreicht hat (für $E \geq 10$ TeV).
Eine erste Analyse zählte die Ereignisse mit einer Energie von $E > 38$ TeV und fand 8 Ereignisse mit Energien zwischen 39 TeV und 67 TeV bei einer Untergrunderwartung von 3.6 ± 0.3 Ereignissen. Dieser Überschuss wurde mit Hilfe eines Likelihood-Fit mit einer Energieschwelle von 10 TeV genauer untersucht. Es war kein astrophysikalischer Neutrinofluss nötig, um den Überschuss zu beschreiben. Stattdessen wurde der Überschuss von einer höheren Normierung des atmosphärischen Neutrinoflusses absorbiert. Wenn keine weiteren Einschränkungen von unabhängigen Messungen oder Modellen des atmosphärischen Neutrinoflusses verwendet werden, kann eine 90% obere Grenze für den astrophysikalischen Neutrinofluss aller Neutrinoarten von $E^2\Phi_{astro,\,ul} = 1.7 \cdot 10^{-8}\mathrm{GeVs}^{-1}\mathrm{sr}^{-1}\mathrm{cm}^{-2}$ im Energiebereich von 20 TeV $\leq E \leq$ 3.0 PeV berechnet werden. Diese obere Grenze auf den Neutrinofluss liegt deutlich unter denen vorheriger IceCube-Analysen und ist kleiner als der später entdeckte astrophysikalische Neutrinofluss. Der atmosphärischen Neutrinofluss, der im gleichen Fit bestimmt wurde, liegt deutlich über Modellvorhersagen basierend auf vor kurzem gewonnenen Messdaten. Wenn der atmosphärische Neutrinofluss auf das Intervall dieser Modellvorhersagen beschränkt wird, ergibt sich eine obere Grenze für den astrophysikalischen Neutrinofluss aller Neutrinoarten von $E^2\Phi_{astro,\,ul} = 3.2 \cdot 10^{-8}\mathrm{GeVs}^{-1}\mathrm{sr}^{-1}\mathrm{cm}^{-2}$ im Energiebereich von 20 TeV $\leq E \leq$ 3.0 PeV, was verträglich mit dem mittlerweile von IceCube gemessenen Neutrinofluss ist, welcher mit einer Analyse mit zwei Jahre Messzeit des fertiggestellten Ice-Cube-Detektors bestimmt wurde.

Contents

1 Introduction

In 1930, Wolfgang Pauli proposed the existence of a neutral weakly interacting particle in order to explain the continuous energy spectrum of electrons emitted in radioactive β decay [132]. Since this particle was never observed before, its interaction cross section was expected to be very small. The neutrino was finally discovered in 1956 by Cowan and Reines et al. [47], exploiting the inverse beta decay ($\overline{\nu}_e + p \rightarrow e^+ + n$) initiated by the large $\overline{\nu}_e$-flux from nuclear fission in the Savannah River Plant reactor on target protons in a liquid scintillator. The measured cross section was $6.3 \cdot 10^{-44}$ cm^2. The muon neutrino was discovered in 1962 [50] and the tau neutrino in the year 2000 [52, 53].
Neutrino astrophysics started to become very interesting on February 24th 1987 when the supernova SN1987A exploded in the Large Magellanic Cloud about $1.7 \cdot 10^5$ light years away, and was observed by several experiments (see e.g. [87, 80, 36]). The supernova likely emitted a large fraction of its gravitational binding energy, of the order of about 10^{53} ergs, in a neutrino burst lasting only a few seconds, and consisting of about 10^{58} neutrinos.
Based on the data events from SN1987A, some neutrino properties could be constrained [26]. A neutrino mass limit of the order $m_{\nu_e} \leq 16$ eV as well as an upper limit on the neutrino charge was derived. Additionally, the data was used to derive a limit on the number of neutrino flavors in the range from 1 to 8. The measured neutrinos also provided information about the supernova such as the temperature, the cooling time scale and the ν_e flux. This helped to confirm the schematic picture of the stellar collapse of the progenitor star during the supernova.
The neutrino detection of SN1987A increased the interest in neutrinos as messenger particles. Since they only interact weakly, they can pass easily through all kinds of dense matter and are also unaffected by radiation and magnetic fields, which is a huge advantage over photons or charged particles. As messenger particles, neutrinos are therefore able to provide information about objects in the universe from which no photons or charged particles can escape. Neutrino astronomy may be able to open a completely new observation window to the universe, similar to the first observations of non-visible ranges of the electromagnetic spectrum in the past.
One specific case in which this is of particular interest is the search for the sources of cosmic rays (see section 2.1.3). Since cosmic rays are deflected in the magnetic fields of the Milky Way, they cannot be traced back to their original sources. However, when cosmic rays interact with the ambient matter around their sources, neutrinos are produced, and these particles do point back to their production origin. The detection of these neutrinos, which have much higher energies than those detected in SN1987A, offers the unique possibility to solve the riddle of the origin of cosmic rays.
To date, no single neutrino source has yet been discovered [6]. However, the sum of the

fluxes of all neutrino sources is may still be detectable. The analysis presented in this thesis searches for this diffuse astrophysical neutrino flux. In order to be able to detect this flux, a detector volume of the order of at least 1 km^3 is needed [92, 89]. IceCube is the first experiment [12], that provides the necessary detector size. The analysis in thesis is based on one year of IceCube data.
In the search for the diffuse astrophysical neutrino flux in this thesis, the so-called cascade event channel is used. Cascade events are produced by all three neutrino flavors, which increases the probability to detect astrophysical neutrinos. IceCube is sensitive to cascade events in the energy range from some TeV up to several PeV. Furthermore, cascade events have a good energy resolution, which helps to distinguish the different spectra of astrophysical neutrinos and atmospheric neutrinos, produced by cosmic ray interactions with the atmosphere.
In chapter 2 of this thesis, the cosmic ray flux and its likely acceleration mechanism are introduced. Afterwards, the connection of the production of cosmic rays and high energy neutrinos, their propagation and the astrophysical neutrino flux model are discussed. Furthermore, the large experimental background present in this analysis, consisting of atmospheric muons and neutrinos, is introduced.
Chapter 3 gives an overview about the IceCube experiment, the interaction of high energy particles in the ice and the light propagation in the ice. Based on these mechanisms, the different event topologies created by muons and neutrino interactions are introduced. Finally, the data acquisition of the IceCube detector is discussed.
In chapter 4, the simulation of signal and background events for the IceCube experiment is discussed.
Chapter 5 describes the event selection and the variables on which it is based. The event selection is split into different groups of cuts, which are described in detail. At the end of the chapter, the results of the initial first cut and count analysis of the data are presented.
In chapter 6, a maximum likelihood fit is applied to the data events found. Its results are discussed and compared to the results of the IceCube analysis that found the astrophysical neutrino flux. The final chapter, chapter 7, provides a brief summary of the thesis.

2 Basics of Cosmic Rays and High Energy Neutrinos

2.1 Cosmic Rays

In the following, the discovery and the features of the cosmic ray flux, a likely acceleration mechanism for the nuclei and the potential sources of cosmic rays will be discussed.

2.1.1 The Cosmic Ray Flux

In 1912, Viktor Hess tried to measure the decrease of ionizing radiation originating from radioactive material in the earth as a function of height. First measurements showed the expected drop of ionization rate up to about 1000 m [76]. Furthermore, the ionization rate was smaller above large lakes than above land at the same height. This was expected since there is less radioactive minerals in water than in the soil. Surprisingly, at even higher altitudes the ionization rate started to increase again, and reached a value at about 5000 m which was around twice as high as on the ground. Viktor Hess concluded that there must be an additional source of ionizing radiation coming from the sky. These measurements were the first indication for the existence of cosmic rays.
Since that time, many more measurements of cosmic rays have been undertaken. Today, we know that the earth's atmosphere is bombarded constantly by charged particles with very high energies. Some of the measured particles' energies are higher by many orders of magnitude than everything current particle accelerators are able to provide. This raises the question of how these particles are accelerated, and what the sources of these highly energetic particles are. Due to the deflection of charged particles in the interstellar magnetic fields, their direction information is lost and therefore a search for their origins is nearly impossible. Nevertheless, lots of direct and indirect measurements have strongly increased our knowledge of the properties of cosmic rays.
Direct measurements are performed by detectors mounted on balloons and satellites. These detectors are able to measure the energy of the particles and allow further particle identification [34]. Some of the recent balloon experiments are the *Balloon-borne Experiment with a superconducting Solenoid Spectrometer* (BESS) with an energy range of 1 GeV per nucleon up to several 100 GeV per nucleon [74], the *Cosmic Ray Energetics and Mass Balloon Experiment* (CREAM), which is sensitive between a few TeV per nucleon up to a few 100 TeV per nucleon [133, 99] and the *Transition Radiation Array for Cosmic Energetic Radiation* (TRACER), which has an energy range of about 10 GeV up to several 100 TeV

[40].
Additionally, cosmic ray detectors can be operated on satellites like the *Payload for Antimatter Matter Exploration and Light-nuclei Astrophysics* (PAMELA), which covers an energy range from 1 GeV to about 1 TeV per nucleon [19, 18] or on the International Space Station like the *Alpha Magnetic Spectrometer* (AMS) with an energy range from 1 GeV to 1 TeV [44].
From these and other experiments we learn that the cosmic ray flux consists predominantly of protons and nuclei. Figure 2.1 shows the spectra of several components of the cosmic ray flux.

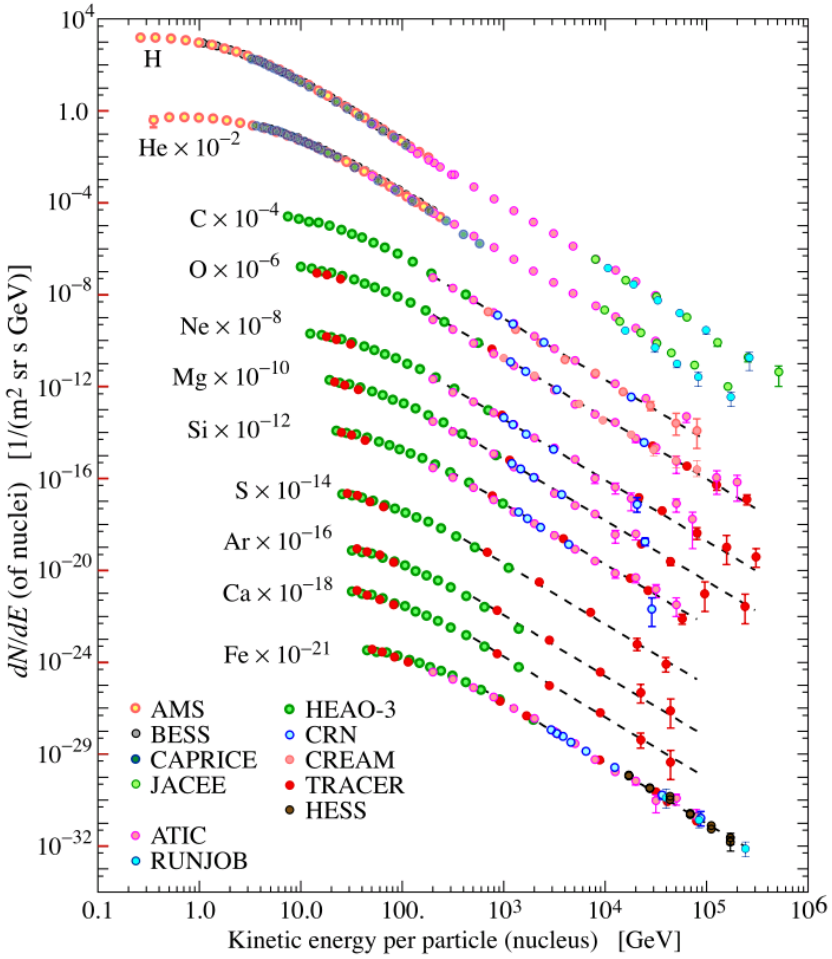

Figure 2.1: *Intensity of several elements present in cosmic rays as a function of their energy-per-nucleus. The plot was taken from [34].*

The differential flux of nucleons in the energy range from some tens of GeV up to about 100

TeV can be approximately described by

$$\frac{d\Phi}{dE}(E) \approx 1.8 \cdot 10^4 \left(\frac{E}{1\ \mathrm{GeV}}\right)^{-\alpha} \frac{\text{nucleons}}{\mathrm{m}^2 \cdot \mathrm{s} \cdot \mathrm{sr} \cdot \mathrm{GeV}}, \tag{2.1}$$

with the energy-per-nucleon E and the cosmic ray spectral index $\alpha = 2.7$. About 79% of the nucleons are protons and about 15% are bound in helium nuclei. The remaining 6% are nuclei heavier than He with varying abundances. Electrons and positrons contribute less than 1%. Antiprotons were found in cosmic rays, but up to now, no antideuteron or antihelium were detected, although remnant antimatter from the time of the big bang could still exist. A collection of experimental data for cosmic ray nuclei and electrons can be found in [100]. The detection area of balloons and satellites is naturally limited to the order of some m^2. Therefore, for the smaller fluxes at higher energies, a different kind of detector is necessary in order to be able to collect reasonable statistics. Experiments measuring the air-showers in the atmosphere produced by the interaction of highly energetic cosmic rays with air nuclei are able to cover the high-energy part of the cosmic ray spectrum. They derive the air-shower properties from the detection of the shower muons, electrons and photons that hit the surface and the emitted Cherenkov and fluorescent light from charged particles, or their radio emission. These ground-based experiments reach sizes up to many km^2. Some of the recent ground-based experiments covering the energy range from 10 TeV up to 1 EeV are KASCADE [24], KASCADE Grande [25], IceTop [14], TUNKA [29] and TIBET AS-Gamma [22]. HIRes [39] and AUGER [15] can observe cosmic rays up to energies of about 100 EeV.

Figure 2.2 shows the all-particle cosmic ray flux spectrum. The description of its features follows Blümer et al. [37]. The spectrum can be approximately described by a broken power law with an index $\gamma = -2.7$ up to the so-called knee at an energy of $E_{knee} \approx 4$ PeV. For higher energies, the power law index changes to $\gamma = -3.1$. It is assumed that the decline of the light element flux is responsible for the index change in the knee region. The cut-off energies of the different elements are proportional to their nuclear charge Z, $E_{cut-off} = Z \cdot 4.5$ PeV. Up to energies of about $10^{17} - 10^{18}$ eV, one assumes that cosmic rays are of Galactic origin accelerated in shock fronts formed in supernova remnants (SNRs, see section 2.1.3). The highly energetic particles then diffuse through the galaxy. The knee is believed to be caused by sequential breaks in the individual elements' spectra, starting with the lighter elements. A further feature is the so-called second knee at an energy of about $10^{17.5}$ eV followed by the so-called ankle at $10^{18.5}$ eV. According to the classical ankle model, the transition between the Galactic and extragalactic cosmic rays occurs at the ankle. In this model, the second knee is interpreted as a change in the composition of cosmic rays from lighter to heavier nuclei before the protons of extragalactic origin start to dominate at the ankle [88]. At even higher energies of about 10^{20} eV, the so-called Greisen-Zatsepin-Kuzmin (GZK) cut-off [72, 135] is expected to suppress the cosmic ray flux via the resonant production of Δ^+ in interactions of the highest energy cosmic rays with cosmic microwave background photons.

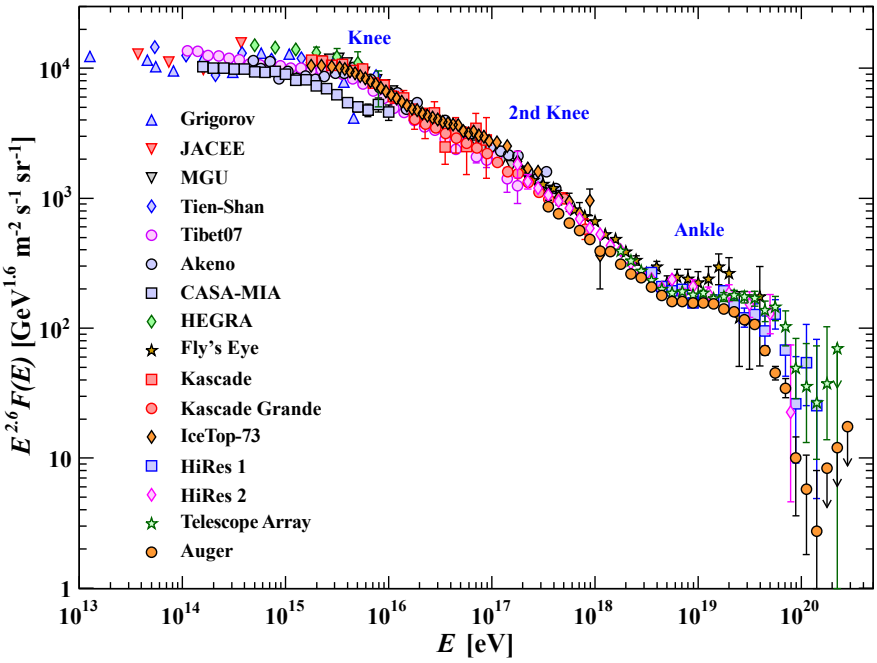

Figure 2.2: *All-particle cosmic ray energy spectrum scaled with $E^{2.6}$ from air shower experiments. The figure was taken from [37].*

2.1.2 Fermi Acceleration

The Fermi mechanism describes the energy gain of charged particles in interstellar clouds and was already published in 1949 [58]. This brief introduction to first and second order Fermi acceleration follows Longair et al. [116].

In the original paper from Fermi [58], charged particles are reflected by the magnetic fields from moving plasma clouds (see figure 2.3). These clouds move randomly with typical velocities u. By staying for a characteristic time τ_{esc} in the acceleration region, charged particles gain energy by several reflections from these clouds. With the assumption that the clouds are infinitely massive and therefore their momentum is unchanged in the collision process with the charged particles, Fermi derived an average energy gain per collision of

$$\left\langle \frac{\Delta E}{E} \right\rangle = \frac{8}{3}\left(\frac{u}{c}\right)^2 . \tag{2.2}$$

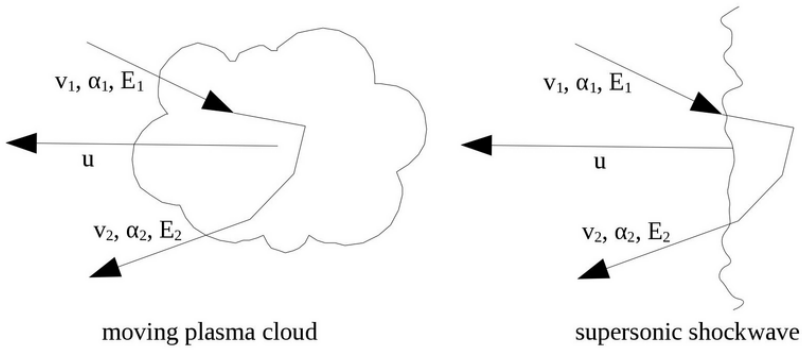

Figure 2.3: *A sketch of the Fermi acceleration of charged particles: on a moving cloud (left, second order) and on a shockfront (right, first order). The parameters (v_1, α_1, E_1) and (v_2, α_2, E_2) are the speed, the angle and the energy of the charged particle before and after the scattering process, respectively. The parameter u is the speed of the moving plasma cloud or the shockwave, depending on the scenario.*

Due to the average energy gain of $(u/c)^2$, this is called second-order Fermi acceleration. This process results in a power-law energy spectrum for the accelerated particles, given by

$$N(E) = C \cdot E^{-\gamma}, \tag{2.3}$$

with a normalization constant C. Taking into account the small velocities of interstellar clouds in comparison to the speed of light c results in $u/c < 10^{-4}$, which only leads to an energy gain in the order of $(u/c)^2 < 10^{-8}$ of the charged particles. The mean free path of charged particles in the interstellar medium is of the order of about 0.1 pc, resulting in only a few collisions per year and therefore leading to a very slow energy gain of the charged particles. Additionally, charged particles with small energies also quickly lose energy again through ionization. Therefore, the initial acceleration process must be fast enough to compensate this energy loss. Due to these reasons, second-order Fermi acceleration is not considered to be the acceleration mechanism responsible for cosmic rays. A more efficient process is necessary.
This process is believed to be diffusive shock acceleration. In this model, a supersonic shockfront from a supernova remnant moves through the interstellar medium (see figure 2.3). The matter ejected in supernova explosions can have velocities of the order of $\beta = u/c \approx 0.01$. There are typically magnetic inhomogeneities nearby on both sides of the shockfront, and these can reflect particles back and forth across the front. Each time they move trough the shockfront they gain some energy

$$\left\langle \frac{\Delta E}{E} \right\rangle = \frac{4}{3}\frac{u}{c}, \tag{2.4}$$

as derived for example in [116]. The probability of a particle remaining in the acceleration

region decreases as the number of crossings increase. This means that fewer particles are accelerated to higher energies. The particle spectrum from this process is given by

$$N(E) = C \cdot E^{-2}. \tag{2.5}$$

The first-order Fermi process is much more efficient than the second-order counterpart, and leads to higher energy gains in much shorter times. Therefore, supernova remnants, with their strong shocks, are a likely origin of the cosmic ray flux.

2.1.3 Sources of Cosmic Rays

In order to accelerate charged particles to the highest energies, they must stay in the acceleration region. This can be achieved by magnetic confinement of the particle during the acceleration process. Therefore, the acceleration region has to be larger than the gyroradius of the particle

$$r_g = \frac{p}{zeB} = 1.08 \frac{(E/\mathrm{PeV})}{z(B/\mu\mathrm{G})}\mathrm{pc}. \tag{2.6}$$

Hillas [79] has showed that a source of cosmic rays with size L and a magnetic field B can produce cosmic ray particles with a maximum energy of

$$E_{max} = (z \cdot e \cdot \beta c) \cdot B \cdot L, \tag{2.7}$$

where βc is the velocity of the acceleration region (e.g. the shockfront) and z the charge of the particle in elementary charge e. Inserting the maximal measured cosmic ray energy $E = 10^{20}$ eV in equation 2.7 results in

$$B \cdot L = \frac{3 \cdot 10^{11}}{z \cdot \beta}\ \mathrm{T} \cdot \mathrm{m} \tag{2.8}$$

being a minimal (due to β) constraint on the product of the magnetic field B and size L of the cosmic ray acceleration region.
Figure 2.4 shows a diagram of the Hillas criterion with several potential cosmic ray sources. Even for the brightest known γ-ray source, the crab SNR, the product $B \cdot L$ for the acceleration site is by orders of magnitude too small to accelerate cosmic rays to the highest energies. There is only a very limited number of known objects that lie above the iron confinement line.

The Hillas criterion is only a necessary condition but not a sufficient one. Some source candidates will be briefly discussed following [93].
Shocks in the intergalactic medium can occur due to the accretion of gas and dark matter around very large structures in the universe such as clusters of galaxies. In these accretion regions, diffusive shock acceleration can take place. The linear extension of the magnetized

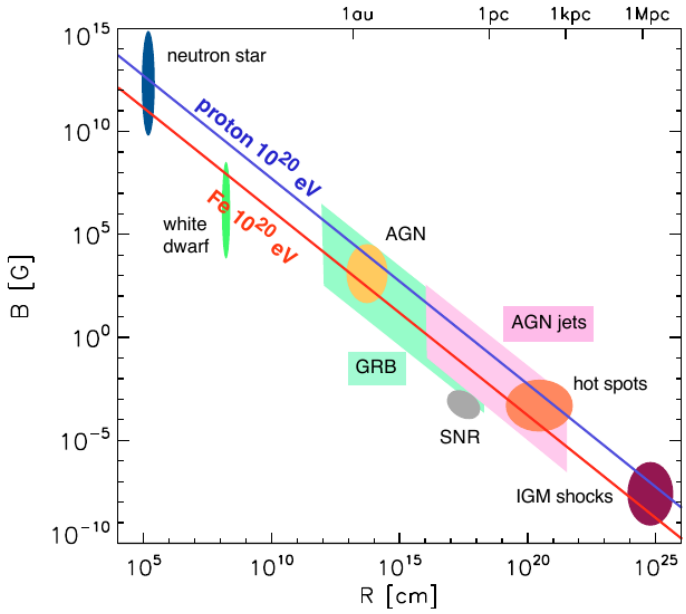

Figure 2.4: *The Hillas criterion, the product $B \cdot L$ (see equation 2.8) for protons and iron for the stronger candidate sources of ultrahigh energy cosmic rays (UHECRs). Among them are active galactic nuclei (AGN), gamma-ray bursts (GRBs), shocks in the intergalactic medium (IGM) and supernova remnants (SNRs). The areas represent the uncertainties of the sources' parameters. The plot was taken from [93].*

shock can be estimated to be about 10 Mpc, and the magnetic field strength to be about 1 μG, leading to a confinement of charged particles up to energies of the order of 10^{20} eV. Detecting very-high-energy gamma rays from these sites can help to constrain their parameters. In a recent numerical calculation [124] it was shown that the energy of a proton can not exceed about 10^{19} eV due to its energy loss in the interaction with photons of the Cosmic Microwave Background.

A possible source of the highest energetic cosmic rays is in active galactic nuclei (AGN). These cores of active galaxies generate large amounts of electromagnetic radiation. It is assumed that their energy output is a result of matter accreting around and falling into supermassive black holes at their centers. For a black hole mass of about 10^9 solar masses, it is assumed that a magnetic field strength of about 300 G is reached in the central region within a radius of about 100 AU. Charged particles with energies up to about hundreds of EeV can be confined there. Jets can be formed along the rotation axis of the accretion disk. These jets, or the bow shocks they form when they hit the interstellar medium, can be sites of cosmic ray acceleration. The acceleration of ultra-high energy cosmic rays (UHECRs) in AGN is expected to lead to features in the gamma-ray spectrum of these sources. With more gamma-ray data over a broad energy range, it may be possible to distinguish these hadronic signatures from those caused by leptonic acceleration, and gain a deeper understanding of the acceleration mechanisms of UHECRs in AGNs.

Gamma-ray bursts (GRBs) are extremely bright sources of gamma rays. They can last from some milliseconds to some minutes. They are thought to be created by a special class of supernova, or the merger of neutron stars. The explosion of a GRB leads to shock regions with magnetic field strengths of about 10^6 G, which are considered to be possible acceleration sites for UHECR. Current models predict, under some assumptions, the acceleration of charged particles in GRBs up to 10^{20} eV. The gamma-ray flux from a GRB detected at earth is comparable to the observed flux of UHECRs.
A special class of young millisecond neutron stars, so-called magnetars, with magnetic fields strengths on their surface of the order of 10^{15} G, are also promising source candidates for UHECRs. According to a model from Arons et al. [27], newly born magnetars can accelerate charged particles up to 10^{20} eV. With some more model assumptions, 5% of the extragalactic magnetar population is able to produce the observed UHECR flux.

2.2 Highly Energetic Neutrinos

In this section, neutrino production mechanisms at sources of highly energetic cosmic rays are introduced. Thereafter, the neutrino propagation from the source to the Earth is discussed. The diffuse astrophysical neutrino flux and its detection are then presented. Finally, atmospheric neutrinos are discussed.

2.2.1 Neutrino production in astrophysical sources

A cosmic ray source accelerating protons or other nuclei to very high energies is also a source of neutrinos [64, 90]. They are produced in the interactions of high energy protons with ambient matter via the process

$$p \ + \ X \rightarrow \begin{cases} \pi^0 \ + \ X \\ \pi^{\pm} \ + \ Y \end{cases} , \tag{2.9}$$

in which X represents either a proton or neutron, and Y another or several other particles. Alternatively, the protons can also interact with ambient photons γ

$$p \ + \ \gamma \rightarrow \Delta^+ \rightarrow \begin{cases} \pi^0 \ + \ p \\ \pi^+ \ + \ n \end{cases} . \tag{2.10}$$

While the neutral pions immediately decay via

$$\pi^0 \rightarrow \gamma \ + \ \gamma, \tag{2.11}$$

neutrinos are produced in the charged pion decays

$$\pi^+ \rightarrow \mu^+ + \nu_\mu \rightarrow e^+ + \nu_e + \overline{\nu}_\mu + \nu_\mu \tag{2.12}$$

$$\pi^- \rightarrow \mu^- + \overline{\nu}_\mu \rightarrow e^- + \overline{\nu}_e + \nu_\mu + \overline{\nu}_\mu. \tag{2.13}$$

Kaons can also be produced in addition to pions. It follows from equations 2.12 and 2.13 that at the source, the neutrino flavor ratio is $\nu_e : \nu_\mu : \nu_\tau$=1:2:0.
When the density of the ambient matter around the source is small, the pions and muons decay without interacting, which conserves their original production spectrum. Neutrinos are not deflected by magnetic fields like the charged particles, and also cannot be absorbed in dense matter like gamma rays. Therefore, they might point back to the sources of high energy cosmic rays and so they provide important information about the sources which cannot be gained otherwise.

High energy gamma-ray fluxes from a variety of objects can currently be explained either with leptonic [38] or hadronic [134, 41] models. In leptonic models, the high-energy radiation is produced by synchrotron and bremsstrahlung emission from high-energy electrons. High-energy photons can be produced by inverse Compton scattering. According to hadronic models, the high-energy gamma-rays are produced by the decay of π^0 mesons (see equation 2.11) emerging from the interaction of cosmic rays with ambient matter or radiation (see equations 2.9 and 2.10). Since neutrinos can only be produced in an hadronic acceleration model, the simultaneous observation of neutrinos from a high-energy gamma-ray source can help to distinguish the acceleration mechanisms.

2.2.2 Neutrino propagation

Using a large underground detector in the Homestake mine, Davis et al. measured the the solar neutrino flux. The measured flux was a factor of 7 smaller than expected from theoretical calculation based on nuclear fusion reactions in the sun [51]. Already one year later, Pontecorvo et al. proposed to solve the riddle of solar neutrinos' disappearance by the oscillation of electron neutrinos into muon neutrinos [73].
When neutrinos are created in weak interactions, their flavor is defined by the flavor of the involved leptons. Recent experiments [71] have confirmed neutrino oscillations. Due to the non-zero neutrino masses and neutrino mixing, a neutrino of a certain flavor (ν_e, ν_μ and ν_τ) can transform into another flavor during propagation. This can explain the disappearance of a number of neutrinos with a certain flavor and the appearance of different flavored neutrinos. The following brief discussion of neutrino mixing follows [110]. Neutrinos are created in weak interactions as flavor eigenstates $|\nu_\alpha\rangle$ with $\alpha = (e, \mu, \tau)$. The evolution of a quantum state is described by the application of the time evolution operator

$$|\Psi(t)\rangle = \exp\left(\frac{-iHt}{\hbar}\right)|\Psi(t=0)\rangle\,, \tag{2.14}$$

in which H is the Hamilton operator and $\hbar$ the Planck constant divided by 2π. The Hamilton operator H acts on the particle's mass eigenstates $\left|\nu_j\right\rangle$ with $j = (1, 2, 3)$. The evolution of a flavor eigenstate with time can then be described as

$$|\nu_\alpha(t)\rangle = \sum_{j=1,2,3} U^*_{\alpha j} \exp(-iE_j t) \left|\nu_j\right\rangle, \tag{2.15}$$

with the mixing matrix $U_{\alpha j}$ and energy eigenvalues E_j of the Hamilton operator.
The 3 x 3 unitary mixing matrix $U_{\alpha j}$ can be described by three mixing angles θ_{ij} and the CP-violating phase δ_{CP}. It is analogous to the CKM matrix for the quark sector. It can be expanded as the product of three 2 x 2 rotation matrices

$$U = \begin{pmatrix} 1 & 0 & 0 \\ 0 & c_{23} & s_{23} \\ 0 & -s_{23} & c_{23} \end{pmatrix} \begin{pmatrix} c_{13} & 0 & s_{13}e^{-i\delta_{CP}} \\ 0 & 1 & 0 \\ -s_{13}e^{i\delta_{CP}} & 0 & 1 \end{pmatrix} \begin{pmatrix} c_{12} & s_{12} & 0 \\ -s_{12} & c_{12} & 0 \\ 0 & 0 & 1 \end{pmatrix}, \tag{2.16}$$

with $c_{ij} = \cos\theta_{ij}$ and $s_{ij} = \sin\theta_{ij}$. Knowing the time-like evolution of a flavor eigenstate α at time $t = 0$, one can derive the probability to measure the this eigenstate at a time t in the flavor β

$$\begin{aligned} P(\nu_\alpha \to \nu_\beta) &= \left|\left\langle \nu_\beta(t) \,|\, \nu_\alpha(t=0)\right\rangle\right|^2 \\ &= \delta_{\alpha\beta} - 4 \sum_{i>j} Re\left(U^*_{\alpha i} U_{\alpha j} U_{\beta i} U^*_{\beta j}\right) \sin^2\left(\frac{\Delta m^2_{ij} L}{4E_\nu}\right) \\ &\quad + 2 \sum_{i>j} Im\left(U^*_{\alpha i} U_{\alpha j} U_{\beta i} U^*_{\beta j}\right) \sin\left(\frac{\Delta m^2_{ij} L}{2E_\nu}\right), \end{aligned} \tag{2.17}$$

with the difference of the squared mass eigenstates $\Delta m^2_{ij} = m^2_i - m^2_j$.
Averaging over the $\sin^2$ term in equation 2.17 for large distances L leads to a factor of 1/2. Averaging over the sin term leads to zero, and therefore the third term vanishes. Taking the parameter values from Gonzalez Garcia et al.[1] [71] the matrix U becomes

$$U \approx \begin{pmatrix} 0.82 & 0.55 & 0.09 + 0.12\,i \\ -0.46 + 0.07\,i & 0.58 + 0.04\,i & 0.67 \\ 0.32 + 0.07\,i & -0.60 + 0.05\,i & 0.73 \end{pmatrix}. \tag{2.18}$$

[1] The values of θ_{12},θ_{13},θ_{23}, and δ_{CP} from the column "Normal Ordering" of Table 1 are used.

With equation 2.17, the matrix $P_{\alpha\beta}$ is given by

$$P \approx \begin{pmatrix} 0.55 & 0.26 & 0.19 \\ 0.26 & 0.36 & 0.38 \\ 0.19 & 0.38 & 0.43 \end{pmatrix}. \tag{2.19}$$

That results in

$$\begin{pmatrix} \nu_e \\ \nu_\mu \\ \nu_\tau \end{pmatrix}_{earth} = P \cdot \begin{pmatrix} \nu_e \\ \nu_\mu \\ \nu_\tau \end{pmatrix}_{source} = P \cdot \begin{pmatrix} 1 \\ 2 \\ 0 \end{pmatrix}_{source} \approx \begin{pmatrix} 1.07 \\ 0.98 \\ 0.96 \end{pmatrix} \approx \begin{pmatrix} 1 \\ 1 \\ 1 \end{pmatrix}. \tag{2.20}$$

Therefore, at earth, approximately the same number of neutrinos of each flavor is expected.[2] Even though almost no tau neutrinos are expected to be produced in the sources of cosmic rays, due to neutrino oscillations, about one third of the neutrinos arriving at earth is expected to be of ν_τ flavor.

2.2.3 Astrophysical Neutrino Flux

As described in section 2.2.1, neutrinos are produced by the interactions of high energetic cosmic rays inside their sources and during propagation. If sufficiently strong neutrino sources exist, they can be discovered by point source searches. However, up to now, even the latest IceCube (see section 3.1) point source search consisting of 1373 days of data has not found a point source yet [6]. Current best upper limits are $\Phi_\nu^{ps\ north} \lesssim 10^{-12}\ \mathrm{TeV}^{-1}\mathrm{cm}^{-2}\mathrm{s}^{-1}$ for the northern sky (1 TeV $< E <$ 1 PeV) and $\Phi_\nu^{ps\ south} \lesssim 10^{-11}\ \mathrm{TeV}^{-1}\mathrm{cm}^{-2}\mathrm{s}^{-1}$ for the southern sky (100 TeV $< E <$ 100 PeV).
Even if individual sources are too weak to be found with the currently available detectors, the sum of the fluxes of all point sources (the diffuse neutrino flux) might still be detectable. Waxman and Bahcall derive a model-independent upper limit on the high-energy neutrino flux [129] based on observations of high-energy cosmic rays, which is briefly summarized in the following.
Observations of UHECR indicate that the cosmic ray flux above $\approx 3 \cdot 10^{18}$ eV is dominated by protons of extra-galactic origin. The production rate of protons in the energy range of 10^{19} eV to 10^{21} eV is

$$\frac{d\epsilon_{CR}}{dt}\left(10^{19}...10^{21}\ \mathrm{eV}\right) \approx 5 \cdot 10^{44}\ \mathrm{erg} \cdot\ \mathrm{Mpc}^{-3} \cdot\ \mathrm{yr}^{-1}, \tag{2.21}$$

according to [126]. With an assumed cosmic ray injection spectrum of $dN_{cr}/dE_{cr} \approx E_{cr}^{-2}$ (coming from Fermi acceleration, see section 2.1.2), it follows for the production rate of

[2] Using the parameter values from the column "Inverted Ordering" of Table 1 of Gonzalez Garcia et al. results in a flavor ratio at earth of $\approx (0.93, 1.05, 1.02) \approx (1, 1, 1)$.

cosmic rays

$$E_{cr}^2 \frac{d^2N}{dE_{cr}dt} = \frac{\frac{d\epsilon}{dt}\left(10^{19}...10^{21}\text{ eV}\right)}{\ln(10^{21}/10^{19})} \approx 10^{44}\text{ erg}\cdot\text{ Mpc}^{-3}\,yr^{-1}. \tag{2.22}$$

If the protons lose a fraction f of their energy in photo-meson production of pions before they escape the source, then the current energy density of ν_μ is given by

$$E_\nu^2 \frac{dN_\nu}{dE_\nu} \approx 0.25 f t_H E_{cr}^2 \frac{d^2N_{cr}}{dE_{cr}dt} \tag{2.23}$$

where $t_H \approx 10^{10}$ yr is the Hubble time. For energy-independent f, the neutrino spectrum follows the cosmic ray injection spectrum ($E_\nu = fE_p \approx 0.05E_p$). Defining the maximum ν_μ intensity I_{max} (one obtains for $f = 1$)

$$I_{max} \approx 0.25\zeta_Z t_H \frac{c}{4\pi} E_{CR}^2 \frac{d^2N_{CR}}{dE_{CR}dt} \approx 1.5\cdot 10^{-8}\zeta_Z \frac{\text{GeV}}{\text{cm}^2\cdot\text{s}\cdot\text{sr}}, \tag{2.24}$$

where the factor $\zeta_Z \approx 3$ takes into account the cosmological redshift of the neutrino energy. The Waxman-Bahcall upper limit for $(\nu_\mu + \bar{\nu}_\mu)$ is

$$E_\nu^2 \Phi_{\nu_\mu}^{WB} = \frac{c}{4\pi} E_\nu^2 \frac{dN_\nu}{dE_\nu} = \frac{1}{2} f I_{max} \lesssim 2.25\cdot 10^{-8} \frac{\text{GeV}}{\text{cm}^2\cdot\text{s}\cdot\text{sr}}. \tag{2.25}$$

This result has to be multiplied by a factor of about $1/2$ to take into account the neutrino oscillations [127] and with a factor of 3 to obtain the all-flavor flux, resulting in (see also [128])

$$E_\nu^2 \Phi_{WB} \lesssim 3.4\cdot 10^{-8} \frac{\text{GeV}}{\text{cm}^2\cdot\text{s}\cdot\text{sr}}. \tag{2.26}$$

The sensitivity of neutrino detectors searching for the diffuse flux of astrophysical neutrinos has increased strongly over the last years. The AMANDA experiment [23] reported a sensitivity of $E_\nu^2\Phi_\nu = 3.8\cdot 10^{-7}$ GeVcm^{-2}s^{-1}sr^{-1} [68] for energies $E > 200$ TeV in 2005. The ANTARES experiment [20] quoted a sensitivity of $E_\nu^2\Phi_\nu = 3.0\cdot 10^{-8}$ GeVcm^{-2}s^{-1}sr^{-1} [35] for an energy threshold of $E > 30$ TeV with four years of data from 2008 to 2011. The sensitivity of the full IceCube detector for electron neutrinos is $E_\nu^2\Phi_\nu = 1.5\cdot 10^{-8}$ GeVcm^{-2}s^{-1}sr^{-1} for one year of data [125].

2.2.4 Atmospheric Neutrinos

The highly energetic nuclei of the cosmic rays interact with the atmosphere and create particle showers. Pions and kaons are created in these particle showers, which decay into muons and muon neutrinos. The muons can decay further into neutrinos. Furthermore, mesons

containing charm quarks (charmed mesons) are also created in the in the particle shower.
The atmospheric neutrinos can be categorized into two sets, so-called conventional and prompt neutrinos. The conventional neutrinos originate from kaon and pion decays. Their energy spectrum $dN/dE \sim E^{-3.7}$ has a steeper index than the index of the cosmic ray flux $\gamma \approx -2.7$, which is a result of the interactions of kaons and pions with the atmosphere before they decay. The conventional neutrino flux contains electron and muon neutrinos.
The prompt neutrinos originate from the decay of charmed mesons. The power-law index of this neutrino flux component follows the one of the cosmic ray flux because they decay so quickly ($\approx 10^{-12}$ s) that they do not interact with the atmosphere. Since charmed mesons are heavier than the tau mass, they can decay into all three neutrino flavors, and therefore they add the atmospheric tau neutrino flux. The prompt neutrinos are expected to become the dominating part of the atmospheric neutrino flux at energies of about 100 TeV.

The spectrum of atmospheric muon and anti-muon neutrinos can be parametrized [61] as a function of the neutrino energy E_ν and the zenith angle θ

$$\Phi_\nu(E_\nu) = \frac{\Phi_N(E_\nu)}{1 - Z_{NN}} \cdot \left(\sum_{i=1}^{3} \frac{A_i}{1 + B_i \cos(\theta) E_\nu / \epsilon_i} \right), \tag{2.27}$$

in which i runs over the decay contributions from pions, kaons and charmed hadrons. The factors A_i and B_i are constants. The overall normalization factor is the primary flux of nucleons $\Phi_N(E_\nu)$ calculated at the neutrino energy E_ν and multiplied with the factor $1/(1 - Z_{NN})$, which is related to the nucleon attenuation length. The competition between the interaction and decay of pions, kaons and charmed hadrons on their way through the atmosphere is determined by their critical energies ϵ_i. The values of the critical energies are $\epsilon_\pi = 115$ GeV, $\epsilon_K = 850$ GeV and $\epsilon_{charm} \approx 50$ PeV.
For $E_\nu > \epsilon_i$, it is more likely that the particle will interact than decay. If $E_\nu \cdot (B_i \cos\theta)/\epsilon_i >> 1$, the energy spectrum is one power steeper than the primary spectrum $\Phi_N(E_\nu)$ and proportional to $\cos^{-1}\theta$. For sufficiently large energies, the conventional atmospheric flux is therefore proportional to $\cos^{-1}\theta$ in contrast to the astrophysical neutrino flux which is expected to be isotropic. This offers a possibility to distinguish them from each other by their different zenith angle θ dependence.

At high energies ($\gtrsim 1$ TeV), most of the atmospheric muons reach the ground before they decay. Therefore, the principal remaining sources of ν_e are the decays of K^+, K_L and K_S. The conventional atmospheric $\nu_e + \bar{\nu}_e$ flux then can be parametrized [63]

$$\begin{aligned} \Phi_\nu(E_\nu) = \Phi_N(E_\nu) \Bigg(& \frac{Z_3 b_{K^+e3} (Z_{NK^+} + Z_{NK^-})}{1 + B_3 \cos\theta E_\nu / \epsilon_K} + \frac{Z_3 b_{K_L e3} Z_{NK_L}}{1 + B_3^* \cos\theta E_\nu / \epsilon_{K_L}} \\ & + \frac{Z_3 b_{K_S e3} Z_{NK_S}}{1 + B_3 \cos\theta E_\nu / \epsilon_{K_S}} \Bigg), \end{aligned} \tag{2.28}$$

where Z_i, b_i, B_i and ϵ_i are constants and E_ν, $\cos\theta$ and $\Phi_N(E_\nu)$ have the same meaning as in equation 2.27.

Conventional atmospheric neutrino model

In this thesis, the HKKMS(2006) model [82] is used for the description of the conventional atmospheric neutrino flux. The calculations start by sampling cosmic rays of a given spectrum in the atmosphere. The cosmic rays are propagated through the atmosphere, and their hadronic interactions and the production of secondary particles and neutrinos are tracked. A three dimensional model of the atmosphere is used for a detailed description of the earth's magnetic field and its influence on the low-energy secondary particles. Figure 2.5 shows the atmospheric neutrino fluxes calculated according to the model.

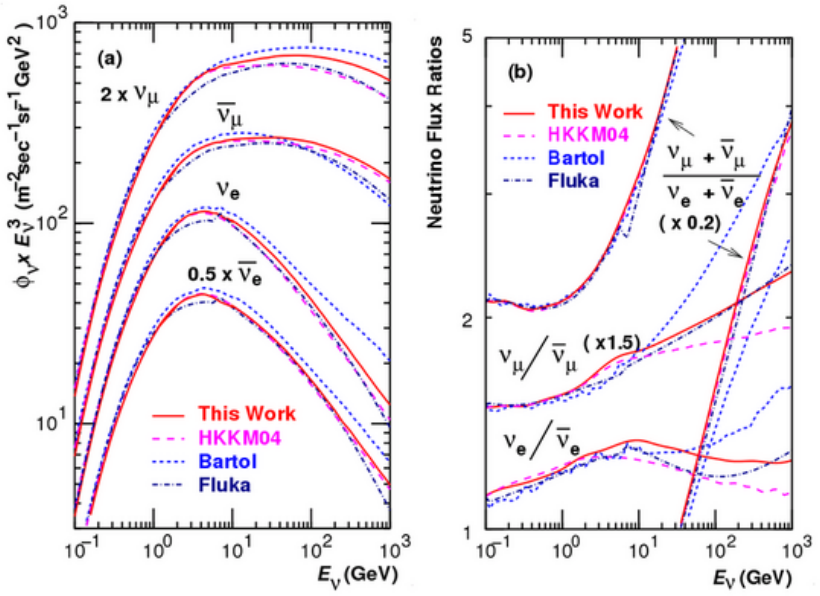

Figure 2.5: *The atmospheric neutrino fluxes and their ratios according to the HKKMS(2006) model (red line) compared with other models. The plot was taken from [82].*

The neutrino flux predictions of the HKKMS(2006) model were extended to higher energies by fitting a physics-motivated analytical parametrization to them, which is based on energy and zenith angle ([60] as cited in [9]). The uncertainty of the atmospheric neutrino flux given by the model is 25% at an energy of 1 TeV.

Prompt atmospheric neutrino model

The prompt neutrino flux in this thesis is described with the Enberg model [55]. The charm production in this model is described by a perturbative QCD approach. Figure 2.6 shows the

prompt atmospheric $\nu_\mu + \bar{\nu}_\mu$ flux from the Enberg model. The prompt atmospheric $\nu_e + \bar{\nu}_e$ flux is identical, since the charmed mesons decay with the same probability into electron and muon neutrinos. The prompt atmospheric $\nu_\tau + \bar{\nu}_\tau$ flux is about an order of magnitude smaller compared to $\nu_\mu + \bar{\nu}_\mu$ flux because only D_s mesons decay into ν_τ.

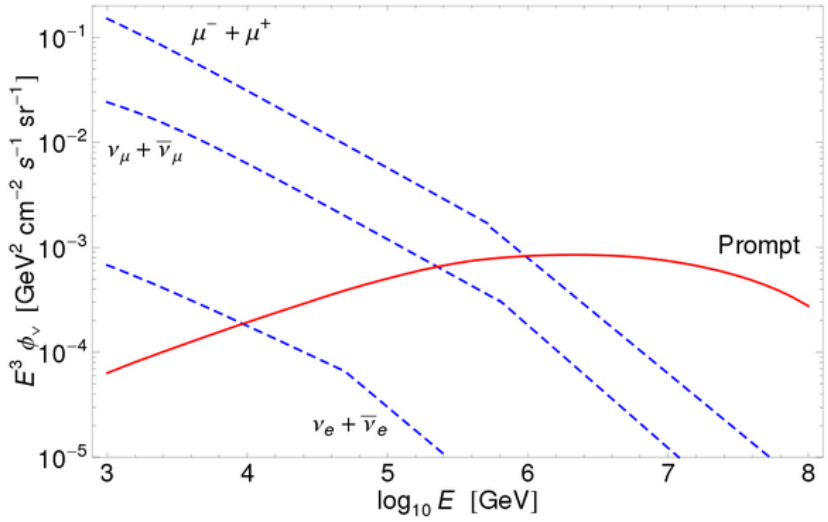

Figure 2.6: *The Enberg model of the prompt atmospheric $\nu_\mu + \bar{\nu}_\mu$ flux (red line) and the conventional fluxes of $\nu_\mu + \bar{\nu}_\mu$ and $\nu_e + \bar{\nu}_e$ (dashed lines). The plot was taken from [55].*

There are several theoretical uncertainties such as the charm quark mass, the gluon distributions and additional parameters from the dipole model used to calculate the deep inelastic scattering. The spectral shape of the prompt neutrino flux only weakly depends on these uncertainties, but the normalization is uncertain up to a factor of almost two. Figure 2.7 shows the Enberg flux model for atmospheric muon neutrinos and its upper and lower uncertainty boundaries as a function of the energy. One can see from the ratio plot in figure 2.7 that ±40% is a good estimate for the uncertainty of the normalization of the Enberg flux.

Similar to the HKKMS(2006) model, a parametrization of Enberg flux model based on the zenith angle and the energy is used in this thesis.

Modification of the atmospheric neutrino models

The HKKMS(2006) and Enberg model do not take into account the knee in the cosmic ray spectrum for the calculation of the atmospheric neutrino fluxes. To correct that, both models are slightly modified with a rescaling factor, which is a function of the energy, according to the H3a model [62]. Details about the rescaling functions used, can be found in the appendix A of [4].
The analysis of this thesis was developed without the H3a correction, but it was used for the conventional and prompt atmospheric neutrino contributions in the final likelihood fit in

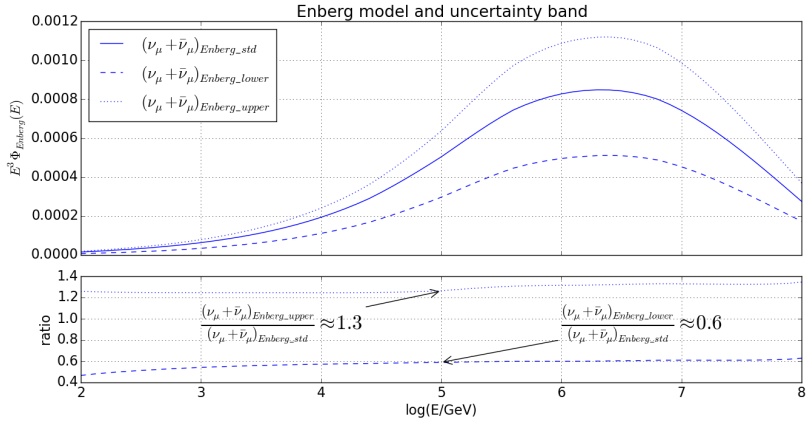

Figure 2.7: *The prompt atmospheric muon neutrino flux and its uncertainties predicted by the model of Enberg [55]. One can see that the ratios of of the upper and lower uncertainty bands to the model are almost independent of the energy.*

section 6.

2.2.5 Neutrino interactions with matter

This brief summary of the interaction of high-energy neutrinos with matter follows [66]. Neutrinos only interact with matter via the weak interaction. In the standard model of particle physics, this interaction is characterized by deep inelastic scattering at the energy scale relevant for this analysis ($E > 1$ TeV). It is described by the exchange of the gauge bosons $W^\pm$ and Z^0. Two principal reactions are possible

$$\begin{aligned} \nu_l + N &\rightarrow l \ + X \quad \text{(CC)} \\ \nu_l + N &\rightarrow \nu_l + X \quad \text{(NC)}, \end{aligned} \tag{2.29}$$

in which ν_l represents a neutrino of flavor $l = (e, \mu, \tau)$, l the associated lepton, N a nucleon and X the reaction product of the nucleon. Both reactions of equation 2.29 also exist for antineutrinos. In this case the ν_l and l are exchanged with their antiparticles $\bar{\nu}_l$ and $\bar{l}$. The charged-current (CC) interaction is mediated by virtual $W^\pm$ bosons, and the neutral-current interaction by virtual Z^0 bosons. Figure 2.8 shows the first-order Feynman diagram for deep-inelastic charged-current scattering of a ν_μ on a nucleon.

The differential cross section for the charged-current interaction of figure 2.8 is given by

$$\frac{d^2\sigma}{dxdy} = \frac{2G_F^2 M E_\nu}{\pi} \left(\frac{M_W^2}{Q^2 + M_W^2} \right)^2 \left(xq(x, Q^2) + x\bar{q}(x, Q^2)(1 - y)^2 \right), \tag{2.30}$$

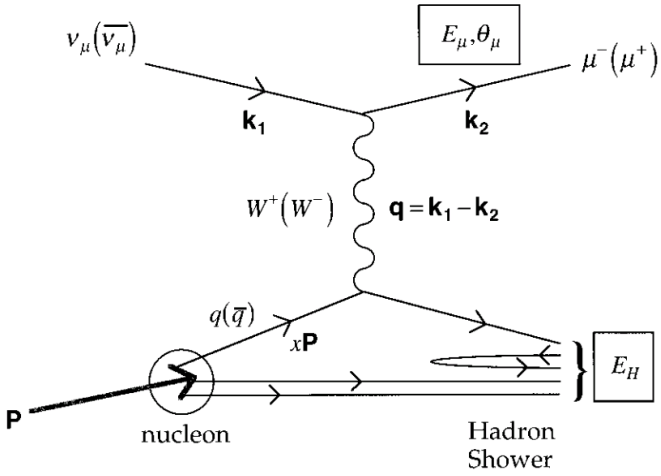

Figure 2.8: *First-order Feynman diagram for a deep inelastic charged-current interaction of a ν_μ scattering on a nucleon. The figure was taken from [43].*

where M is the nucleon mass, M_W the mass of the $W^\pm$ boson, $-Q^2$ the invariant momentum transfer between the incident neutrino and the outgoing muon, $x = Q^2/(2M\nu)$ the Bjorken scaling variable, $y = \nu/E_\nu$, $\nu = E_\nu - E_\mu$ is the energy loss in the target frame, $G_F = 1.16632 \cdot 10^{-5}$ GeV^{-2} the Fermi constant and $q(x, Q^2)$, $\bar{q}(x, Q^2)$ the quark distribution functions, containing the valence and sea quark contributions for various quark flavors in a proton. Since the cross section depends on the mass of the nucleon, high-energy neutrinos interact with the nucleons of an atom rather than with its electrons (there exists an exception that will be discussed later).
The differential cross section for a neutral-current interaction (see equation 2.29) is

$$\frac{d^2\sigma}{dxdy} = \frac{G_F^2 M E_\nu}{2\pi}\left(\frac{M_Z^2}{Q^2 + M_Z^2}\right)^2 \left(xq^0(x, Q^2) + x\bar{q}^0(x, Q^2)(1 - y)^2\right), \tag{2.31}$$

where M_Z is the mass of the Z^0 boson and $q^0(x, Q^2)$, $\bar{q}^0(x, Q^2)$ contain the parton distribution functions.

Figure 2.9 shows the cross sections for neutral-current and charge-current interactions as a function of the energy of the ν or $\bar{\nu}$. In the energy range from 10 GeV to 10 TeV the cross sections rise linearly with the neutrino energy E_ν. Above 10 TeV, the cross section is damped by the W-boson propagator or Z-boson propagator, respectively. For lower energies, the $\bar{\nu}N$ cross sections are smaller than the νN cross sections because the valence quarks in the nucleon predominate and $\bar{\nu}q$ cross sections are damped by the $(1 - y)^2$ factor. At about 1 PeV, the valence quark contribution becomes negligible and the νN and $\bar{\nu}N$ cross sections approach each other.
As noted before, the cross sections of an ν or $\bar{\nu}$ scattering on an electron are much smaller than the νN cross sections, because of the lower electron mass. There is one important exception;

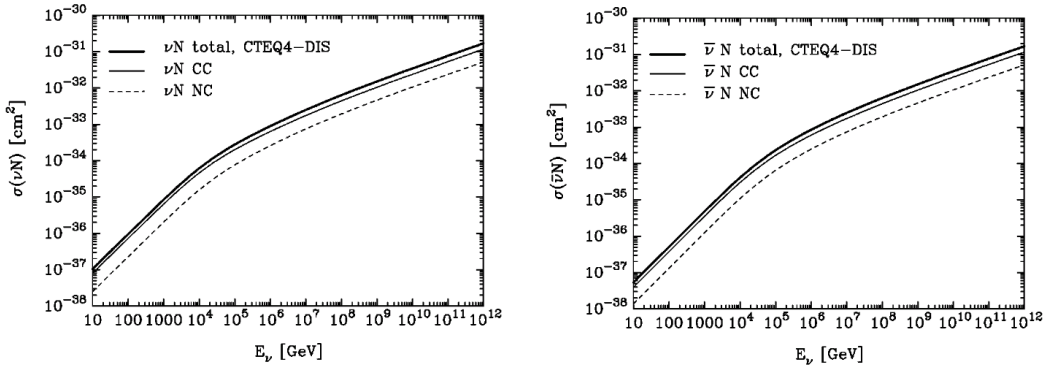

Figure 2.9: *Charged-current (CC) and neutral-current (NC) cross sections for ν (left) and $\bar{\nu}$ (right) with nucleons as a function of the neutrino energy E_ν. The figures are taken from [66].*

the so-called Glashow resonance $\bar{\nu}_e + e^- \rightarrow W^- \rightarrow$ *anything* [70] at $E_\nu^{res} = M_W^2/2m_e \approx 6.3$ PeV. It has a cross section of $\sigma_{Glashow} \approx 5 \cdot 10^{-31}$ cm^2 which is about a factor of 350 larger than the charged-current νN cross section at that energy. Figure 2.10 shows the cross section of the Glashow resonance $\bar{\nu} + e^- \rightarrow W^- \rightarrow$ *hadrons* compared to $\bar{\nu} + N \rightarrow W^- \rightarrow$ *hadrons*. The Glashow resonance offers a unique possibility to distinguish $\bar{\nu}_e$ from all other neutrino flavors at the resonance energy E_ν^{res}.

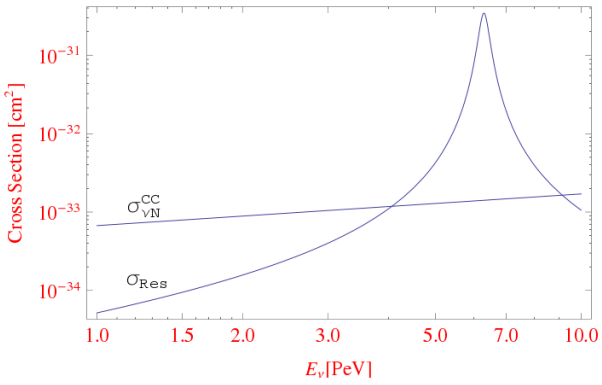

Figure 2.10: *The cross section of the Glashow resonance $\bar{\nu}+e \rightarrow W^- \rightarrow$ hadrons compared to $\bar{\nu} + N \rightarrow W^- \rightarrow$ hadrons. The figure was taken from [28].*

In the energy range from 10^{16} eV to 10^{21} eV, the neutrino cross sections can be approximated

by

$$\sigma_{CC}(\nu N) = 5.5 \cdot 10^{-36}\ \mathrm{cm}^2 \left(\frac{E_\nu}{1\ \mathrm{GeV}}\right)^{0.363}$$
$$\sigma_{NC}(\nu N) = 2.3 \cdot 10^{-36}\ \mathrm{cm}^2 \left(\frac{E_\nu}{1\ \mathrm{GeV}}\right)^{0.363}. \quad (2.32)$$

However, for neutrino energies $E_\nu \gtrsim 10^{16}$ eV, the neutrino cross sections become dependent on the behavior of the parton distributions at very small Bjorken scaling variable x, for which no direct experimental measurement constraints exist. Different model assumptions about the behavior of $x \to 0$ result in different cross sections.
Since the neutrino cross sections increase with the neutrino energy, the earth becomes less transparent for high-energy neutrinos. The water-equivalent interaction length of neutrinos is defined as $\mathcal{L}_{int} = 1/(\sigma_{\nu N}(E_\nu)N_A)$, where $N_A = 6.022 \cdot 10^{23}\ \mathrm{cm}^{-3}$ (water equivalent) is Avogadro's number. Figure 2.11 shows the interaction lengths of charged-current and neutral-current interaction for ν and $\bar{\nu}$. Using the earth density layer model presented in [65], the earth's diameter is about 10^{10} cm of water equivalent. At about $E = 40$ TeV, the charged-current interaction length becomes comparable to the diameter of the earth. At the Glashow resonance, the $\bar{\nu}_e$ interaction length is only 60 km of water equivalent.

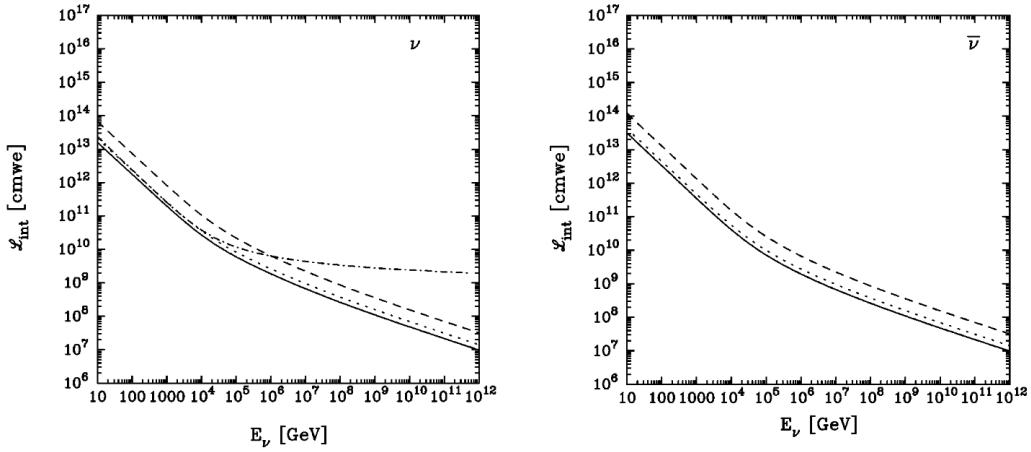

Figure 2.11: *Interaction lengths (in cm water equivalents) of charged-current (dotted line), neutral-current (dashed line), and sum of both (solid line) of ν nucleon interaction (left) and $\bar{\nu}$ nucleon interaction (right). (The dot-dashed curve represents the charged-current interaction length with fixed $Q^2 = 5\ \mathrm{GeV}^2$.) The figure was taken from [66].*

2.3 Atmospheric muons

In addition to atmospheric neutrinos, muons are also produced by the interaction of cosmic rays with the earth's atmosphere. They are the major background contribution for the

analysis presented in section 5. An approximate extrapolation for the atmospheric muon flux according to [111] is

$$\frac{dN_\mu}{dE_\mu d\Omega} \approx \frac{0.14}{\text{GeV s sr cm}^2}\left(\frac{E_\mu}{\text{GeV}}\right)^{-2.7}\left(\frac{1}{1+\frac{1.1E_\mu\cos\theta}{115\text{ GeV}}}+\frac{0.054}{1+\frac{1.1E_\mu\cos\theta}{850\text{ GeV}}}\right), \tag{2.33}$$

in which E_μ is the muon energy and θ its zenith angle. The two terms represent the contributions from charged pions and kaons, respectively. The approximation is valid for ($E_\mu > 100/\cos\theta$ GeV) and $\theta < 70°$, and neglects an additional small contribution from charm and heavier flavors which become more important at higher energies.
The mean number of muons N_μ with an energy $E > E_\mu$ in an airshower produced by a primary of energy E_{prim} and mass A is approximately given by

$$N_\mu(E > E_\mu) = A\frac{E_0}{E_\mu\cos\theta}\left(\frac{E_{prim}}{AE_\mu}\right)^\alpha\left(1-\frac{AE_\mu}{E_{prim}}\right)^\beta, \tag{2.34}$$

where θ is the zenith angle, $\alpha = 0.757$, $\beta = 5.25$ and $E_0 = 0.0145$ TeV, according to [86]. According to this formula, a primary proton with an energy of 1 PeV and $\theta = 0$ produces about 3 muons with $E > 1$ TeV, while an iron nucleus produces about 5.
The properties of the atmospheric muon flux are closely related to the cosmic ray flux. The cosmic ray model, used for the simulation of the atmospheric muons in the later analysis, is therefore briefly summarized in the following.

2.3.1 The Poly-gonato model

The poly-gonato model [81] is a phenomenological model combining the data from direct and indirect measurements of cosmic rays in the energy range from $E = 10$ GeV up to $E = 1$ EeV. Balloon and satellite experiments (see section 2.1.1) can directly measure the element type and energy of a cosmic ray particle and therefore also the cosmic ray flux.
Some experiments which indirectly measure cosmic rays by determining the components of their extensive air showers have been already introduced in section 2.1.1. In these experiments, only indirect quantities such as the mean logarithmic mass $\langle \ln A\rangle = \sum_i r_i \ln A_i$, in which r_i is the relative fraction of nuclei of mass A_i, can be used to describe the cosmic ray mass composition. Different composition hypotheses have been used to fit the data since the cosmic ray composition has large uncertainties at high energies.
The poly-gonato model describes the energy-dependent flux of each cosmic ray element with charge Z by

$$\frac{d\Phi_Z}{dE_0}(E_0) = \Phi_Z^0 \cdot E_0^{\gamma_Z} \cdot \left(1+\left(\frac{E_0}{E_Z}\right)^{\epsilon_c}\right)^{(\gamma_c-\gamma_Z)/\epsilon_c} \tag{2.35}$$

where Φ_Z^0 is the flux normalization and γ_Z the spectral index of the power law. Above the

cut-off energy E_Z, the flux is described by a different power law with slope γ_c. The cut-off energy E_Z is believed to have a rigidity-dependent behavior in the form of $E_Z = E_p \cdot Z$, with $E_p = 4.5$ PeV. The parameter ϵ_c describes how smooth the transition between the two different power laws is. A value of $\epsilon_c = 1$ describes a smooth transition in approximately one decade of energy, while larger values describe harder transitions e.g. $\epsilon_c = 4$ corresponds to a change within 1/5 of a decade. The parameters γ_c and ϵ_c are assumed to be independent of the nucleon's charge Z.
The all-nuclei cosmic ray spectrum can be described by the sum of all the individual nuclei with charge Z

$$\frac{d\Phi}{dE_0}(E_0) = \sum_{Z=1}^{92} \frac{d\Phi_Z}{dE_0}(E_0)\,. \tag{2.36}$$

The spectrum can therefore be described completely by the parameters Φ_Z and γ_Z for each element, which are extrapolated from direct measurements of individual nuclei spectra at energies below 100 TeV. The three parameters, E_p, ϵ_c and γ_c, which are independent of the nuclei charge are determined by fitting the all-particle spectrum determined by indirect measurements. Figure 2.12 shows the average all-particle cosmic ray spectrum and the poly-gonato model.

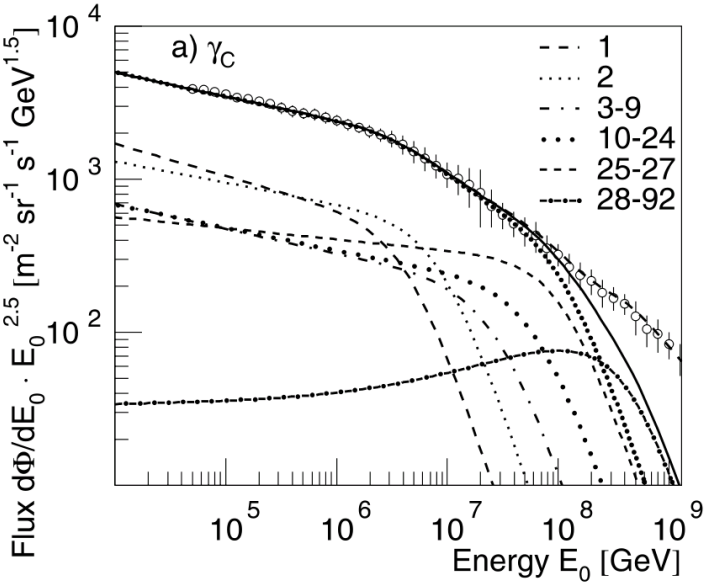

Figure 2.12: *Average all-particle cosmic ray energy spectrum. The solid line through the data points represents the fit of the poly-gonato model (see equation 2.36). The dashed lines show the contributions of groups of elements ($1 \leq Z \leq 28$) to the model. The figure was taken from [81].*

3 The IceCube Experiment

3.1 The IceCube Detector

IceCube is currently the largest and most sensitive high-energy neutrino detector. It is located at the geographical South Pole. The detector construction started in 2005 and was finished in December 2010. With a hot water drill holes were melted in the ice of the South Pole. A string with detectors, known as Digital Optical Modules (DOMs), was deployed in each hole. After about two weeks, the water in the holes was refrozen [16].
The IceCube detector consists of a lattice of 86 strings frozen in the ice. They start at the surface and have a length of about 2500 m. With this length they nearly reach the bed rock under the ice shelf of Antarctica. Each string is equipped with 60 DOMs, with 17 m distance between them. The part of the strings equipped with DOMs is located at a depth between 1450 m and 2450 m. The ice above 1450 m contains too many bubbles, making it much less transparent and therefore less suitable for the experiment. The average horizontal distance between the DOMs is about 125 m. In total, the 5160 DOMs of IceCube fill a volume of about 1 km^3. Figure 3.1 show a schematic of the detector, consisting of 86 the IceCube strings, including the 8 DeepCore strings optimized for lower energies, and the IceTop air shower experiment [14] on top.

The IceCube detector has a neutrino energy threshold of about 100 GeV. The highest energy event measured so far with IceCube had an energy of about 2 PeV ([3]), and therefore illuminated a large part of the detector.
In this dissertation, 335 days of data from May 2009 to May 2010 were used. In this time, the detector only consisted of 59 strings (IC59). This IceCube detector configuration compared to the complete one is shown in figure 3.2.

In the full IceCube detector the DOMs of the central 8 strings have a module density 5 times higher than the rest of the detector, with a horizontal distance of 72 m and a vertical distance of 7 m and a location below 2100 m. They form the so-called DeepCore [11] part of the IceCube detector. The PMTs have a 35% higher quantum efficiency than the standard IceCube DOMs, which together with the clearer ice, leads to a much lower energy threshold of 10 GeV in the DeepCore volume. Thus, DeepCore has a higher sensitivity to study, for example, atmospheric neutrino oscillations [2].
On top of IceCube detector, the IceTop [14] air shower array is located. It measures the muons produced in particle showers which are generated by cosmic ray interactions with the atmosphere. IceTop consists of 162 ice tanks distributed over an area of 1 km^2. Two tanks separated by a distance of 10 m are placed close to the hole of each string. Each tank is filled with frozen water and contains two DOMs. IceTop facilitates the exploration of the cosmic

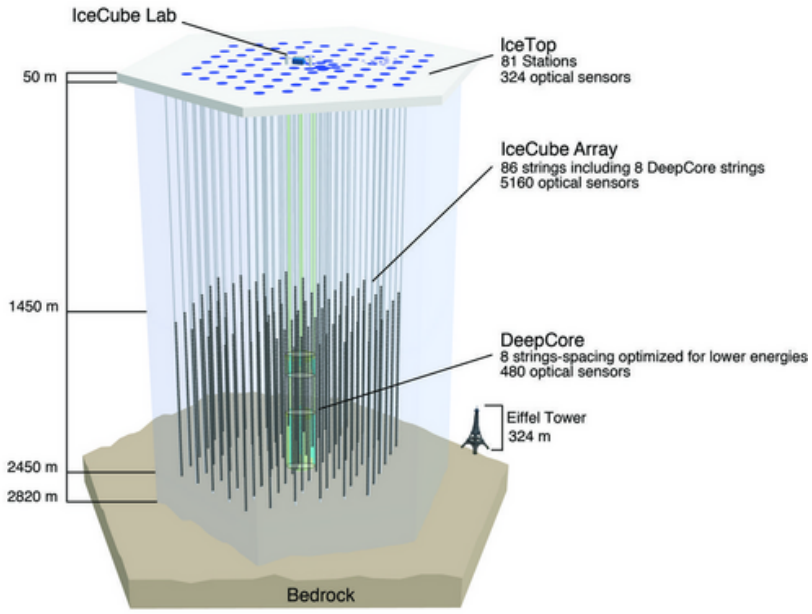

Figure 3.1: *A schematic drawing of IceCube (source: IceCube Collaboration), showing the 86 strings including the 8 DeepCore strings optimized for lower energies, and the IceTop air shower experiment on top. In the depth between 1450 m and 2450 m the strings are equipped with the Digital Optical Modules (DOMs).*

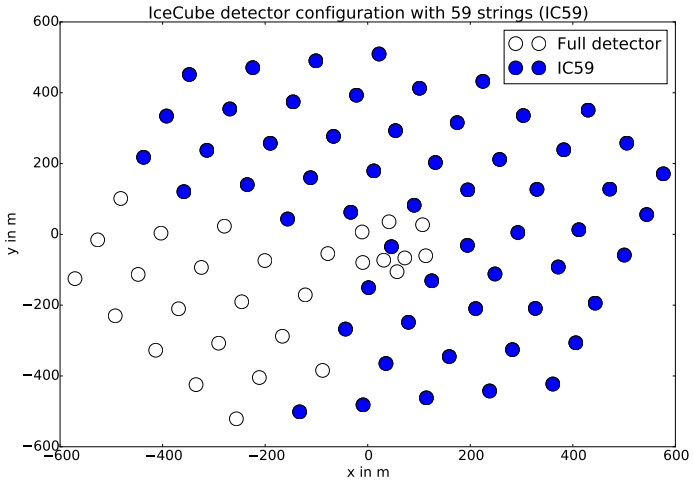

Figure 3.2: *The IceCube detector configuration in the xy-plane showing the 59 deployed strings (blue circles) used in this thesis. The white circles show the remaining strings for the full IceCube detector configuration.*

ray composition in the energy range from 100 TeV up to 1 EeV.

3.2 Particle interactions in the ice

3.2.1 Cherenkov radiation

Neutrinos can interact with nuclei in or close to the detector. In these interactions, secondary particles are produced (see section 2.2.5). The charged particles among them polarize the ambient matter. If the speed $\beta = v/c$ of the charged particles is higher than the speed of light in the medium (with a refraction index n), they emit Cherenkov radiation ([122] as quoted in [111]) under an characteristic angle Θ_C that is defined by

$$\cos\Theta_C = \frac{1}{\beta n}. \tag{3.1}$$

The Cherenkov angle for ice is about 41°. The number of emitted Cherenkov photons per unit distance and wavelength can be calculated by the Frank Tamm formula ([122] as quoted in [111])

$$\frac{d^2N}{dxd\lambda} = \frac{2\pi\alpha z^2}{\lambda^2}\left(1 - \frac{1}{\beta^2 n(\lambda)^2}\right). \tag{3.2}$$

Integrating equation (3.2) in the wavelength range from $\lambda_1 = 300$ nm to $\lambda_2 = 650$ nm (the range in which the DOMs are sensitive, see section 3.5.1) under the assumption that $n(\lambda_1) = n(\lambda_2)$, leads to

$$\frac{dN}{dx} = \int_{\lambda_1}^{\lambda_2} \frac{d^2N}{dxd\lambda} d\lambda \approx 1.5 \cdot 10^6 \, Z^2 \left(1 - \frac{1}{\beta^2 n^2}\right). \tag{3.3}$$

A charged particle ($z = 1$) with $\beta \approx 1$ in ice ($n = 1.31$) emits about $3.4 \cdot 10^4$ Cherenkov photons per m, leading to an energy loss of $dE/dx < 0.14$ MeV/m.

3.2.2 Electromagnetic particle showers

Electromagnetic cascades are created by an interplay of bremsstrahlung and e^-e^+ pair production [111]. A high-energy electron passing through ice can emit a bremsstrahlung photon. A photon traversing ice with an energy higher than at least double the electron rest mass, $E_\gamma > 2m_e$, can produce an e^-e^+ pair. Each process can be described by a typical length scale. The radiation length X_0 is the mean distance over which a high-energy electron loses $1/e$ of its original energy by bremsstrahlung. This is equal to about 7/9 of the mean free path of e^-e^+ pair production by a high-energy photon.

For matter with nucleon number A and atomic number Z, the radiation length can be estimated (according to [111]) by

$$X_0 = \frac{716.4 \text{ g cm}^{-2}\, A}{Z(Z+1)\ln(287/\sqrt{Z})}. \tag{3.4}$$

In ice, the radiation length is $X_0 \approx 36 \text{ g} \cdot \text{cm}^{-2}$, which is about 0.4 m, using the ice density $\rho = 0.92 \text{ gcm}^{-3}$ [33].
In a simple model for an electromagnetic cascade, one neglects the factor of 7/9 and uses the same radiation length X_0 for both processes. Furthermore, one assumes that the energy is always split exactly in half between the particles. Starting with an electron, a bremstrahlung photon is produced, after the first radiation length X_0. After another radiation length this then creates an e^-e^+ pair, while the primary electron produces another bremsstahlung photon. After each X_0, the number of shower particles doubles. Let the primary particle have the energy E_0, then after $t \cdot X_0$, the number of particles $N(t)$ and the energy-per-particle $E(t)$ are

$$N(t) = 2^t, \quad E(t) = \frac{E_0}{2^t}. \tag{3.5}$$

The production of new photons or e^-e^+ pairs continues until the energy-per-particle reaches the so-called critical energy E_c at which the energy loss by bremsstrahlung is equal to the energy loss by ionization. The critical energy in ice is about $E_c \approx 80$ MeV [33]. After t_{max} radiation lengths, the total number of particles N_{max} is

$$t_{max} = \frac{\ln(E_0/E_c)}{\ln 2}, \quad N_{max} = N(t_{max}) = E_0/E_c. \tag{3.6}$$

So the shower length grows logarithmically with the energy of the primary particle and number of shower particles is proportional to the energy of the primary particle. The transverse development of the shower scales with the Molière radius $R_M = 21$ MeV X_0/E_c. In this simplified model an electron with an energy of $E = 1$ TeV produces an electromagnetic shower with a longitudinal length of $t_{max} \cdot X_0 \approx 14 \cdot 0.4$ m ≈ 5 m and a traverse width of $t_{max} \cdot R_M \approx 1.4$ m.
Since the number of shower particles produced is proportional to the energy of the primary particle, also the number of Cherenkov photons emitted (by the charged particles in the shower) is proportional to the primary particle's energy. Therefore, one can estimate the energy of the primary particle by counting the Cherenkov photons emitted in its electromagnetic particle shower.
The longitudinal profile of the deposited energy in an electromagnetic particle shower can be described by ([111])

$$\frac{dE}{dt} = E_0 b \frac{(bt)^{a-1}e^{-bt}}{\Gamma(a)}, \quad a = 2.03 + 0.604\ln(E_0/\text{GeV}), \quad b = 0.633, \tag{3.7}$$

where Γ is the gamma function, t the shower depth in units of X_0 and E_0 the energy of the particle shower. The parameters a and b were obtained by fitting equation 3.7 to simulations of electromagnetic showers [130]. The maximum energy loss of the particle shower occurs at $t_{max} = (a - 1)/b$. Similar to the simplistic particle shower model (see equation 3.6), the mean longitudinal size of the shower increases proportional to the logarithm of its energy. The maximum energy deposition of an electromagnetic cascade with an energy of $E = 10$ TeV occurs at about 4.2 m.
At energies of about $E = 10$ PeV, the Landau-Pomeranchuk-Migdal (LPM) effect [95, 105] reduces the cross sections of pair production and bremsstrahlung. This results in larger radiation lengths of particle showers and therefore larger total elongations. At these energies, the shower length no longer rises logarithmically but roughly with the root of the energy [69]. While the particle shower length at 10 PeV is about 10 m, it is already about 100 m at 100 EeV.
The Cherenkov light yield of electromagnetic particle showers in ice was studied in detail in [130, 115].

3.2.3 Hadronic particle showers

Hadronic particle showers evolve from the hadrons produced out of the nucleon after a neutrino-nucleon interaction (see figure 2.8 and section 2.2.5). The mean energy transferred to the hadronic particle shower (also called hadronic cascade) is about 35% of E_ν for $\bar{\nu}N$ (about 45% for νN) for interactions at neutrino energies of about 1 TeV [65]. At about $E_\nu = 1$ PeV, the mean energy of the hadronic cascade is about about 25% of the neutrino energy, being the same for $\bar{\nu}N$ and νN interactions.
The nuclear interaction length λ_I, which is analog to the radiation length for electromagnetic particle showers, is about 83 g cm^{-2} (about 0.91 m in ice) [33]. This is about twice as large as the radiation length for a electromagnetic cascade. The shower maximum occurs at $t_{max} \approx 0.6 \cdot \ln(E/\text{GeV}) - 0.2$ [56].
Hadronic cascades are more irregular than electromagnetic ones, since the π^0 produced in the hadronic interactions immediately decay into photons and create electromagnetic sub-cascades, leading to fluctuations in the ratio of electromagnetic and hadronic shower components. In addition a part of the energy of the hadronic shower goes into the binding energyof secondary particles, which is not visible. A second important effect is the production of muons from the decay of $\pi^\pm$ or other hadrons. These muons can travel much further than other shower particles.
The Cherenkov light yield for hadronic cascades is smaller than for electromagnetic ones, since a fraction of the energy of the hadronic cascade is used to produce neutral particles e.g. neutrons (not producing Cherenkov light) or is stored as binding energy of hadrons. Simulations of the light yield ratios of electromagnetic and hadronic cascades and a parametrization can be found in [94].

3.2.4 Muons

Muons are produced in atmospheric air showers, in hadronic particle showers and in $\nu_\mu/\bar{\nu}_\mu$ nucleon interactions. Their energy loss in ice can be described by [111]

$$-\frac{dE}{dx} = a(E) + b(E) \cdot E, \tag{3.8}$$

where $a(E)$ describes the energy loss due to ionization and $b(E)$ the energy loss due to bremsstrahlung, e^+e^- pair production and photonuclear interactions. Approximating that $a(E)$ and $b(E)$ are constant, the mean range R_μ of a muon with energy E_0 can be described by

$$R_\mu \approx \frac{1}{b} \ln\left(1 + \frac{bE_0}{a}\right). \tag{3.9}$$

For a muon with an energy of $E = 1$ TeV, the values of $a(E)$ and $b(E)$ in ice are $a \approx 3.1 \cdot 10^{-3}$ GeV cm^2/g and $b \approx 2.96 \cdot 10^{-3}$ cm^2/g [33]. Using equation 3.9, the mean range x_0 of a 1 TeV muon in ice is about 2.5 km. In a complex simulation of muon propagation, 99% of the muons with an energy of 2 TeV (1 PeV) were not yet decayed or stopped after a distance of about 5.5 km (30 km) in ice [42].
In addition to their continuous energy loss, muons can also lose energy in stochastic processes that happen randomly along their tracks. Above a lost energy of $E_{stoch} > 1$ TeV, the stochastic energy losses of muons are dominated by so-called catastrophic bremsstrahlung losses over other types of stochastic energy losses, e.g. e^+e^- pair production [32].
Figure 3.3 shows the probability of a muon producing a cascade with at least an energy of $E_{casc,max}$, in a stochastic loss event. A muon with an energy of between 30 TeV and 50 TeV has a probability of about 40% to produce a cascade with an energy of 10 TeV.

The Cherenkov light yield of muons with stochastic energy losses differs from that of a pure muon. These differences were studied in Wiebusch [130].
An electromagnetic cascade produced by the catastrophic bremsstrahlung loss of a muon is hard to distinguish from a cascade produced by a neutrino interaction. The ability to distinguish between these two event classes depends on the amount of Cherenkov light emitted along the muon track. A part of the event selection presented in section 5 was particularly developed to reject this event class of muons as efficiently as possible.

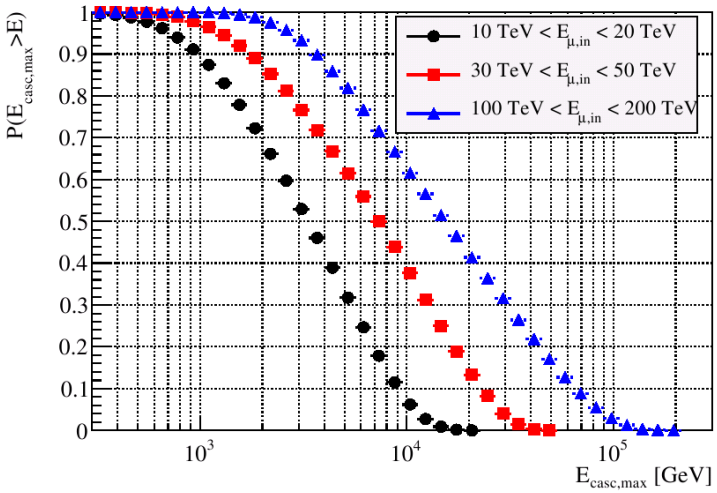

Figure 3.3: *Probability P for a stochastic loss of a muon with energy E_μ to create a cascade with an energy larger than $E_{casc,max}$ within the IceCube detector volume. The plot is based on a simulation with Muon Monte Carlo (see section 4.1.1) and was taken from [30].*

3.3 Light propagation in ice

The following description is based on Ackermann et al. [17], in which more information can be found. A recent publication about new models to describe the ice properties within the detector is Aartsen et al. [84].
One of the reasons to build IceCube at the South Pole is that glacial ice is the most transparent natural medium in the wavelength range between 200 nm and 400 nm. In general, there are air bubbles in ice, which reduce its tranparency. After a depth of 1350 m, all of these bubbles are converted to non-scattering air hydrates and the ice reaches its maximum transparency. Measurements from the IceCube precursor experiment, AMANDA [23], showed that the optical properties of the ice below a depth of 1500 m depend mainly on the concentration of dust in the ice.
Two main mechanisms are important for the propagation of light in the ice, namely scattering and absorption. Both can be described by a typical effective length scale after which the photon survival probability drops to 1/e for absorption or after which the photon is scattered. In the intrumented region of IceCube, the effective absorption length ranges from about 40 m to 150 m and the effective scattering length ranges from 6 m to is 40 m, varying strongly with depth.

3.3.1 Scattering

Light scattering in Mie theory is decribed as the scattering of light on small spherical masses of material with a different refractive index to that of the surounding material. In the IceCube detector, these scattering centers are mainly dust grains with typical sizes of the order of a

few μm. Other contributions come from sea salt crystals, liquid acid drops and soot.
Let λ_s be the geometrical scattering length, which is the average distance between two scatters. $\langle \cos\Theta \rangle$ denotes the average of the cosine of the scattering angle Θ. For $\langle \cos\Theta \rangle > 0$, the scattering is preferentially forward and for $\langle \cos\Theta \rangle = 0$ the scattering is forward-backward symmetric. For the South Pole ice, scattering is preferentially forward with $\langle \cos\Theta \rangle = 0.94$. A beam of light moving through the ice is scattered in successive steps of λ_S with an average angle $\langle \cos\Theta \rangle$ between two steps. After i steps, the light beam traveled $\lambda_S \langle \cos\Theta \rangle^i$ in the initial direction. The total effective length of the light propagation is the sum over all steps

$$\lambda_e = \lambda_s \sum_{i=0}^{n} \langle \cos\Theta \rangle^i \tag{3.10}$$

which for large n becomes

$$\lambda_e = \frac{\lambda_s}{1 - \langle \cos\Theta \rangle}. \tag{3.11}$$

Alternatively, the reciprocal from λ_e - the effective scattering coefficient $b_e = 1/\lambda_e$ can be used. The left plot of figure 3.4 shows the effective scattering coefficient of the ice as a function of the light wavelength and the depth of the ice.

3.3.2 Absorption

The absorption of photons in a medium can be described by the length λ_a after which the survival probability drops to 1/e. Alternatively the absorption coefficient or absorptivity, which is the reciprocal of λ_a

$$a = \frac{1}{\lambda_a} \tag{3.12}$$

can be used. The main contribution to the absorptivity come from mineral grains and soot. The right plot of figure 3.4 shows the absorptivity of the ice as a function of the photon wavelength and the depth of the ice.

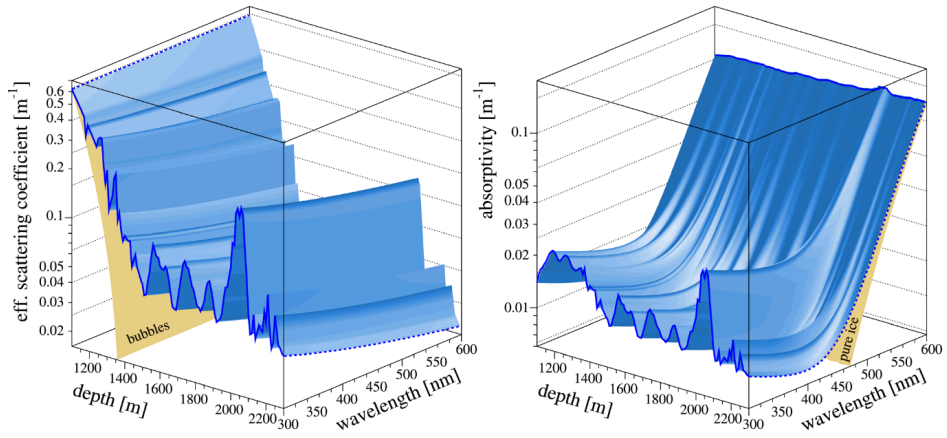

Figure 3.4: *Effective scattering coefficient and absorptivity as functions of depth in ice and the photon wavelength. The figure was taken from [17].*

3.4 Event topologies

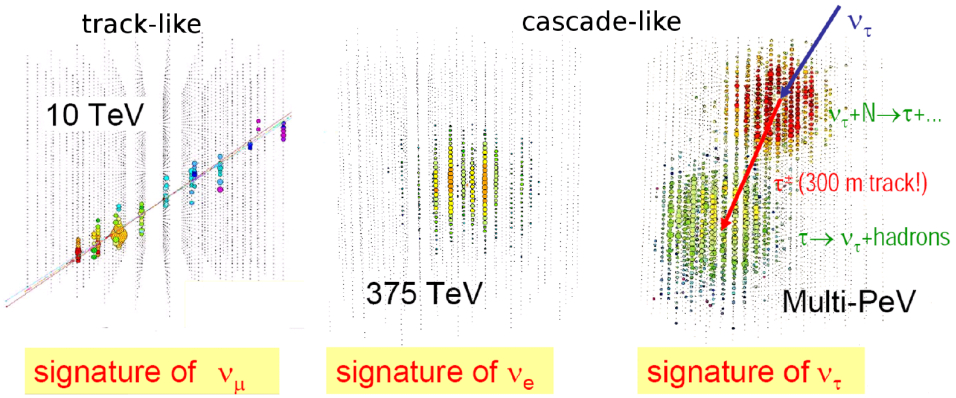

Figure 3.5: *Event topologies of different simulated neutrino interactions in the detector. Charged current interactions of $\nu_\mu, \bar{\nu}_\mu$ with nucleons in the ice create track-like event patterns. Charged current interactions of $\nu_e, \bar{\nu}_e, \nu_\tau, \bar{\nu}_\tau$ and neutral current interactions of all neutrino flavors create cascade-like event patterns. The figure was taken from [103].*

There are two main event topologies in the IceCube detector: track-like and cascade-like event patterns. Both topologies are shown in figure 3.5.
Track-like event patterns are caused by the Cherenkov light emitted along the track of high-energy muons moving through the detector (see section 3.2.4). These muons can either be of atmospheric origin or were created in a charged-current interaction of $\nu_\mu, \bar{\nu}_\mu$. The high-energy muons move with about the speed of light (in vacuum) through the ice, and therefore, so does the point of Cherenkov light emission. The scattering of the Cherenkov

photons in the ice diffuses the tracks and can delay the arrival of the Cherenkov photons at the DOMs, but the overall track-like pattern is conserved. Track-like events have a very good direction resolution in the order of 1°, due to their well-defined trajectories.
Cascade-like event patterns are caused by the charged-current interactions of $\nu_e, \bar{\nu}_e, \nu_\tau, \bar{\nu}_\tau$ and neutral-current interactions of all flavors. However, they can also be created by a muon with a catastrophic bremsstrahlung loss (see section 3.2.4). The sizes of the electromagnetic and hadronic particle showers of cascade-like events are small (see sections 3.2.2 and 3.2.3) compared to the horizontal DOM distances (see section 3.1). Therefore, they appear as almost static and point-like sources of Cherenkov radiation. The emitted Cherenkov photons propagate through the ice and are scattered. The original anisotropic Cherenkov light emission of the particle shower is transformed into a nearly spherical hit pattern. Simulations show that for a cascade with an energy of 100 TeV in a distance of 50 m, the anisotropy of the Cherenkov light emission is visible up to hundreds of ns, but after about 600 ns of the Cherenkov light propagation its pattern is already isotropic [101]. Cascade-like events that are fully contained within the detector volume have a very good energy resolution (about 15%), because all their energy is deposited in the detector.
A particular event signature, consisting of two cascades, can be created by a charged current interaction of a very-high-energy $\nu_\tau/\bar{\nu}_\tau$ with a nucleon in the detector (see the right event pattern of figure 3.5). At the interaction point of the tau neutrino, a hadronic cascade is created. The tau created in the interaction has a decay length of about 50 m per PeV (of its energy) [48]. If the tau decays in the detector, it produces a second cascade. This event class has not yet been observed in IceCube.

3.5 Data Acquisition (DAQ)

The DOMs [75] are the heart of the IceCube detector. They are equipped with a large PMT to collect the Cherenkov photons produced by the secondary charged particles from the neutrino interactions. Each DOM has its own digitization and trigger units, and can communicate with close-by DOMs on the same string. If a trigger decision is made, the data is sent over cables inside the string to the IceCube labaratory (ICL) where the information is further processed and stored. Other cables within the string provide the power for the DOMs.
The following short summay of the IceCube data acquisition system follows Abbasi et al. [12].

3.5.1 The DOM architecture

Each DOM consists of a pressure resistant 13 mm thick glass sphere, which houses the PMT and the electronic boards (see figure 3.6). An improved optical coupling between the PMT and the glass sphere is achieved with a flexible gel interface. The DOMs are filled with nitrogen at a pressure of $1/2$ atmosphere. A mu-metal cage within the DOMs shields the cathode and first dynodes of the PMT from the magnetic field of the earth.
Each DOM is equipped with a 25 cm diameter Hamamatsu R7081-02 PMT, sensitive between

300 nm and 650 nm and with a quantum efficieny of 25% [8]. The dark rate is about 300 Hz at −27 degree, which is the temperature in the deep ice. At lower temperatures, radioactive decays of K^{40} from the PMT glass as well as the glass sphere dominate the dark rate, while for higher temperatures, the cathode thermionic emission dominates. The PMT consists of 10 dynode stages, which reach a gain of 10^7 at 1300 V. This gain results in a pulse height of 8 mV for a single photon, which is above the electronic noise level (0.1 mV).
Additionally, the Main Bord (MB) of each DOM is equipped with 12 flasher LEDs which produce bright UV pulses that can be detected by other DOMs. Each of these LEDs can emit 10^{10} photons per flash at a wavelength of 405 nm with a pulse width of 10 - 100 ns. They can emit light either individually or in combination. The pulse lengths and the amplitudes of the flashes are programmable. This can be used to simulate physical events and to study the behavior of reconstruction algorithms, to calibrate distant DOMs and also for studies of the optical properties of the ice.

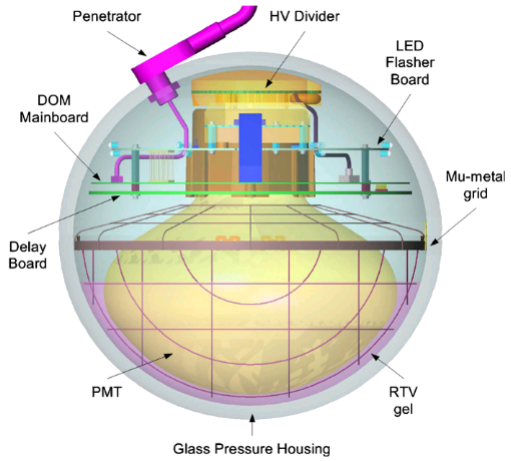

Figure 3.6: *A schematic view of a DOM. The figure was taken from [12].*

3.5.2 Pulse readout and digitization

Figure 3.7 shows a scheme of the data processing on the DOM MB. If one or more photons are detected by the PMT and the 0.25 single photoelectron (SPE) pulse height is reached, a pulse readout is triggered by a high-bandwith discriminator. A 75 ns delay line provides enough time for the downstream electronics to receive the trigger from the discriminator.
After passing the delay line, the signal is amplified by three independent amplifiers with amplifications factors of 16, 2 and 0.25. Each of these amplifiers sends its signal to one of the analog inputs of the active Analog Transient Waveform Digitizers (ATWDs).[1] Each input has an analog memory that stores 128 samples at a sampling rate of 300 Hz.
If a trigger signal is received, the amplified signals are digitized, otherwise, they are discarded.

[1] Two alternating ATWD units are used to avoid dead time when one of them is read out; while one is processing input signals, the other is ready for input capture.

The digitization is done by 128 Wilkinson 10-bit common-ramp analog-to-digital converters (ADCs) internal in the ATWD. After the conversion, the sample with the amplification of 16 is transferred to a Field Programmable Gate Array (FPGA) first. If an overflow occurs in this channel, the sample with the amplification factor of 2 is digitized. If an overflow also occurs in this channel, the sample with the amplification factor of 0.25 is used. On average, the ATWD needs 29 μs to digitize a waveform after capture.
The ATWD digitization system has a time window of 450 ns. It is supplemented by a 10 bit Flash ADC (FADC), which is running at 40 MHz and has 10 bit resolution per sampling. It is able to digitize the response of the PMT over 6.4 μs.

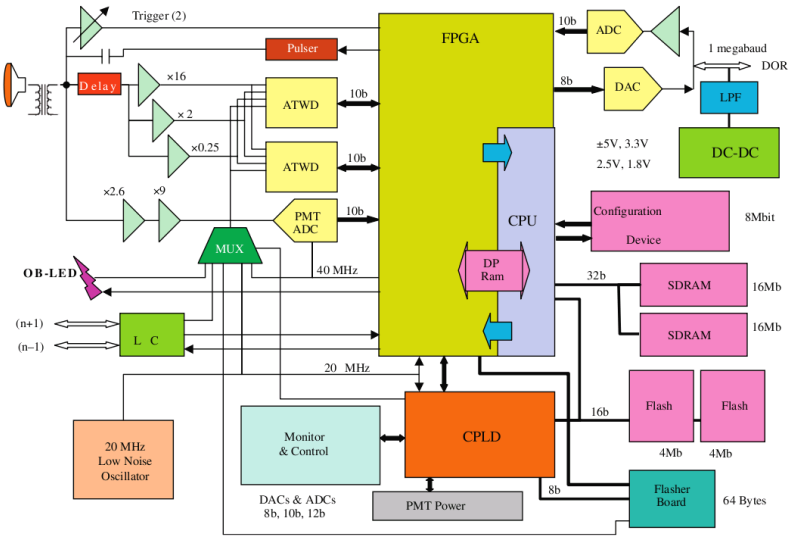

Figure 3.7: *Layout of the DOM Main Board. The figure was taken from [12].*

3.5.3 Trigger

A DOM is only read out when a sufficient number of DOMs fullfil the so-called hard local coincidence (HLC) condition, which is that two or more DOMs which are nearest or next-nearest neighbors on the same string record hits within a time window of $\pm 1\mu$s. The readout control and the trigger logic are done with a FPGA. The software can be updated after the deployment of the DOMs in the ice, which allows future changes and updates.
The main IceCube trigger requires that at least 8 DOMs have HLC hits in a time window of 5 μs, therefore, it is called Simple Majority Trigger (SMT8). If this condition is fullfilled, the data from the DOMhubs[2] is read out in a time window of ± 10 μs around the trigger time. DOMs which have hits in the trigger time window but do not satisfy the HLC condition are also included in the read out. These hits are called soft local coincidence (SLC) hits.

[2]The DOMhubs are PCs, which receive the data from the DOMs and send control commands to them. Each string has it own DOMhub.

This trigger condition reduces the noise rate significantly and leads to a trigger rate of about 1.6 kHz in the IC59 detector configuration.

3.5.4 Data processing and storage

The SMT8 trigger calculation takes place in the ICL on the surface of Antartica. Furthermore, the data is filtered with the so-called Online Filter (see section 5.1) to reduce the data volume. The reduced data sample is then sent over satellite directly to the IceCube headquarters in Madison, Wisconsin. The rest of the data is shipped later on tapes.

3.5.5 Feature extraction

On the raw data the so-called `FeatureExtractor` is run, before the OnlineFilter is applied. The raw data coming from the DOMs are called waveforms and contain the measured charge of the PMT as a function of the time. The waveforms are calibrated by subtracting their baselines and removing the droop, an undershot in the waveform caused by the PMT circuit. The calibrated waveforms are stored and can be used as input for event reconstructions. However, there are reconstructions that do not operate on calibrated waveforms, but instead on the arrival times and the number of Cherenkov photons. Since the shape of a single photoelectron pulse in the PMT is known, the `FeatureExtractor` can unfold the so-called `RecoPulses` from the waveform. Details about the `FeatureExtractor` configuration, that was used for the data sample in this thesis, can be found in [104].

4 Simulation

The analysis described in section 5 is based on a comparison between measured and Monte Carlo (MC) simulated data. The assumed signal consists of astrophysical neutrinos following an E^{-2} power-law. The flux normalization per flavor is chosen as $dN/dE \cdot E^2 = 1.0 \cdot 10^{-8}\,\mathrm{GeV\,s^{-1}\,sr^{-1}\,cm^{-2}}$. The background events are muons and neutrinos originating from the interaction of cosmic rays with the atmosphere.
The simulation is done in several steps. At the beginning, muons or neutrinos are produced with so-called generators. These generate particles according to a given spectrum in some energy range. They also propagate the simulated particles through the atmosphere or the earth (in case of neutrinos). In the next step, the interaction of the particles in the detector volume is simulated and the secondary particles that are created in that step e.g. muons, are propagated. All particle showers generated in interactions of the primary particles or their secondaries are simulated.
In the next step, the Cherenkov photons produced by the muons and particle showers are propagated through the ice, taking into account scattering and absorption (see section 3.3). If the Cherenkov photons reach a DOM, the number of photoelectrons produced is calculated. Additional photoelectrons originating from the DOM's noise are added to the simulation. After the determination of the number of photoelectrons in the cathode of the PMT, the DOM's response is simulated. If the DOM trigger condition is fulfilled, its data is read out. The fulfillment of the individual DOM trigger condition is checked for all DOMs. Based on that, the detector trigger condition of the full detector is determined. If the event fulfills the detector trigger condition, it is saved and is passed on to the next filter level (see section 5). The simulation chain is described in greater detail below.

4.1 Neutrino simulation

For the simulation of neutrino interactions around the IceCube detector, the `NuGen` module is used, which is able to simulate neutrinos and antineutrinos of all flavors in a wide energy range. Its fundamental physics are based on the All Neutrino Interaction Generator (ANIS) [67].
Neutrinos are injected with a parametrized angular and energy distribution (e.g. the conventional atmospheric spectrum (see section 2.2.4) or the isotropic astrophysical spectrum (see section 2.2.3)), and propagated through the earth. For the density profile of the earth, the Preliminary Earth Model [54] is used.
In the next step, they are forced to interact in a pre-defined volume around the detector. This makes the simulation process more efficient. This forced interaction is taken into account

by an interaction probability weight (P_{int}) which the simulated neutrinos are given. The secondaries of the interaction are saved and passed on to the propagation algorithms.

4.1.1 Muon Monte Carlo

The simulation of muons and taus are handled by the Muon Monte Carlo (MMC) program [42]. This program also handles the tau decay. MMC simulates a muon's energy losses due to ionization, bremsstrahlung, photo-nuclear interaction and pair production when traveling through matter. It takes into account continuous as well as stochastic energy losses. MMC has an energy range from 106 MeV (muon rest mass) up to 100 EeV.

4.1.2 Cascade Monte Carlo

The Cascade Monte Carlo (CMC) program handles the simulation of electrons and hadronic showers. Neutrino-induced cascades below an energy of 1 TeV are simulated as point-like light sources, which emit Cherenkov light with the profile of an electromagnetic particle shower [115]. Cascades that have a higher energy are split into sub-cascades for further simulation. The smaller amount of Cherenkov light production of hadronic cascades (see section 3.2.3) as well as the LPM effect (see section 3.2.2) are taken into account by CMC.

4.2 Atmospheric muon background simulation

The simulation of the atmospheric muons is based on the poly-gonato model of the cosmic ray flux (see section 2.3.1). The simulation of the atmospheric muon background in two different ways is described in the following sections.

4.2.1 Polygonato Corsika

According to the poly-gonato model, atmospheric particle showers are simulated with the Corsika code (COsmic Ray SImulations for KAscade) [45, 46]. High-energy muons ($E > 400$ GeV) are produced in the development of these showers. They are able to reach the IceCube detector, and are the main source of background of the IceCube experiment.
After the primary particle with typical properties such as nuclei type, direction and energy has been drawn from the polygonato cosmic ray flux model, Corsika propagates the shower through the atmosphere. All muons from the shower are passed to MMC. The rest of the simulation chain follows the overview given in section 4.
It can happen that two or more atmospheric muons simultaneously move through the detector, trigger it and are recorded in the same event. The rate of coincident muon events is at least about a factor of 10 smaller than the single muon rate (see section 5.4 and section 5.5).
The Polygonato Corsika was used as a cross-check for the more flexible Five Component Corsika generation scheme (see section 4.2.2) for the single muon simulation in this thesis.

Coincident muons were simulated with the polygonato generation scheme, since the Five Component Corsika generation scheme cannot create these events.

4.2.2 Five Component Corsika

The polygonato generation scheme has some disadvantages for the practical use of the simulated data for example, challenges in reweighting it to other cosmic ray models. Another problem is the steep cut-off in the primary energy at about 100 PeV, which results in low statistics for highly energetic events in the spectrum of cosmic rays. Another point is the fixed number of simulated primaries of each chemical element, which is not optimal for an efficient production of the simulation.
To simplify the simulation production and to address the problems mentioned above, only five dominant element groups are simulated, from which the name Five Component Corsika originates. These groups are Hydrogen, Helium, Nitrogen (representing all elements with $Z = 3...9$), Aluminium (representing all elements with $Z = 10...25$) and Iron. The relative contribution of the elements in the simulation production can be chosen freely for optimization purposes.
The Five Component Corsika generation scheme does not simulate a spectrum as in the poly-gonato model. Instead, it can generate the five primary nuclei with an arbitrary power-law spectrum $dN/dE = N_0 \cdot E^{-\gamma}$, with $\gamma > 1$. The next step of the simulation calculates a weight w for each event. The application of the weights leads to a power-law spectrum with index 0, which then can be reweighted to any model. In this thesis, the events are reweighted according to the poly-gonato model.
With the freedom to choose the index γ of the simulation spectrum and the ratio of the primary particles, the simulation production can be optimized. This optimization is discussed in the next section.

4.2.3 Optimized Production of Five Component Corsika

The standard production scheme for the Five Component Corsika has an element ratio of $H : He : N : Al : Fe = 10 : 5 : 3 : 2 : 1$, with a spectral index of $\gamma = -2$ in the energy range from 600 GeV to 100 EeV. Studies done within the IceCube collaboration [108] show that it would take about 32 years on 1000 CPUs to generate enough Five Component Corsika events in order to obtain event statistics matching or exceeding one year of IceCube livetime with a threshold energy of $E_{prim} > 30$ TeV.
An optimization study [106] was performed in order to try to significantly reduce the required CPU time. Different values of the index of the production spectrum γ, the energy range and the element ratio have been studied with respect to their influence on the necessary CPU time.
As a result of this study, the generation spectrum index was changed to $\gamma = -2.6$, the element ratio adjusted to $H : He : N : Al : Fe = 3 : 2 : 1 : 1 : 1$ and the energy range adjusted to 32 TeV to 1 EeV for proton primaries. This leads to an acceptable computing time of about 80 days on 1000 CPUs.

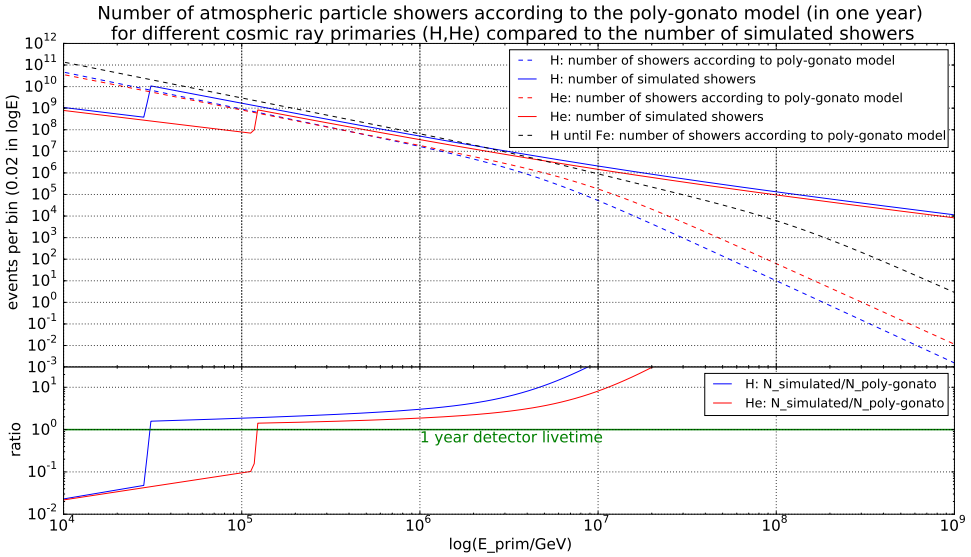

Figure 4.1: *Number of produced particle shower (per energy bin) by different cosmic ray primaries in the interaction with the atmosphere in a livetime of one year compared to the number of simulated particle showers for this analysis. The dashed blue line shows the number of Hydrogen (H) events in one year livetime according to the poly-gonato model [81]. The solid blue line shows the number of Hydrogen events in the simulated sample. The lower plot shows the ratio of the number of produced particle shower and the number of simulated events. For primary energies of $E \gtrsim 30$ TeV, the number of simulated Hydrogen events exceeds the prediction for one year of detector livetime. The same is plotted for Helium (He). Since the muon production in the shower scales with the primary energy per nucleon, there is an offset for He in the (total) primary energy.*

Figure 4.1 shows the number of particle showers produced in the interaction of different cosmic ray primaries with the atmosphere as a function of the primary's energy. The fluxes of the cosmic ray primaries were taken from the poly-gonato model. This is compared to the number of shower event, which were simulated for the muon background simulation for the analysis of this thesis.
The ratio of the median energy of a parent nucleon of cosmic rays to the minimum energy of the muon, which is produced by the interaction of the parent nucleon with the atmosphere, is about 8 for $E > 6$ TeV [86]. Therefore, a nucleon with an energy of 30 TeV produces a muon with a minimum energy of about 4 TeV. Since for a threshold energy of $E_{prim} > 30$ TeV, a livetime of one year for the simulation of the atmospheric muon background is reached, this threshold energy is sufficient for the simulations of muons with energies of $E_\mu \approx 10$ TeV.
Due to the optimized Five component Corsika generation, this analysis was the first one that exceeded a livetime of one year for the atmospheric muon simulation.

4.3 Simulation of light propagation with PHOTONICS

The Cherenkov light emitted by muons and hadronic or electromagnetic showers has to be propagated through the ice. Since the scattering and absorption of the Cherenkov photons are random processes, the photon propagation has to be simulated. This is done by a software package named PHOTONICS [96].
PHOTONICS is used to create tables of timing and amplitude distributions of Cherenkov photons dependent on the geometry between emitter and receiver. It uses an ice model which contains the scattering and absorption coefficients (see section 3.3) as functions of the depth of the light source in the ice, and the wavelength of its radiation.
After the PHOTONICS tables were generated for an ice model, the light yield and arrival time distributions of Cherenkov photons from cascades or muons can be taken from the tables. Therefore, no real-time photon propagation for each simulated event is necessary.
The tables can be used for event reconstruction as well, where they provide the arrival time probability density functions as well as the expected number of detected photons for specific event hypotheses (e.g. cascades or muon tracks, see section 3.4).

5 Analysis

This analysis searches for the diffuse astrophysical neutrino flux in the IC59 (see section 3.1) data set. The astrophysical neutrinos must be separated from the huge atmospheric background, which is vastly dominated by atmospheric muons. The muons create track-like signatures in the detector. Neutrinos created in the atmosphere are an additional but much weaker contribution to the background. They can only be distinguished on a statistical basis from the astrophysical neutrinos by their different energy spectrum (see sections 2.2.3 and 2.2.4).
In order to avoid a confirmation bias, the analysis was developed on a 10% subsample (about 34 days) of the 335 days of IC59 IceCube data. After a collaboration review, the analysis was applied to the remaining 90% of the data (see section 5.6.1).
The signal channel, for the search of astrophysical neutrinos in this thesis, are neutral-current interactions from ν_e, ν_μ and ν_τ, and charged-current interactions from ν_e and ν_{tau}. They produce cascade-like signatures in the detector.
The data sample consists of about $5 \cdot 10^{10}$ atmospheric muons, while a number of 10 - 100 neutrino events is expected in the final event selection of the data sample, according to a previous analysis [5]. Therefore, the analysis must remove the background as much as possible, without removing too much of the signal. This is achieved by using the different physical properties of the events as well as the detector responses, to discriminate between signal and background. For example, the variable distributions differ between cascade-like and track-like events, as does the geometrical hit pattern in the detector. These differences between the two event classes are exploited in the event selection, in order to reduce the large number of background events and to select only well-reconstructed neutrino candidate events.

The complete event selection is grouped in different smaller event subselections called levels. Each level consists of certain cuts on different variables. Arranging the event selection in levels allows to provide a common basis for analyses, to take into account limits in the data transfer rate or in the available computing power. For example, some more complex event reconstructions need a lot of cpu power and therefore, they can only be run on an already reduced data sample.
The different levels and the variables on which they are based are introduced in the following sections. Figure 5.1 gives an overview of the steps of the event selection.
The Trigger Level is the raw data stream from the detector (see section 3.5.3). Level 1, also called the Online Filter, is a basic filter in order to preselect cascade-like events at the South Pole. The reduced data rate can then be transmitted over satellite. Different working groups within IceCube apply different preselections on events. At Level 2, additional event reconstructions are added that need more computational power than is available at the South

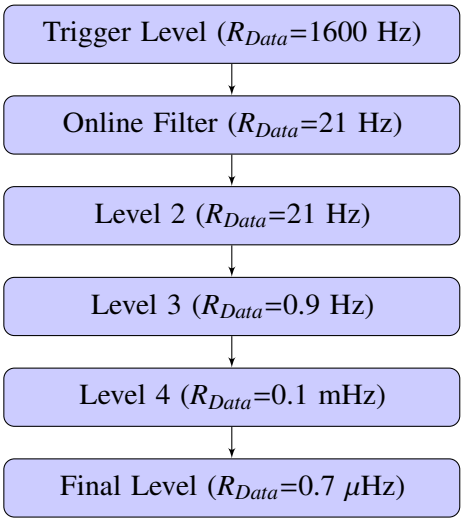

Figure 5.1: *A flow chart diagram of the event selection and data rate R_{Data}. The different cut levels are explained in detail in the text.*

Pole. Level 2 is a common level for most of the different IceCube analysis channels. The Level 3 filter selects again cascade-like events and reduces the number of background events. The size of the cascade Level 3 data sample is small enough, that is can be downloaded in a reasonable time from IceCube members world-wide. The analysis of this thesis is based on the Level 3 cascade event selection.
The Level 4 and Level 5 event selections were developed especially for this thesis' analysis. The Level 4 event selection consists of containment and quality cuts. The containment condition rejects cascade-like events close to or on the boundary of the detector. The quality cuts reject poorer quality events that would be difficult to reconstruct accurately, e.g. small events triggering very few strings.
On this reduced data sample a computational expensive, iterative event reconstruction is applied. Furthermore, the Level 5 event selection reduces the number of background events to about the number of signal events. The events, which pass this event selection, constitute the final sample.
After the Level 5, a cut and count analysis (see section 5.6) based on an additional energy cut of $E > 38$ TeV, which removes most of the remaining background and predicts the smallest average upper limit, is applied to the remaining 90% of the data sample, after the approval of an internal collaboration review.
A likelihood fit is applied to the full data sample in order to further investigate it. The likelihood fit consists of templates for the expected signal and background energy distributions. Their sum is fitted to the energy distribution of the data events to constrain the model parameters of the templates. The likelihod fit is described in detail in section 6 and its results are discussed.

5.1 Level 1 - Online Filter

The following description of the Level 1 - Online Filter event selection for cascade like events is based on the Cascade Online Filter Proposal [104]. The goal of the Level 1 event selection is to reduce the experimental data rate of about 1600 Hz, which is dominated by muons, down to a rate of about 21 Hz, which can be processed with the existing cpu power and bandwidth. In relative numbers, 1.5% of the experimental data (mainly background) are kept while the signal efficiency is about 78% (for $E > 1$ TeV) for an expected E^{-2} power-law electron neutrino flux. The signal efficiency is even higher (81%) when considering only events which are contained within the detector.
The Level 1 filter is based on the event shape variable `Tensor of Inertia`, the first guess track reconstruction `LineFit velocity` and the likelihood fit `Muon Likelihood Fit`, which are briefly introduced in the following.

5.1.1 Tensor of Inertia

Analogous to classical mechanics where the tensor of inertia of a rigid body is defined by the masses and their distance to the center of gravity, the `Tensor of Inertia` (`ToI`) [21] reconstruction is defined by the amplitudes in the hit DOMs. It is calculated via

$$I^{kl} = \sum_i A_i \left(\delta^{kl} \vec{r}_i^{\,2} - r_i^k r_i^l \right), \tag{5.1}$$

where A_i is the number of photoelectrons seen in the DOM at position $\vec{r}_i$ and δ^{kl} is the Kronecker symbol. In the next step the eigenvalues λ_1, λ_2 and λ_3 of the `ToI` are calculated. The smallest eigenvalue is always denoted as λ_1. From the eigenvalues one can calculate the eigenvalue ratio

$$r_{ToI} = \frac{\lambda_1}{\lambda_1 + \lambda_2 + \lambda_3}. \tag{5.2}$$

The different geometrical patterns of signal and background events result in different distributions of eigenvalue ratios r_{ToI}. For muon tracks the smallest eigenvalue is close to zero which results in $r_{ToI} \approx 0$. Cascade-like events are more spherical and therefore all their eigenvalues are about the same. Therefore, their distribution's maximum tends to $r_{ToI} \approx 1/3$ (see figure 5.2).

5.1.2 LineFit

`Line Fit` [21] was developed as a first guess algorithm for muon track reconstructions. It ignores the optical properties of the ice and the geometry of the Cherenkov cone, and it assumes that the light travels with a velocity $\vec{v}$ through the detector. Therefore, the positions of the DOMs $\vec{r}_i$ (hit at time t_i) can be connected by a line described by $\vec{r}_i \approx \vec{r} + \vec{v} \cdot t_i$. One can

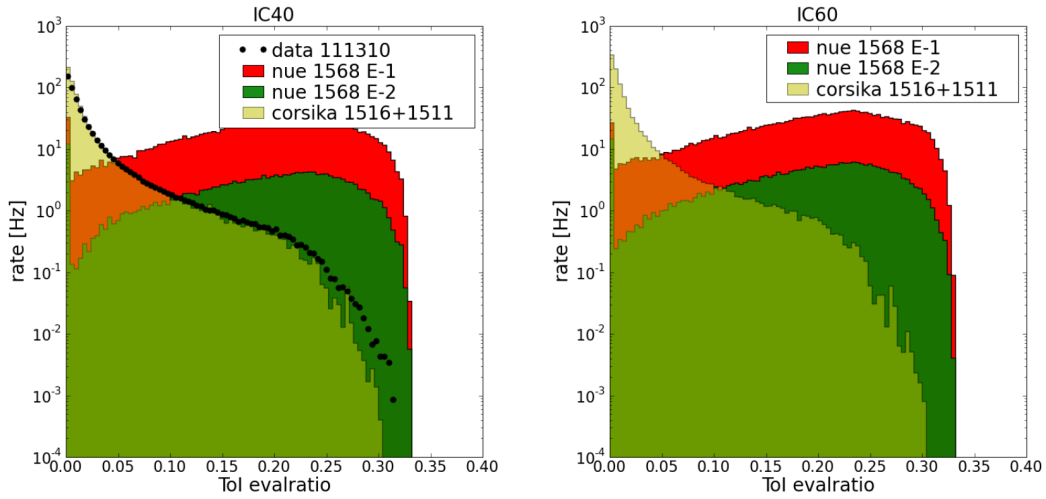

Figure 5.2: *The distributions of the* `Tensor of Inertia` *eigenvalue ratio on Trigger Level (taken from [104]). The simulated muon background is drawn in light green and the experimental data for IC40 in black. The simulated signal (electron neutrinos) with a simulated generation spectrum of E^{-2} is shown in green. The flux normalization of both is in arbitrary units chosen for a better presentation. One can see that cascade-like events tend to have eigenvalue ratios up to $1/3$, while the background distribution peaks at 0 (these values are explained in the text). The left plot shows the distribution for IC40 detector configuration while the right one shows the prediction for IC60 at the time of the study. (One string less than planned was deployed, therefore, the detector became IC59.)*

define

$$\chi^2 = \sum_i (\vec{r}_i - \vec{r} - \vec{v} \cdot t_i)^2, \tag{5.3}$$

with the free fit parameters $\vec{r}$ and $\vec{v}_{LF}$. The minimum of the χ^2 function can be calculated analytically

$$\vec{r} = \langle \vec{r}_i \rangle - \vec{v}_{LF} \cdot \langle t_i \rangle \quad \text{and} \quad \vec{v}_{LF} = \frac{\langle \vec{r}_i t_i \rangle - \langle \vec{r}_i \rangle \langle t_i \rangle}{\langle t_i^2 \rangle - \langle t_i \rangle^2}, \qquad \langle x_i \rangle = \frac{1}{N} \sum_{i=1}^{N} A_i^w x_i. \tag{5.4}$$

A_i is the amplitude in the DOM at location $\vec{r}_i$. The calculation of the weighted average can be altered with the weight w.
Since muons travel with approximately the speed of light through the ice, their `Line Fit velocity` $v_{LF} = |\vec{v}_{LF}|$ is rather high. Cascade-like events are located at the neutrino interaction vertex and therefore have smaller v_{LF} values. Figure 5.3 shows the distribution of v_{LF} for background (Corsika) and signal.

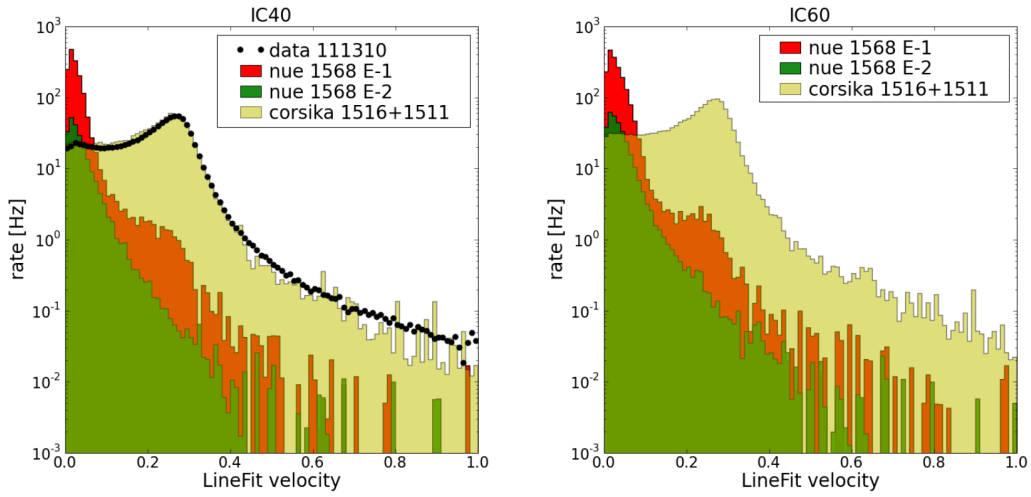

Figure 5.3: *The distribution of the* `LineFit velocity` v_{LF} *in m/ns on Trigger Level (taken from [104]). The simulated muon background is drawn in light green and the experimental data for IC40 in black. The simulated signal (electron neutrinos) with a simulated generation spectrum of* E^{-2} *is shown in green. The flux normalization of both is in arbitrary units chosen for a better presentation. One can see that the rate for cascade-like events peaks at zero and falls strongly for higher values of* v_{LF}*. The background distribution peaks at about* $v_{LF} = 0.3$ *m/ns which is the speed of light. The left plot shows the distribution for IC40 detector configuration while the right one shows the prediction for IC60 at the time of the study. (One string less than planned was deployed, therefore, the detector became IC59.)*

5.1.3 Pole Muon Likelihood Fit

The `Pole Muon Likelihood Fit` is a likelihood-based muon track reconstruction (see [21]) seeded with the result from `LineFit`. It was originally developed for AMANDA ([83]) - the precursor experiment of IceCube at the South Pole - and was reimplemented within IceCube. This likelihood reconstruction is based on the arrival time of hits in the DOMs. Due to scattering in the ice, the arrival of the Cherenkov photons in the ice is delayed. It can be described by the residual time

$$t_{res} = t_{hit} - t_{geo} \tag{5.5}$$

which is the difference between the time, the photon hits the DOM t_{hit} and the geometrical time t_{geo}, a Cherenkov photon needs to travel directly and without scattering from the muon to the DOM. The residual time has to be taken into account to provide a reasonable event reconstruction. The normalized probability density function (PDF) of the residual time can

be parametrized with the so-called Pandel function [112].

$$p(d,t) = \frac{1}{N(d)} \frac{\tau^{-(d/\lambda)} t_{res}^{(d/\lambda-1)}}{\Gamma(d/\lambda)} \cdot e^{-\left(t_{res}\cdot\left(\frac{1}{\tau}+\frac{c_{medium}}{\lambda_a}\right)+\frac{d}{\lambda_a}\right)} \tag{5.6}$$
$$N(d) = e^{-d/\lambda_a} \cdot \left(1 + \frac{\tau \cdot c_{medium}}{\lambda_a}\right)^{-d/\lambda}$$

wherein the parameters λ_a, λ and τ can be interpreted as an absorption length, a scattering length and a scattering time, respectively (see [94]). The parameter values can be obtained by fitting equation 5.6 to a full photon Monte Carlo simulation [94, 121]. c_{medium} is the speed of light in the ice, d the distance between DOM and the emission point on the muon track and $\Gamma(d/\lambda)$ the Gamma function. Changes in the scattering and absorption depending on the depth of the ice are neglected by the Pandel function (see section 3.3).
Since the parametrization in equation 5.6 does not consider electronic jitter and PMT effects it has to be modified to $\tilde{p}(d,t)$ by introducing Gaussian smearing with width σ_{jitter} (for details see [94]). With the help of this modified Pandel PDF, the following likelihood can be constructed

$$L = \prod_{i=1}^{\text{all hits}} \tilde{p}(d,t), \qquad L' = \frac{-\log(L)}{N_{hit\ DOMs} - 5}, \tag{5.7}$$

where 5 is the number of free paramters for a muon track reconstruction. By finding the minimum of L', one can determine the muon track parameters $(\Theta, \Phi, \vec{r}_0, t_0)$. The reconstructed zenith angle Θ of the muon track is used for the Level 1 event selection. It is called $\Theta_{PoleTrackLlh}$ from now on. Figure 5.4 shows the distribution of $\cos(\Theta_{PoleTrackLlh})$.

5.1.4 Level 1 Event Selection

The Level 1 cascade event selection [104] consists of two branches and is based on the variables r_{ToI}, v_{LF}, and $\cos(\Theta_{PoleTrackLlh})$ described above. The number of strings n_{string} and the number of DOMs n_{chan}, which have detected Cherenkov light are also used.
The original cascade event selection is given by

$$cut1 = \left(v_{LF} < 0.077 \frac{\text{m}}{\text{ns}}\right) \wedge (r_{ToI} > 0.066) \wedge (n_{chan} \geq 8)\,. \tag{5.8}$$

In order to increase the event selection efficiency for lower energy events, an alternative selection criterion for events, which were only seen by a few strings, can be applied

$$cut2 = \left(v_{LF} < 0.095 \frac{\text{m}}{\text{ns}}\right) \wedge (\cos(\Theta_{PoleTrackLlh}) < 0.225) \wedge \left(n_{string} \leq 5\right) \wedge (n_{chan} \geq 10)\,. \tag{5.9}$$

The final level 1 event selection is the logical OR of the two cases

$$cut1 \vee cut2. \tag{5.10}$$

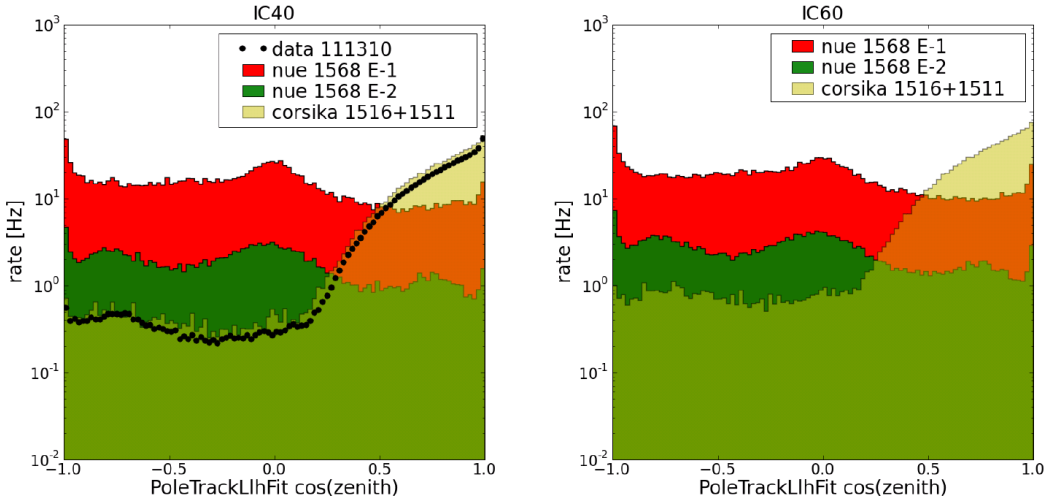

Figure 5.4: *The distribution of the cosine of the zenith angle* $\cos(\Theta_{PoleTrackLlh})$ *of the* `Pole Muon Likelihood Fit` *(taken from [104]). The simulated muon background is drawn in light green and the experimental data for IC40 in black. The simulated signal (electron neutrinos) with a simulated generation spectrum of* E^{-2} *is shown in green. The flux normalization of both is in arbitrary units chosen for a better presentation. The data rate and Corsika rate are maximal for down-going muons* $\cos(\Theta_{PoleTrackLlh}) = 1$*. The rate decreases with increasing zenith angle until* $\cos(\Theta_{PoleTrackLlh}) = 0$ *(horizontal muons) and stays constant for even larger zenith angles. The left plot shows the distribution for IC40 detector configuration while the right one shows the prediction for IC60 at the time of the study. (One string less than planned was deployed, therefore, the detector became IC59.)*

Figure 5.5 shows the parameter space of the Level 1 event selection variables for the signal and background simulations.
Compared to the Level 1 filter applied to IC40 data, the signal efficiency for electron neutrinos (E^{-2}) is increased from 70% to 78%. This results in a data rate of 21 Hz (previous year 16 Hz) leading to a data transfer volume of 8.5 GB per day.

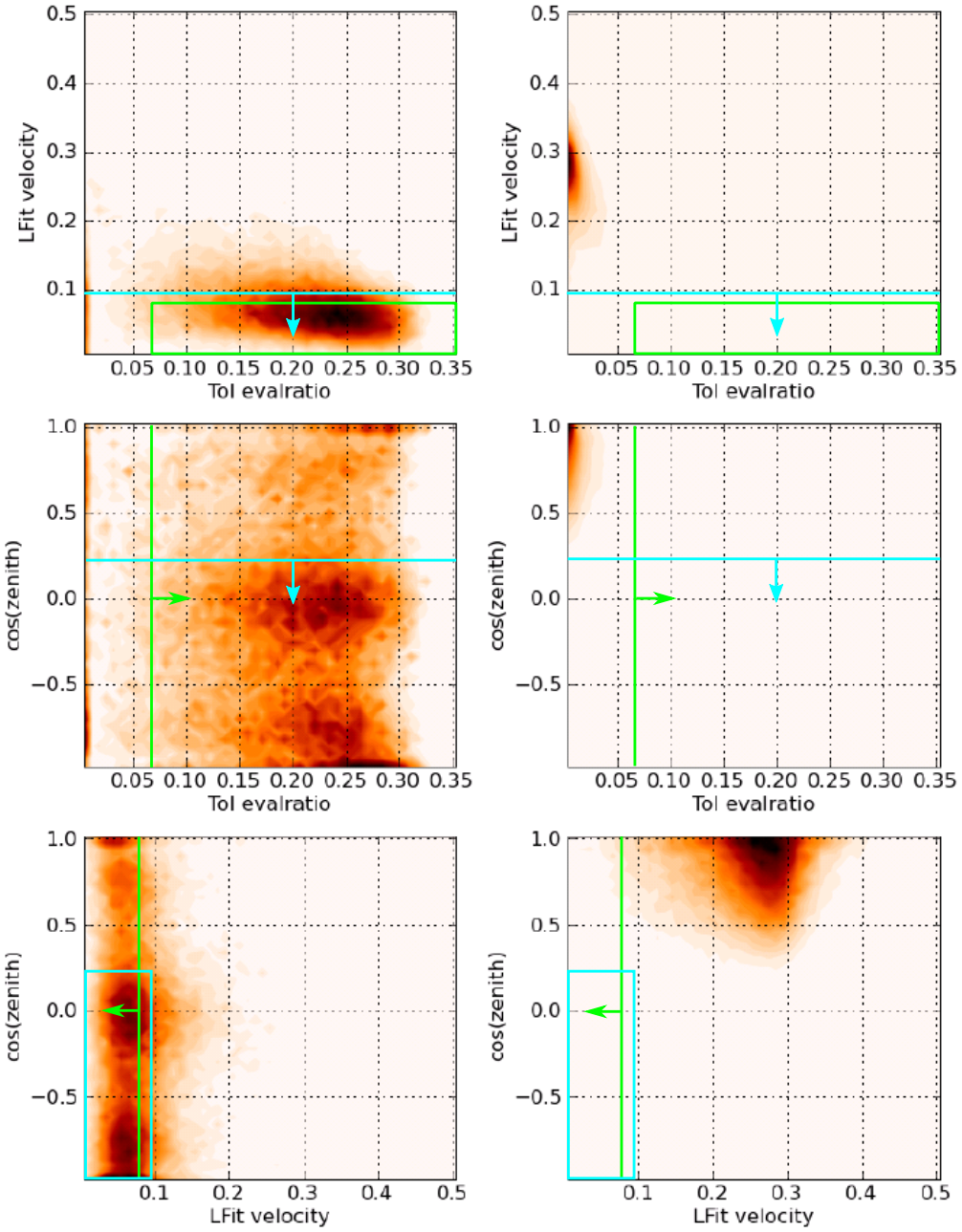

Figure 5.5: *The parameter space of the Trigger Level event selection variables* `ToI` *eigenvalue ratio,* `LineFit velocity` *(v_{LF}) and the cosine of the zenith angle Θ from the* `Pole Muon Track likelihood`*. Distributions for a simulated electron neutrino flux with a spectrum of E^{-2} are shown on the left hand side, while distributions for the muon background simulation are shown on the right hand side. The cut values from cut1 (see equation 5.8) are shown by green lines, and those from cut2 (see equation 5.9) by turquoise lines. The arrows indicate the parameter space accepted by the cut.*

5.2 Level 2 - Offline Processing

The Level 2 processing provides the IceCube collaboration with a comon standard of high level reconstructions of all IceCube events passing the Online Filter. At Level 2, no further event selection is applied and no separation of the different event streams is performed. Additional computational expensive event reconstructions are calculated for either a cascade-like event hypothesis or a muon-like event hypothesis. Among those for a cascade-like event hypothesis is the energy reconstruction ACER (see section 5.3.2) which takes into account the depth-dependent ice properties and which is used for the Level 3 event selection as well as the Cascade Likelihood Vertex Fit (see section 5.3.1). An important muon-like event hypothesis variable for the Level 3 event selection is the Single Photoelectron Fit (SPEFit, see section 5.3.3), which is also computed in the Level 2 processing.

5.3 Level 3

The goal of the common cascade Level 3 is a further reduction of the background with the highest possible signal efficiency. This allows to perform computationally expensive, complex event reconstructions on the remaining sample, which are used in later event selections. The common cascade Level 3 filter is developed and provided by the cascade working group within IceCube ([13]). The Level 3 is only applied to events from the cascade-like event filter stream. The events from all the other data streams, which were still present in the Level 2 are rejected. The data rate is further reduced to about 0.9 Hz, which corresponds to a reduction factor of about 23 with respect to the Level 1 cascade filter (see section 5.1).
The following variables are used for the event selection: the Atmospheric Cascade Energy Reconstruction (ACER), the zenith angle of the Single Photoelectron Fit (SPEFit8), the reduced log-likelihood (rlogl) value of the Cascade Likelihood Vertex Fit and the Fill Ratio Mean.

5.3.1 Cascade Vertex Likelihood Fit

The Cascade Vertex Likelihood Fit (CVLF) [10, 94] was originally developed for AMANDA ([83] and reimplemented for IceCube. It is based on the same likelihood function as the Pole Muon Track Likelihood reconstruction (see section 5.1.3).
The two reconstructions differ in their assumed event hypotheses and correspondingly in the coordinate system used (see [59]). For a cascade-like event hypothesis, the coordinate system is based on the interaction vertex. For a muon event hypothesis reconstruction like the Pole Muon Track Likelihood, the coordinate system is comoving with the muon. The distances are measured perpendicular to the muon track and the time delays are calculated based on the position of the muon when the Cherenkov light is emitted.
From the minimum of the likelihood function of Cascade Vertex Likelihood Fit, one obtains an estimate for the interaction vertex of the event. Addtionally, a variable called the reduced log likelihood $rlogL_{CVLF}$ is calculated. It is a measure of how well the cascade

hypothesis matches the event pattern. Furthermore, it shows a strong separation power (see figure 5.20) to differentiate between cascade-like events and track-like events.

5.3.2 ACER

`ACER` (see [49]) is a fast and simple energy estimator taking into account the glacial ice characteristics. The PHOTONICS tables (see section 4.3) are used to describe the propagation of the Cherenkov light to the DOMs. In the case of no noise, the energy can be calculated analytically by

$$\frac{E}{\mathrm{GeV}} = \frac{\sum_i n_i}{\sum_i \mu_i(\vec{r})} \tag{5.11}$$

where n_i is the number of photoelectrons recorded by the ith DOM and $\mu_i(\vec{r})$ is the number of photoelectrons predicted by the PHOTONICS tables for this DOM based on the event vertex $\vec{r}$. Therefore, the energy estimation only depends on the number of photoelectrons measured by each DOM. The event vertex is provided by the Cascade Vertex Likelihood Fit (see section 5.3.1).
Taking into account noise with a rate R (in Hz) over a time window T (in s) the equation 5.11 becomes

$$-\sum_i \frac{n_i}{\frac{E}{\mathrm{GeV}} + \frac{R \cdot T}{\mu_i(\vec{r})}} + \sum_i \mu_i(\vec{r}) = 0. \tag{5.12}$$

This equation has no analytical solution anymore, but can be solved numerically.

5.3.3 Single Photoelectron Fit (SPEFit)

The `Single Photoelectron Fit` (`SPEFit`) is a likelihood reconstruction for muon tracks similar to the `Pole Muon Track Likelihood` (see section 5.1.3). The main difference is that the fit is repeated iteratively 8 times, which means that fit results are used as a seed for the next fit iteration. The zenith angle of `SPEFit8` likelihood reconstruction $\Theta_{SPEFit8}$ is used for the Level 3 event selection.

5.3.4 The Credo reconstruction

`Credo` is a likelihood reconstruction algorithm for cascade-like events. The following brief description of `Credo` is based on [101, 5], in which more details can be found. `Credo` describes events with the following parameters

$$C = (t_0, x, y, z, \Theta, \Phi, E), \tag{5.13}$$

where t_0 is the time of the interaction in the detector, (x, y, z) are the spatial coordinates of the interaction, Θ is the zenith angle, Φ the azimuth angle of the interacting particle (Θ is defined to be zero for vertically downgoing particles) and E is the energy which is

deposited in the detector by the particle interaction. To be more specific, E is the energy of an electromagnetic particle shower which emits the amount of light observed in the detector.[1] For each IceCube event, the number and arrival times of photoelectrons measured by each DOM is recorded. So for each DOM there is a so-called pulse series, the time-ordered number of photoelectrons per DOM in the event. These pulse series contain all the available information of an event and are the basis for the event reconstruction. The set of all pulse series is the detector response R and can be written as

$$R = (t_{ki}, \Delta t_{ki}, n_{ki}), \tag{5.14}$$

where the index i runs over the bins of the pulse series of the kth DOM. n_{ki} is the number of photoelectrons in the time interval Δt_{ki} that begins at the time t_{ki}. The likelihood used for Credo assumes a Poisson distribution for the number of photoelectrons in each bin of the pulse series. With the help of the PHOTONICS tables [96], the expected number of photoelectrons μ_{ki} in ith bin of the pulse series of the kth DOM can be calculated in the following way

$$\mu_{ki}(\vec{x}_k, t_{ki}, C) = \left(\langle \mu_k^\infty \rangle \frac{dP}{dt}(\vec{x}_k, t_{ki} - t_{geo} - t_{cscd}) + \nu_{noise} \right) \Delta t_{ki}. \tag{5.15}$$

In this equation $\frac{dP}{dt}$ is the delay time probability density function which describes the number of Cherenkov photons arriving at different times due to scattering and absorbtion in the ice. It depends on the DOM position $\vec{x_k}$ and on the time t_{ki}, which is the time when the Cherenkov photons arrive at the kth DOM in the ith bin of the pulse series. Without scattering, the Cherenkov photons would need the geometrical time $t_{geo} = |\vec{x}_{cascd} - \vec{x}_k|/c_{ice}$ to propagate through the ice. $\langle \mu_k^\infty \rangle$ is the time-integrated flux of Cherenkov photons at the kth DOM in units of measured photoelectrons. The noise rate of the DOMs is described by the term ν_{noise}.
With the Poisson distribution one can calculate how likely it is to measure n_{ki} entries in a pulse series for an expectation of μ_{ki}. Multiplying the probabilities for all bins of a pulse series and for all DOMs one obtains the following likelihood:

$$L = \prod_{\substack{DOMs \\ k}} \prod_{\substack{bins \\ i}} \frac{\mu_{ki}^{n_{ki}}}{n_{ki}!} \exp(-\mu_{ki}) \tag{5.16}$$

By taking the negative logarithm of the Likelihood equation 5.16 becomes:

$$-\ln L = \sum_{\substack{DOMs \\ k}} \left[\mu_k - \sum_{\substack{bins \\ i}} \left(n_{ki} \ln \left(\frac{\mu_{ki}}{\mu_k} \right) - \ln(n_{ki}!) \right) - N_k \ln(\mu_k) \right] \tag{5.17}$$

In this equation N_k is the number of photoelectrons recorded by the kth DOM and defined by $N_k = \sum_i n_{ki}$. The term μ_k, defined by $\sum_i \mu_{ki} \approx \langle \mu_k^\infty \rangle + \nu_{noise} \Delta t_{event}$, denotes the number of

[1] Neutrino interactions have a hadronic component that emits slightly less light at a given energy.

expected hits from the PHOTONICS tables plus the number of noise hits (both in units of photoelectrons).
The improvement of the `Credo` likelihood compared to the `Cascade Vertex Fit` likelihood implementation for example (see [101, 5]) is that it describes the expected number of photons and their arrival time with PHOTONICS [96] tables (which include depth-dependent change in the optical properties of the ice) instead of the Pandel parametrizations [112].
The minimization of the likelihood $-\log L$ is done within the GULLIVER likelihood framework. The seed parameters for the Level 3 `Credo` reconstruction are assembled from different simpler event reconstructions. The time and the vertex position are taken from the `Cascade Vertex Likelihood Fit` reconstruction, the direction is taken from the `Tensor of Inertia` reconstruction and the energy from the `Atmospheric Cascade Energy Reco` (see [119]).
There are two possible options for likelihood minimization. The I3SimpleFitter takes the seed values and performs the minimization in one step. The second option is the I3IterativeFitter, in which the minimization is done iteratively. In each step the minimizer starts from a different starting point in the parameter space. For example, in the Level 3 reconstructions, a `CredoFit` with 4 iterations is done. In Level 4 an additional `CredoFit` with 8 iterations is calculated. Since these additional iterations are computationally expensive, they can be only applied on higher cut levels.

5.3.5 FillRatioMean and FillRatioRMS

The `FillRatioMean` and the `FillRatioRMS` [13, 113, 77] are topological variables exploiting the different hit patterns of muon tracks and cascade-like events. They are both a measure of how spherical an event appears. For an event vertex $\vec{r}$ (obtained from `Credo`, see section 5.3.4), one can calculate the radii r_{mean} and the root mean square r_{RMS} averaged over all hit DOMs in the event

$$r_{mean} = \langle |\vec{r} - \vec{r}_i| \rangle_{i \in \text{hit DOMs}}, \qquad r_{RMS} = \sqrt{\langle (\vec{r} - \vec{r}_i)^2 \rangle_{i \in \text{hit DOMs.}}} \tag{5.18}$$

These radii can be addtionally multiplied with a scale factor, which can increase the discrimination power between cascade-like events and muon tracks. For r_{Mean} the scale factor $a = 1.1$ was used, while for r_{RMS} the scale factor $b = 3.4$ was used [120]. The fill ratios `FillRatioMean` and `FillRatioRMS` are then defined as the number of hit DOMs within the radius r_{Mean} or r_{RMS} around the vertex

$$FillRatioMean = \frac{N_{hit\ DOMS}(a \cdot r_{Mean})}{N_{all\ DOMS}(a \cdot r_{Mean})}, \quad FillRatioRMS = \frac{N_{hit\ DOMS}(b \cdot r_{RMS})}{N_{all\ DOMS}(b \cdot r_{RMS})}. \tag{5.19}$$

Cascade-like events are expected to have fill ratios close to one, because their Cherenkov light is spherically distributed around the interaction vertex and therefore most of the DOMs around the vertex within the distance r_{Mean} or r_{RMS} should see it. On the other hand, muon tracks only iluminate DOMs close to their track and therefore are expected to have smaller fill ratios in general.

5.3.6 Level 3 Event Selection

The Level 3 event selection (see [120]), consists of two steps. In the first step, events belonging to one of two different branches of equation 5.20 are selected.

$$\begin{aligned} &E_{ACER} > 10 \text{ TeV} \quad (I) \\ &(\Theta_{SPEFit8} > 80\,^{\circ}) \wedge (rlogL_{CVLF} < 10) \quad (II) \end{aligned} \tag{5.20}$$

The first branch (I) just selects all events which have an energy $E_{ACER} > 10$ TeV, since lower energy events are even more dominated by the atmospheric background.
The second branch (II) selects all events which have a zenith angle $\Theta_{SPEFit8} > 80\,^{\circ}$, corresponding to those which are upgoing or parallel to the horizon. An addtional requirement is that these events have a small reduced likelihood value $rlogL_{CVLF} < 10$ so that they fit acceptable to the cascade event hypothesis.
The `Credo` reconstruction is applied to all events that fulfill the selection of either branch I or branch II. The vertex obtained from `CredoFit` is then used for the calculation of `FillRatioMean`. Figure 5.6 shows the distributions for data, signal and background for `FillRatioMean`.

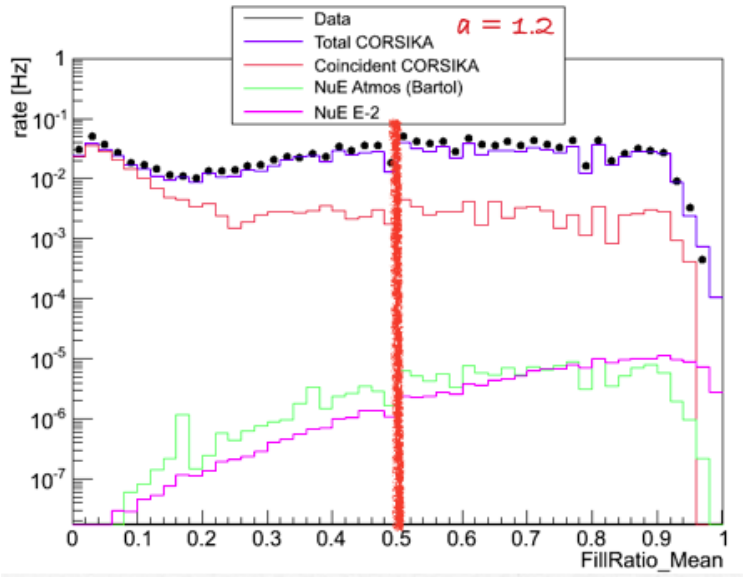

Figure 5.6: *The distribution of the variable* `FillRatioMean` *after the application of the cuts defined in equation 5.20. The black data points show the data, the purple line shows the simulated atmospheric muon background and the pink line shows the simulated astrophysical E^{-2} electron neutrino signal. The red line shows the coincident atmospheric muon events and the green line the atmospheric electron neutrinos. The thick red vertical line marks the cut value (see equation 5.21). In this analysis* `FillRatioMean` *is calculated with a=1.1 (see section 5.3.5) following optimization studies. The plot is taken from [120].*

The second step of the Level 3 event selection is

$$FillRatioMean > 0.5. \tag{5.21}$$

With this cut, additional background events are rejected.
Figure 5.7 shows the distribution of $\Theta_{SPEFit8}$ as a function of E_{ACER} for the Level 3 event selection.

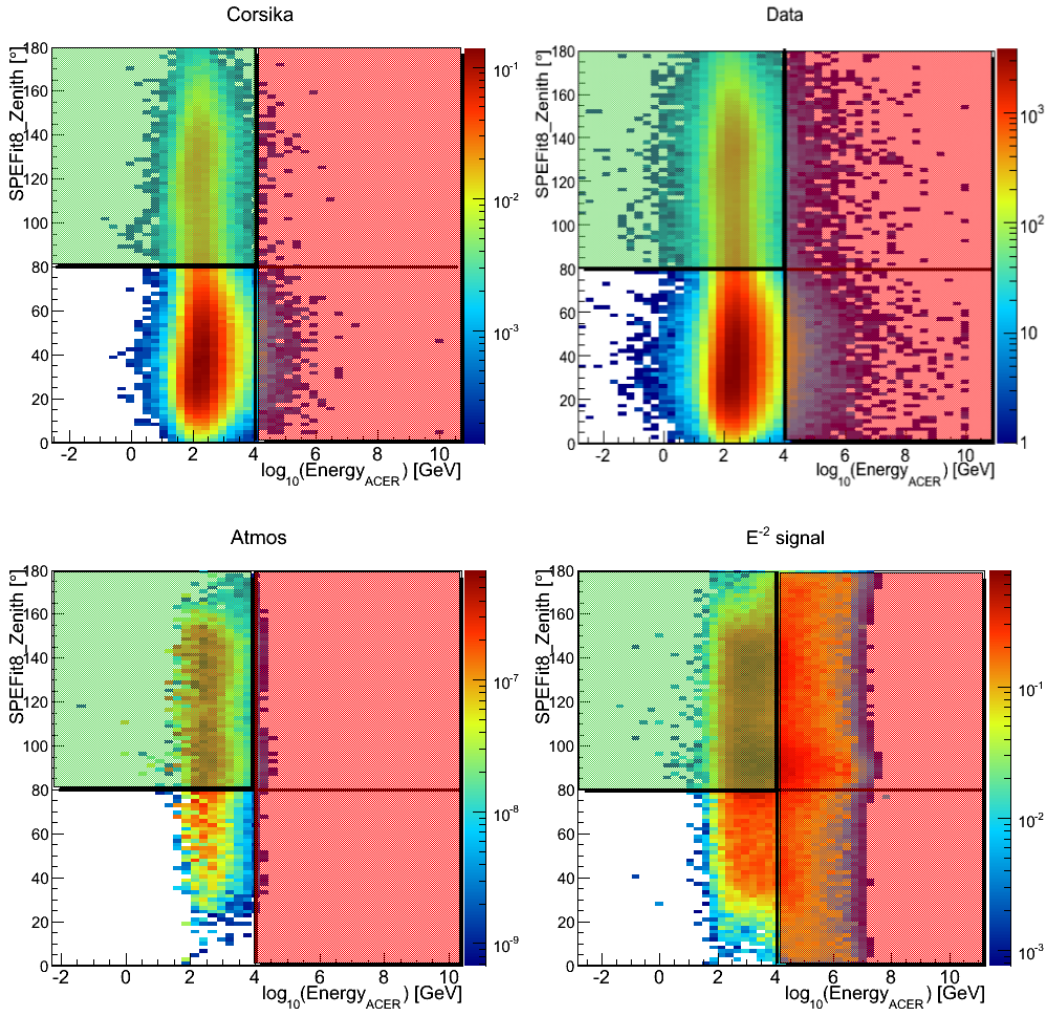

Figure 5.7: *The two dimensional distributions for the Level 3 selection of $\Theta_{SPEFit8}$ and E_{ACER} for Corsika (upper left), data (upper right), atmospheric neutrino background (lower left) and signal (ν_e, lower right). The red marked region is the branch of high energy events (I in 5.20) while the green region is the low energy upgoing events branch (II in 5.20). The plot was taken from [120].*

With the application of the Level 3 cuts 74% of the simulated neutrino signal is kept while the data rate is reduced by a factor of about 23. The ratio between Data and Corsika and atmospheric neutrino background is about 1.22 after the Level 3 cuts. Table 5.1 shows the signal efficiency and the reduction of background and data for the Level 3 cuts.

	Level 2 rate (Hz)	Level 3 rate (Hz)	passing efficiency
Data	20.9	0.9	4%
Corsika	20.3	0.74	4%
atmos ν background	$2.80 \cdot 10^{-4}$	$1.44 \cdot 10^{-4}$	51%
$\nu_e\ E^{-2}$	$2.84 \cdot 10^{-6}$	$2.10 \cdot 10^{-6}$	74%

Table 5.1: *The passing rates of the Level 3 event selection. The numbers are taken from [120].*

5.4 Level 4 - Containment and Quality Cuts

The Level 4 event selection criteria and above were developed individually for this analysis. The aim is to arrive at a data sample which is almost free of atmospheric muons, the dominant background for the search for a diffuse neutrino signal. Such a data set allows the search for an excess above the expected atmospheric neutrino background. The astrophysical neutrino flux is assumed to be distinguishable from the atmospheric one, for a sufficiently large statistical sample, due to the different energy spectra of atmospheric and astrophysical neutrinos. However, this is only possible if the atmopsheric muon contamination is insignificant.
Atmospheric muons passing through a large part of the detector produce a clear muon track, and can therefore be distinguished from the typical cascade-like event patterns caused by neutrino interactions in the detector. But muons can sneak in from the detector boundaries or only pass a short distance through the detector e.g. through some detector corner. Such muons may produce too few light in the detector to be able to identify their track. Furthermore, they may undergo catastrophic bremsstrahlung losses within the detector which look similar to the signature of a neutrino interaction. In this case, the muons essentially constitute a irreducible background, so the event selection must reduce the number of incoming muons as much as possible.
In order to remove this class of events, containment cuts have been developed based on ideas from a previous IC40 analysis (see [5]). These cuts reject all events which have hits in the DOMs very close to the detector boundaries or have their first hit on a boundary DOM. These criteria form the Level 4 event selection together with additional cuts on the quality of the event reconstruction. The main idea of Level 4 is to retain only well-reconstructed events completely contained within the IceCube detector. The event selection and the variables on which it is based, will be described in the following.
Furthermore, only cascade-like events which are completely contained in the detector are expected to have a good energy resolution since all of their energy is deposited in the detector.

If an event lies on or beyond the border of the detector, part of its light pattern may be lost and the event reconstructions may not work properly. To avoid this, such events are not considered in this analysis. Regardless of their rejection in this analysis, another current IceCube analysis [97] investigates the possibility to expand the event reconstructions beyond the detector borders.

5.4.1 Vertex Containment

The Vertex Containment is based on the event vertex coordinates (x, y, z) obtained by the `Credo` likelihood reconstruction (see section 5.3.4).
Figure 5.8 shows the IceCube detector configuration IC59. Each dot represents a deployed string with 60 DOMs. The red dots represent strings which are on the outer layer of the detector. The green line is used to decide whether the event, according to its vertex coordinates (x, y), is contained within the detector or not. Uncontained events are rejected. Tightening the polygon beyond the green line to the next inner layer of strings would result in a loss of 44% sensitivity.

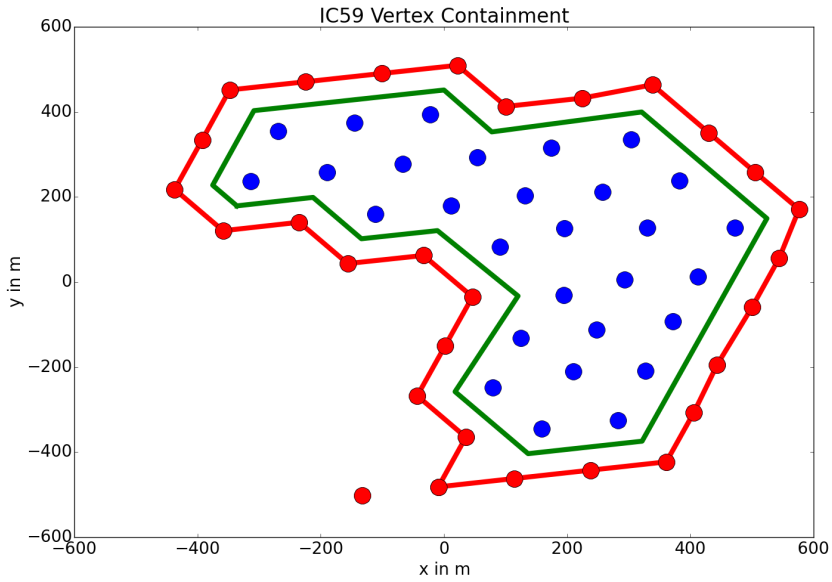

Figure 5.8: *The IC59 detector configuration in the x-y-plane. Each dot represents an IceCube string with 60 DOMs. The red dots represent the outer layer of DOMs (layer 2). The green line is the polygon which marks the boundary inside which the vertex of the event is considered to be within the detector in the x-y-plane.*

Additionally, it was required that the z vertex coordinate of a event must be at least 50 m below the upper most DOM and at least 50 m above the lower most DOM to pass the selection, i.e. -450 m $<$ z $<$ 450 m (z=0 is defined to be half the vertical height of the

detector). Figure 5.9 shows a plot of the distribution of the z-coordinate of the event vertices.

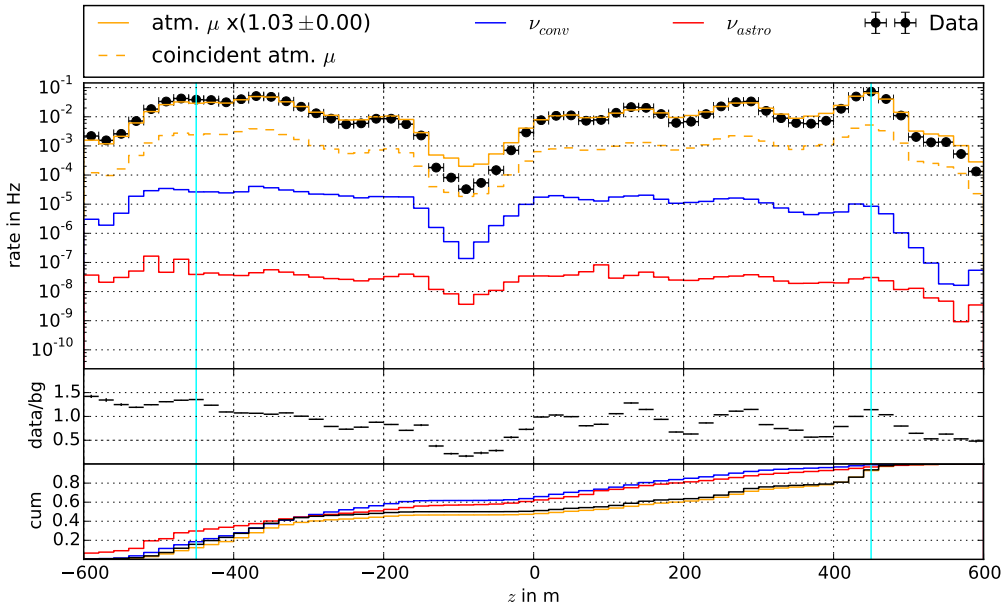

Figure 5.9: *The upper panel shows the distribution of the z coordinate of the event vertices reconstructed with CredoFit4 on Level 3 events. The center of the detector is $z = 0$ and the instrumented volume reaches from $z = -500$ m up to $z = 500$ m. The drop of the rate around a depth of $z \approx -100$ m is due to a dust layer consisting of volcanic ash. The red line shows the simulated astrophysical E^{-2} electron neutrino signal, the blue line is the sum of the conventional atmospheric muon and electron neutrinos, the orange line ("Corsika_5C") shows the atmospheric muons (simulated with the Five Component CORSIKA, see section 4.2.2) and the black data points represent 10% of the analyzed data sample. The dashed orange line ("CoincidentCorsika") shows the coincident atmospheric muons (see section 4.2.1). The vertical cyan lines indicate the applied cuts. The atmospheric (single) muon simulation is scaled with the factor (see equation 5.22 and its explainaing text) stated in the legend. The middle plot shows the ratio of the data and simulated background and the lower plot shows the cumulative distributions of the z coordinate.*

It can be seen that at this level, the measured data is dominated by the atmospheric muon background. This can be used to check the agreement of the distributions of the simulated muon background and the measured data. The overall rate agreement between them can be described by the ratio

$$f = \frac{\sum_{i=1}^{m} w_i^{data}}{\left(\sum_{j=1}^{n} w_j^{\mu} + \sum_{k=1}^{l} w_k^{atm.\nu}\right)}, \tag{5.22}$$

where w_i^{data} are the individual event weights of the 10% data sample, $w_k^{atm.\nu}$ the individual event weights of the simulated conventional atmospheric neutrino flux, and w_j^{μ} the ones for

the simulated atmospheric muon flux.[2] The ratio f and its error (rounded to two digits) are calculated and written behind the atmospheric muon simulation label in the legend of figure 5.9 and all following plots.
The variable distribution (in this case the z coordinate of the `Credo` reconstruction) of the Five Component CORSIKA muon simulation is scaled with the ratio f to the measured data. This allows for a better comparison of the simulated distribution with the measured data.

5.4.2 Layer of Maximum DOM Charge (LMDC)

The position of the DOM with the highest measured charge (number of photoelectrons) is used as an additional containment cut for the event selection. Events with the highest charge found on an edge DOM are complicated to interpret. They might indicate a neutrino interaction close to the detector boundary but they can also result from the catastrophic bremsstrahlung loss of a muon passing by the detector boundary. The IceCube detector strings can be separated into different layers. In the x-y-plane the outermost layer (see red dots in figure 5.8) which consists of the edge strings is layer 2, while the inner strings have smaller layer numbers. Due to the ambiguity associated with the highest charge percentage on the border, only events in which the highest number of photoelectrons DOM is one of the inner layers are retained ($LMDC_{xy} < 2$).
Along the z axis, layers are assigned according to the DOM position on the string, from 1 at the top to 60 at the bottom. A similar cut is applied on this axis: only events in which the highest number of photoelectrons was not recorded by one of the first three DOMs or the last three DOMs, i.e. $3 < LMDC_z < 58$ pass the event selection. Figure 5.10 shows the distribution of $LMDC_z$.

5.4.3 Layer of Earliest Hit (LEH)

Examining the temporal development of an event is an additional way to remove events which are possibly caused by muons moving into the detector volume from outside. The position of the DOM which has seen the first Cherenkov photons of the event is checked, and if it is found to lie on the boundary of the detector, the event is rejected. Using the same layer definitions as before, only events with $LEH_{xy} < 2$ are retained.
An analogous cut is used to reject muons which move in from the top of the detector. This is achieved by removing events which have their earliest hit in the in the top 50 m of the detector volume $LEH_z < 450$ m (see figure 5.12).

5.4.4 Number of Strings

The `Number of Strings` ($n_{strings}$) is a simple variable which defines how many of the IceCube strings have seen Cherenkov photons from the event. The more strings that see an

[2] The sums run over all events of each data set.

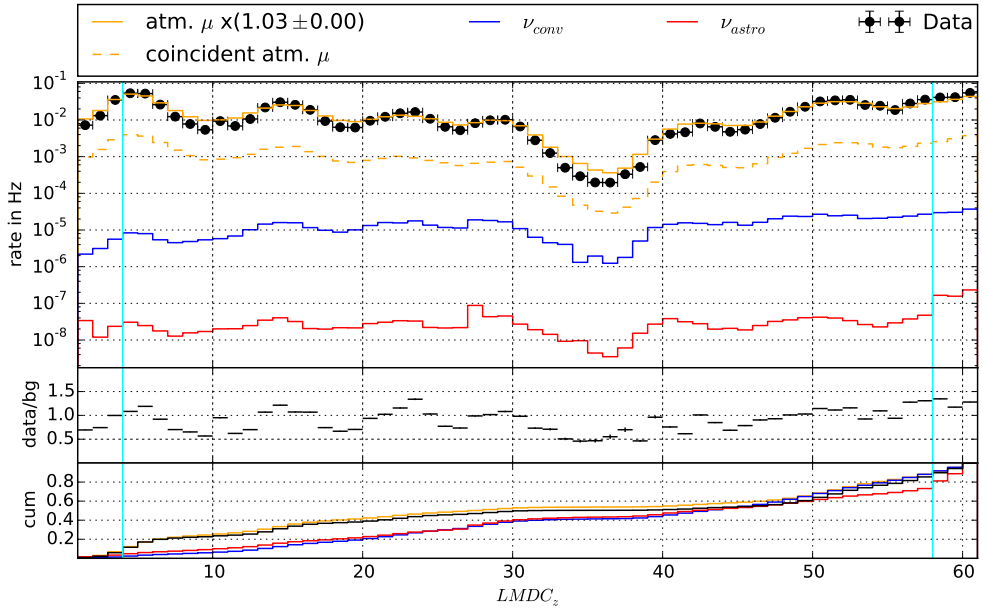

Figure 5.10: *The distribution the* `Layer of Maximum DOM Charge` *($LMDC_z$) in Level 3 events, depending on the DOM position. The number ranges from 1 (upper DOM) to 60 (lowest DOM) on an IceCube string. The line colors and panels are the same as in figure 5.9.*

event, the better its properties can be reconstructed. Figure 5.13 shows the distribution of the Number of Strings. Only events which are seen by DOMs on at least four strings pass this selection, $n_{strings} > 3$.

5.4.5 Energy reconstructed with Credo

A cut is placed on the event energy obtained from the `Credo` event reconstruction described in section 5.3.4. Figure 5.14 shows the distribution of the reconstructed `Credo` energies. Since the sample is completely background dominated at lower energies, finding an astrophysical neutrino flux contribution in this energy range is challenging. Due to the different energy spectra of astrophysical neutrinos and atmospheric muons (see section 2.2.3 and 2.3), a higher energy threshold removes more background than signal. The chosen energy threshold of the analysis $E_{Credo} > 10$ TeV, removes about 90% of atmospheric muon background events compared to Level 3 and results in a signal efficiency for electron neutrinos of about 60% (compared to Level 3).

5.4.6 Ratio between maximum and total charge

It can happen that muons undergo a catastrophic bremsstrahlung loss very close to a DOM. This DOM then measures a large amount of the event's total emitted Cherenkov light. These

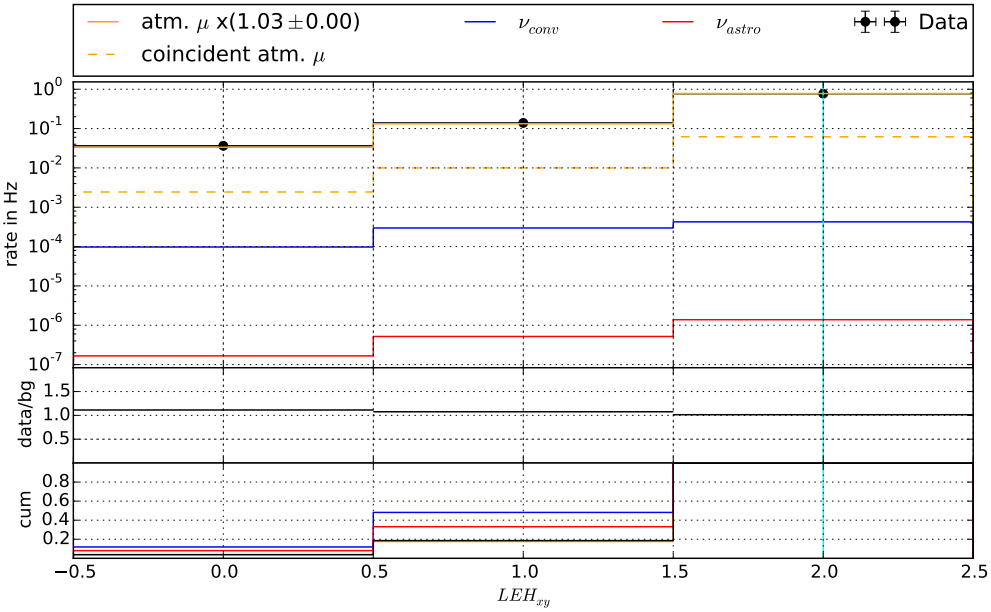

Figure 5.11: *The distribution of the* `Layer of Earliest Hit` *in the x-y-plane (LEH_{xy}) in Level 3 data. This shows the part of the detector which has seen the first Cherenkov photons of the event. The line colors and panels are the same as in figure 5.9.*

events are called balloon events (see [31]) and their energy can be overestimated, if they happen very close to a DOM. Furthermore, they cannot be distinguished from a neutrino interaction close to a DOM, if the track of the muon is too short or not visible. Due to this ambiguity balloon events are removed from the sample by cutting on the variable `Ratio between maximum and total charge`, which was already used in the IC22 analysis [91]. This is defined as the ratio of the highest charge measured by any DOM q_{max}^{DOM} divided by the sum of the charges of all DOMs q. Figure 5.15 shows the distribution of q_{max}^{DOM}/q. Balloon events are rejected by the application of the following cut: $q_{max}^{DOM}/q < 0.3$.

5.4.7 Energy to Charge Ratio

For electromagnetic cascades, the energy of a contained event is linearly correlated with the total charge of the event. Events that strongly deviate from this linear relation possibly indicate a problem with their energy reconstruction. The `Energy to Charge Ratio` is given by $\log((E_{Credo}/\text{GeV})/(q/\text{p.e.})) = \log(E_{Credo}/\text{GeV}) - \log(q/\text{p.e.})$, so the logarithm of the ratio of the `Credo` energy to the total charge of the event. Large values indicate an over-estimation of the event's energy. For this event selection, the cut $\log((E_{Credo}/\text{GeV})/(q/\text{p.e.})) < 1.9$ is applied. Figure 5.16 shows the distribution of the `Energy to Charge Ratio`.

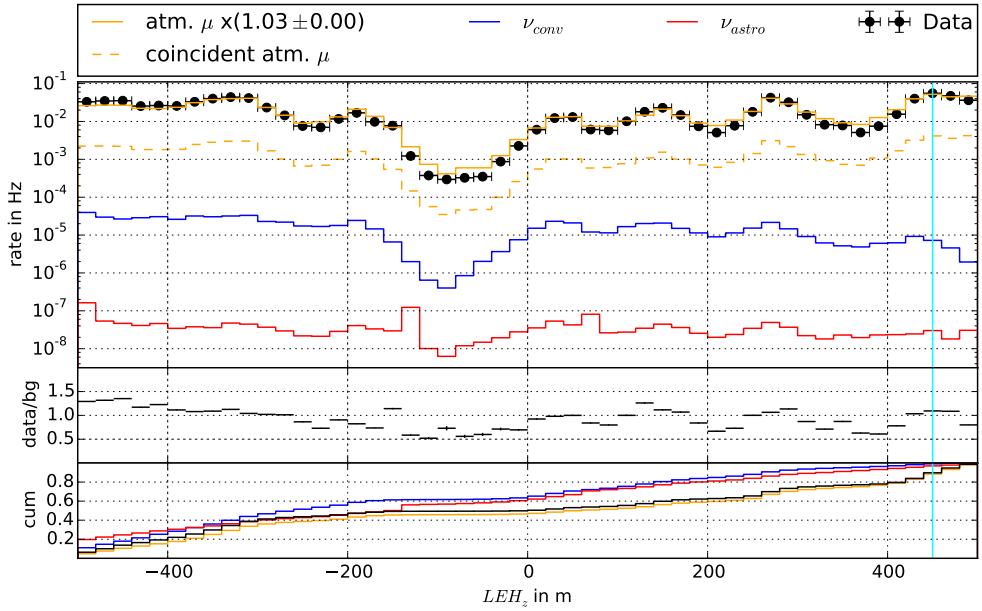

Figure 5.12: *The distribution of the z-coordinate of the* `Layer of Earliest Hit` *(LEH_z) in Level 3 data. The line colors and panels are the same as in figure 5.9.*

5.4.8 Level 4 Event Selection Summary

Level 4 Event Selection		
Containment Cuts	Quality Cuts	Energy Cut
$(x, y, z)_{event\ vertex} = contained$	$n_{strings} > 3$	$E_{Credo} > 10$ TeV
$LMDC_{xy} < 2$	$q_{max}^{DOM}/q < 0.3$	
$3 < LMDC_z < 58$	$\log((E_{Credo}/\text{GeV})/(q/\text{p.e.})) < 1.9$	
$LEH_{xy} < 2$		
$LEH_z < 450$ m		

Table 5.2: *The Level 4 event selection variables. To pass the Level 4 selection, the events must fulfill all cut criteria.*

Overall, the Level 4 event selection consists of the containment cuts, the quality cuts and the energy cut discussed, and which are outlined in table 5.2.[3] Table 5.3 shows the rates of simulated and data events for Level 3 and Level 4, the passing rates and the number of remaining events in the 10% sample (34 days).
The amount of data is reduced by the Level 4 event selection by a factor of about 8000 compared to Level 3, and results in about 365 events in the 10% sample. The rate of the

[3]To pass the Level 4 event selection, the events must fulfill all cut criteria, which are presented in table 5.2.

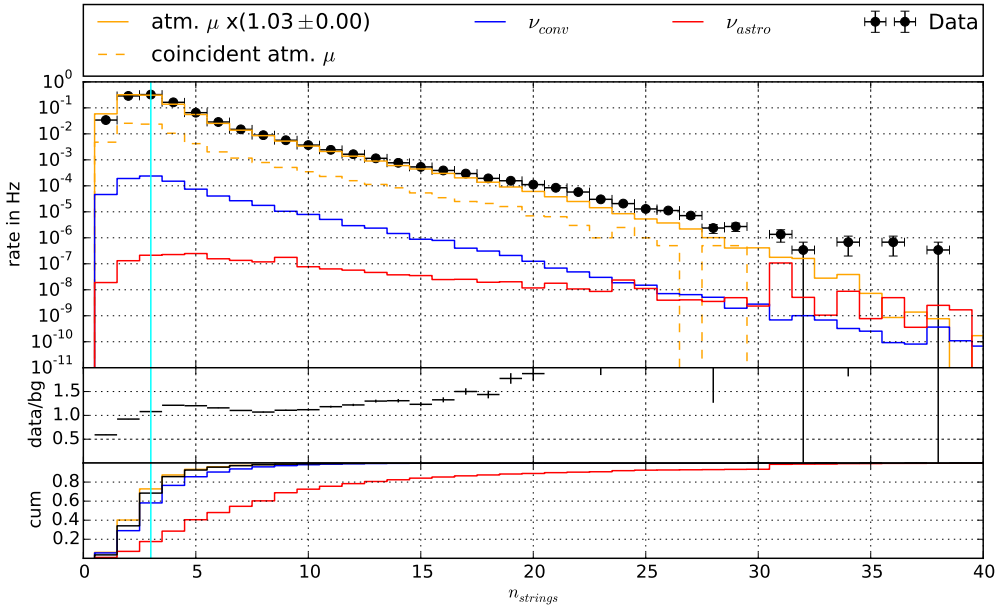

Figure 5.13: *The distribution of the* `Number of Strings` *($n_{strings}$) on Level 3 whose DOMs have detected the Cherenkov light of the event. Since the energy of the event is correlated with the $n_{strings}$ the distributions falls for increasing $n_{strings}$. The line colors and panels are the same as in figure 5.9.*

expected astrophysical neutrino flux is only reduced by a factor of about 9.[4] The number of expected astrophysical electron neutrinos is 0.7 in the 10% sample or 1.33 astrophysical neutrinos of all flavors, respectively. In order to reach the neutrino signal level the background has to be reduced additionally by a factor of about 300. To achieve that, the Level 5 event selection is used.

Level 4 Additional Reconstructions

After the Level 4 Event Selection, an additional `Credo` reconstruction was applied. Since the remaining sample was small enough, it was possible to run a computationally intensive eight-fold iterative `Credo` fit with the newly developed so-called SPICE ice model [85]. The higher number of iterations improves the event reconstruction, e.g. the energy resolution. The energy reconstruction of the `CredoFit8` is used for the final event selection in the following section.

[4] The rate of astrophysical electron neutrinos with energies $E > 10$ TeV, and vertices inside the polygon used for the vertex containment (see figure 5.8), is only reduced by a factor of about 2.5.

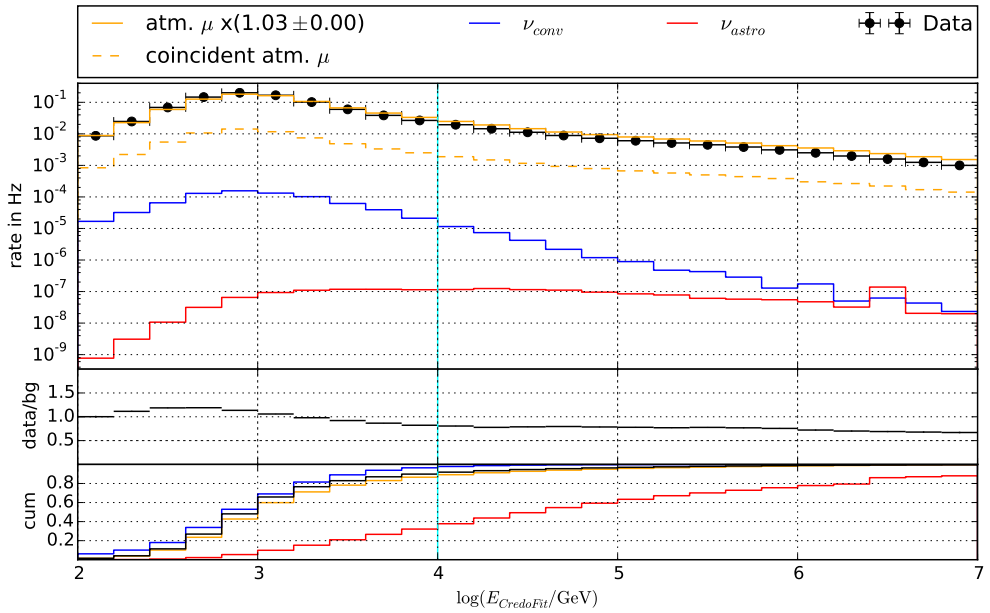

Figure 5.14: *The* `Credo` *energy reconstruction (E_{Credo}) on Level 3. The line colors and panels are the same as in figure 5.9. One can see that the about 60% of the ν_e signal events have energies higher than $\log(E_{Credo}/\mathrm{GeV}) = 4$ (10 TeV) while only about 10% of the background events are above this energy threshold.*

	Level 3 rate (Hz)	Level 4 rate (Hz)	ratio L4/L3	L4 events (10% sample)
$\mu^{coincident}_{atmospheric}$	$(7.40 \pm 0.02) \cdot 10^{-2}$	$(2.77 \pm 0.60) \cdot 10^{-5}$	$3.7 \cdot 10^{-4}$	$(8.16 \pm 1.77) \cdot 10^{1}$
$\mu_{atmospheric}$	$(9.20 \pm 0.01) \cdot 10^{-1}$	$(1.30 \pm 0.02) \cdot 10^{-4}$	$1.4 \cdot 10^{-4}$	$(3.83 \pm 0.05) \cdot 10^{2}$
Data	$(9.45 \pm 0.01) \cdot 10^{-1}$	$(1.24 \pm 0.06) \cdot 10^{-4}$	$1.3 \cdot 10^{-4}$	$(3.65 \pm 0.19) \cdot 10^{2}$
ν_e^{astro}	$(2.07 \pm 0.15) \cdot 10^{-6}$	$(2.41 \pm 0.01) \cdot 10^{-7}$	$1.2 \cdot 10^{-1}$	$(7.10 \pm 0.03) \cdot 10^{-1}$
ν_e^{conv}	$(1.33 \pm 0.01) \cdot 10^{-4}$	$(3.38 \pm 0.01) \cdot 10^{-7}$	$2.5 \cdot 10^{-3}$	$(9.90 \pm 0.01) \cdot 10^{-1}$
ν_μ^{conv}	$(6.87 \pm 0.09) \cdot 10^{-4}$	$(2.58 \pm 0.04) \cdot 10^{-6}$	$3.8 \cdot 10^{-3}$	(7.60 ± 0.12)

Table 5.3: *The rates of the Level 3 and Level 4 event selection. The simulated atmospheric muons are denoted as $\mu_{atmospheric}$ and the coincident ones with $\mu^{coincident}_{atmospheric}$. "Data" represents the measured data. ν_e^{astro} stands for the astrophysical electron neutrino signal, and ν_e^{conv} and ν_μ^{conv} denote the conventional atmospheric electron and muon neutrino flux [82].*

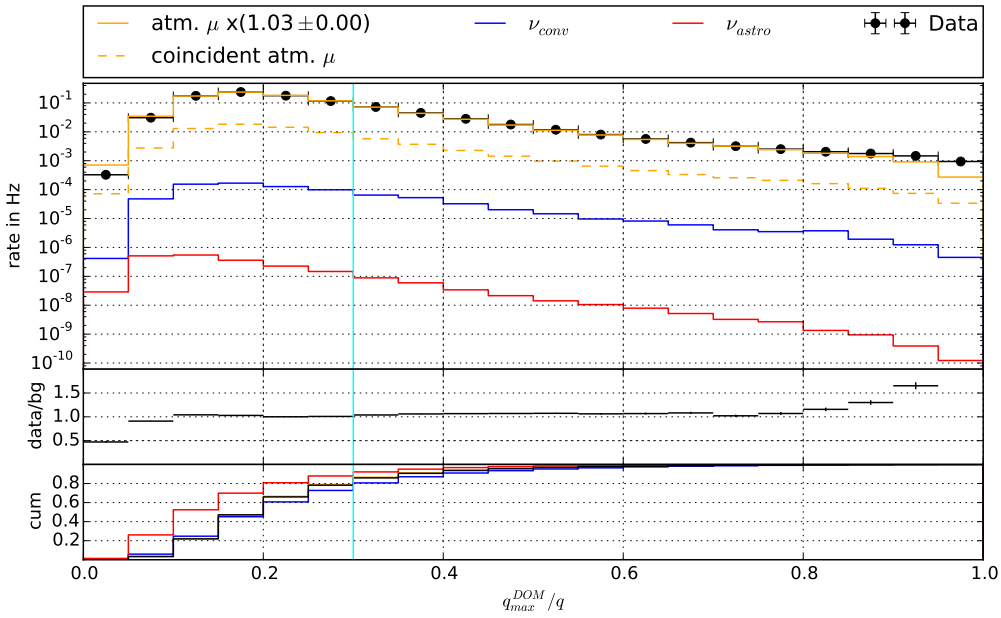

Figure 5.15: *The* `Ratio between maximum and total charge` *(q_{max}^{DOM}/q) in Level 3 data, which is used to veto an event class known as balloon events. The line colors and panels are the same as in figure 5.9.*

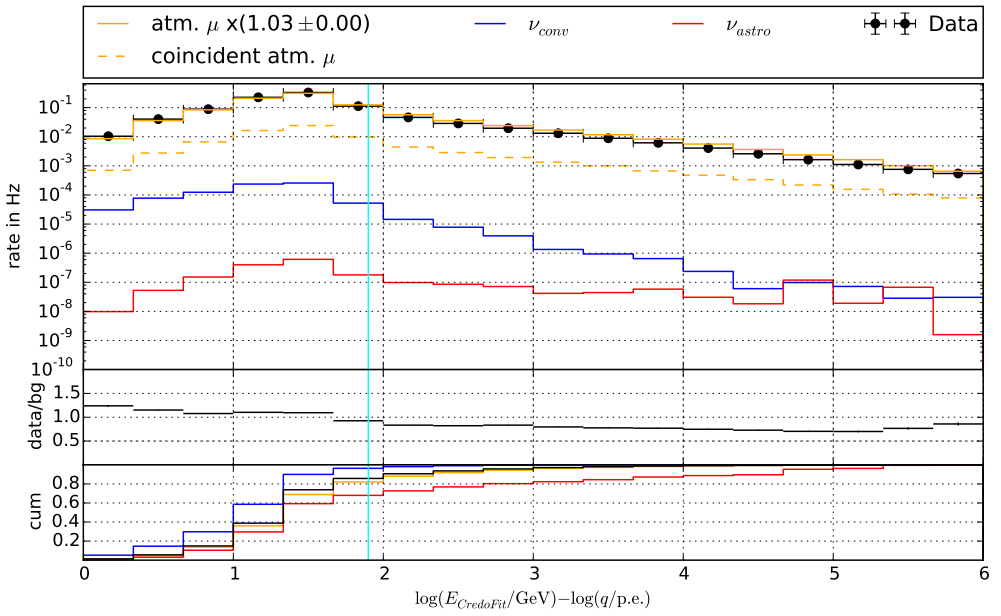

Figure 5.16: *The* `Energy to Charge Ratio` $\log((E_{Credo}/\mathrm{GeV})/(q/\mathrm{p.e.}))$ *in Level 3 data, which is used to reject events for which the* `Credo` *energy does not fit the deposited charge in the detector. The line colors and panels are the same as in figure 5.9.*

5.5 Level 5 - Final Event Selection

The aim of the final event selection, Level 5, is to reduce the number of simulated background events below the number of simulated astrophysical neutrino events.[5] To have confidence in the background estimate of the final event sample, a good agreement between the simulated background and the measured data is important on earlier levels of the event selection. An indication for a good agreement is that the ratio of the number of simulated events and of measured data events stays constant, within its statistical error margins, for the different cut variables in the last steps of the final event selection. Therefore, the figures of the Level 5 variable distributions are presented in sequence, with each subsequent distribution including all previously discussed cuts.
The variables used will be introduced in the following. They all select important properties of the cascade-like signal events and show a good background rejection power. The cut values were chosen to retain a 95% signal efficiency for each cut, while removing simulated background events as strongly as possible. The changes in the ratio of simulated to data events were carefully checked during the last steps of the event selection.

5.5.1 FillRatioRMS

This variable was already introduced in section 5.3.5. Figure 5.17 shows its distribution after Level 4. In Level 5, a cut of $FillRatioRMS > 0.67$ is applied, which preserves 95% of the neutrino signal efficiency while removing about 80% of the simulated background.

5.5.2 First Photon Arrival Time

The `First Photon Arrival Time` is a causality variable taking into account the earliest possible arrival time of Cherenkov photons at a DOM given a cascade-like event hypothesis. Figure 5.18 shows a sketch of a possible scenario: a muon producing a high energy cascade by emitting a hard bremsstrahlung photon along its track, faking a neutrino interaction event. The Cherenkov light of the cascade propagates with the speed of light c_{vac}/n_{ice} through the ice. The muon travels with $v \approx c_{vac}$ through the detector and can produce additional hits on DOMs. For a given cascade vertex estimate (x, y, z, t) taken from `CredoFit` of the assumed cascade-like event, these Cherenkov photons from the muon would appear to be superluminal. The `First Photon Arrival Time` Δt_{early} is calculated according to

$$\Delta t_{early} = \min_i \left(t_i^{earliest\ hit} - \frac{d_i}{c_{ice}} \right), \tag{5.23}$$

where i runs over all DOMs, $t_i^{earliest\ hit}$ is the time of the earliest hit of DOM i, c_{ice} is the

[5] In section 5.6 a cut and count analysis based on the Level 5 event selection and an addtional energy cut, optimized to obtain the smallest possible average upper limit for the astrophysical neutrino flux, is introduced. Using the Level 5 event selection and a different energy cut, a likelihood fit is applied to the data in section 6.

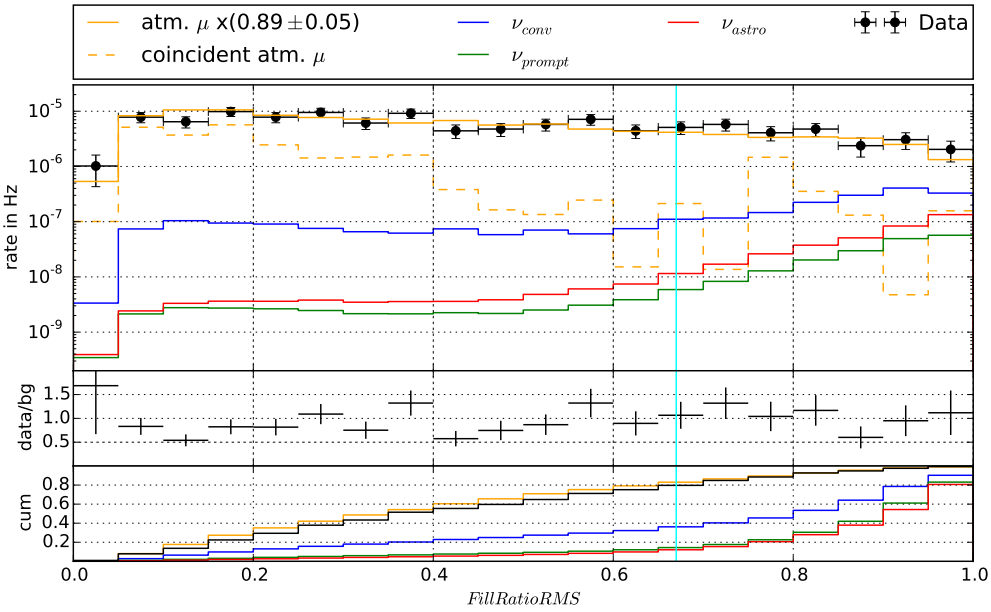

Figure 5.17: *The* `FillRatioRMS` *distributions in Level 4 data. Cascade-like events have a more spherical profile and therefore they have larger values of FillRatioRMS than the muon track event patterns from the atmospheric muons. The red line shows the sum of the simulated astrophysical E^{-2} neutrino fluxes (ν_e, ν_μ, ν_τ). The green line is the sum of the simulated prompt atmospheric neutrino fluxes. The other line colors and panels are the same as in figure 5.9.*

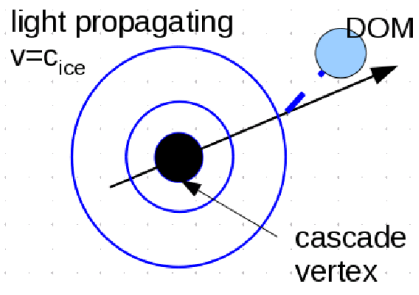

Figure 5.18: *This is a sketch of a muon undergoing a catastrophic bremsstrahlung-loss and later emitting Cherenkov radiation arriving the detector too early for a cascade hypothesis.*

speed of light in ice and d_i is the distance between the ith DOM and the cascade vertex. After the first cut of $\Delta t_{early} > -200$ ns (with 95% signal efficiency) it still showed a strong discrimination power between signal and background. Therefore, a second cut of $\Delta t_{early} > -78.5$ ns was applied, leading to a total signal efficiency after the two cuts of 90% while reducing the background by more than 85%.

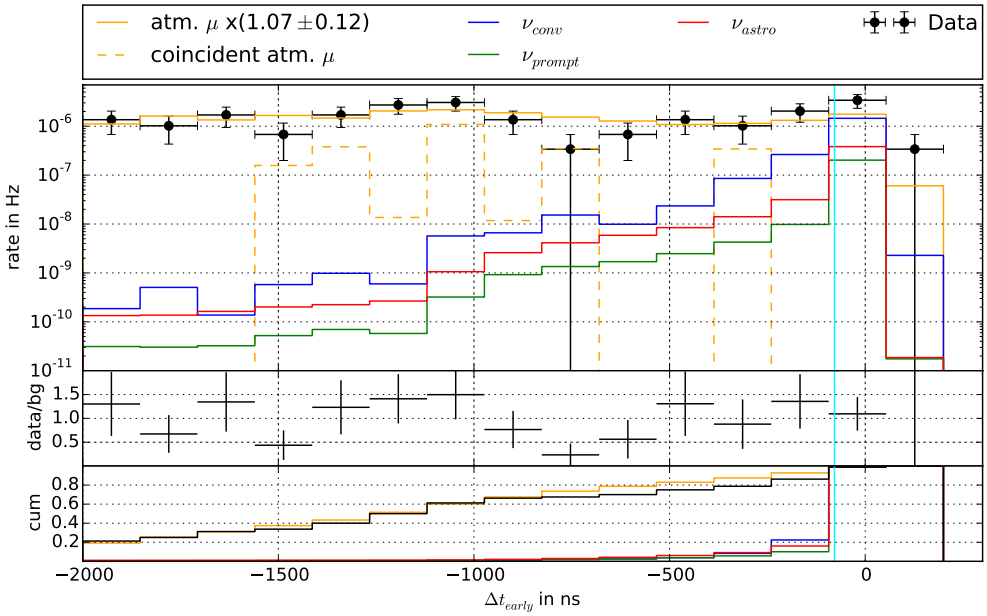

Figure 5.19: *The* `First Photon Arrival Time` *(Δt_{early}) distributions with the previously discussed Level 5 cuts already applied. Events created by a neutrino interaction have residual photon arrival times close to zero. Events created by muons can have large negative residual photon arrival times. The line colors and panels are the same as in figure 5.17.*

5.5.3 Cascade Vertex Likelihood Fit Quality

The next cut was applied on the quality parameter *rlogL* of the `Cascade Vertex Likelihood Fit`, already described in section 5.3.1. Figure 5.20 shows its distribution for signal, and background simulation and data. The condition $rlogL < -7.45$ was chosen for this cut, retaining 95% of the signal while reducing the atmospheric muon background by 60%.

5.5.4 Final Energy Distribution

After the the application of all cuts, described in section 5.5.1 through 5.5.3 a final energy distribution is obtained, as shown in figure 5.21.

The appearance of events with energies smaller than 10 TeV in figure 5.21 is not in contradiction to the Level 4 event selection (see section 5.4.8), which consists of an energy cut of $E_{Credo} > 10$ TeV. The `Credo` reconstruction in the Level 3 processing [119] used an older ice model AHA [98]. For the Level 4 `Credo` event reconstruction, the new SPICE ice model [85] was used (see section 5.4.8).
One can see from the final energy distribution, that there are no simulated atmospheric muon events left for energies $\log(E_{CredoFit8}/\text{GeV}) > 4.5$ ($E > 32$ TeV).
To estimate the number of simulated atmospheric muons for higher energies, their distri-

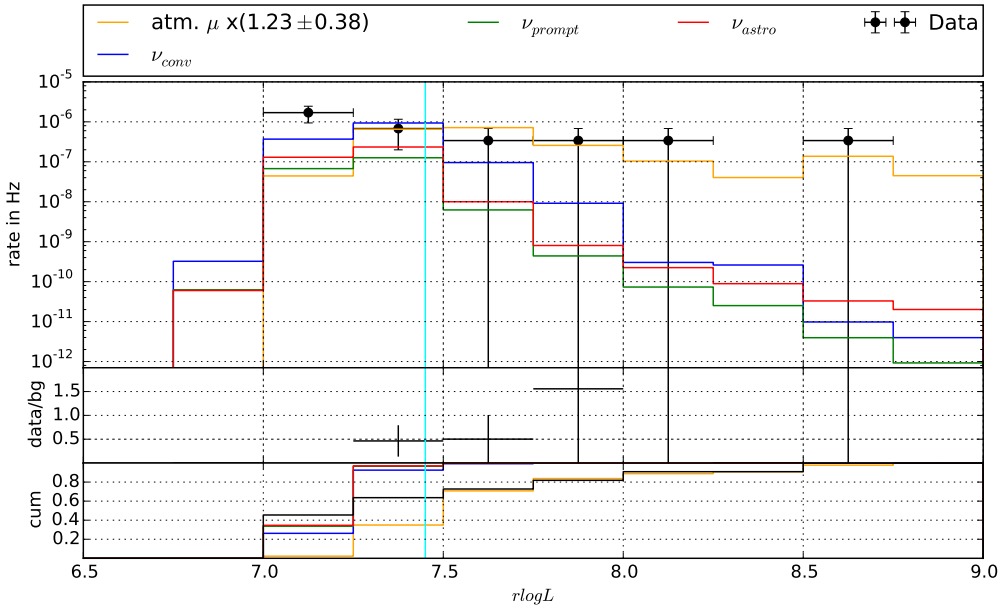

Figure 5.20: *The* `Cascade Vertex Likelihood Fit Quality` *(rlogL) distributions with the previously discussed Level 5 cuts already applied. Cascade-like events have smaller values of* `Cascade Vertex Likelihood Fit Quality`*. The line colors and panels are the same as in figure 5.17.*

bution for 10 TeV $\leq E \leq$ 32 TeV was fit with a power-law ($dN/dE = \Phi_0 \cdot E^{-3.7}$) with the normalization Φ_0 as a free fit parameter. The atmospheric muon spectrum is one power steeper than the primary cosmic ray spectrum for energies $E_\mu \gg 1$ TeV [34], hence the power-law index in the fit was approximated with −3.7. This power law was integrated from $E = 32$ TeV to infinity

$$R_\mu = \int_{32\,\mathrm{TeV}}^{\infty} \Phi_0 \cdot E^{-3.7} dE = (2.26 \pm 0.85) 10^{-8}\,\mathrm{s}^{-1} \tag{5.24}$$

to obtain the extrapolated number of remaining atmospheric muon events for $E \geq 32$ TeV.

5.5.5 Energy resolution and bias removal

Figure 5.22 shows the energy resolution of the experiment for astrophysical electron neutrinos (E^{-2}) for the final event selection. The x-axis is the difference between the `CredoFit8` energy reconstruction and the cascade energy E_{vis}. E_{vis} is the energy of an electromagnetic cascade, that produces the observed amount of Cherenkov light in the detector.
The peak of the energy resolution was fit with a Gaussian function, from which a mean μ and a width σ are obtained. σ can be interpreted as the energy resolution: $\Delta \log(E) =$

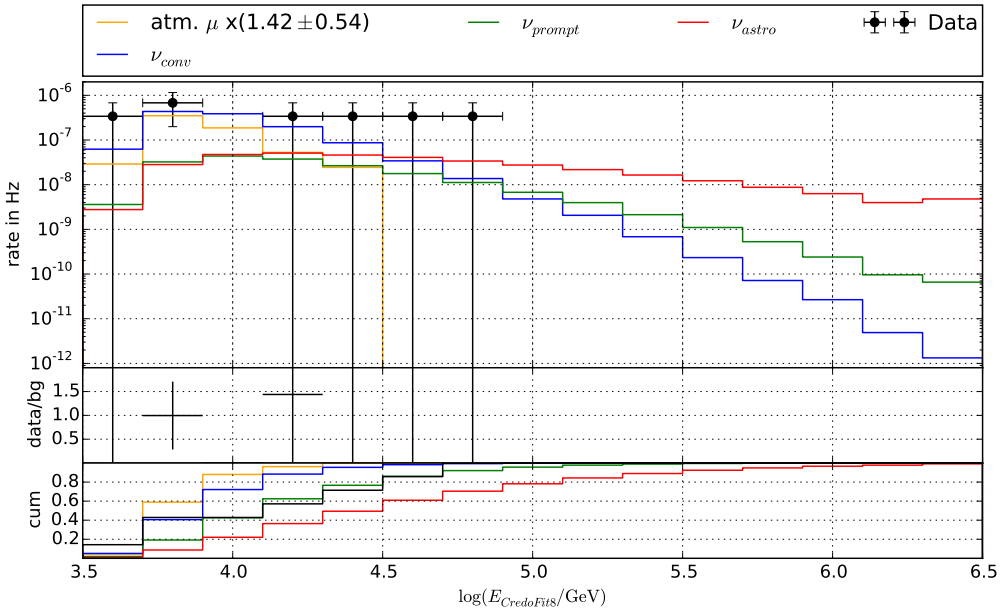

Figure 5.21: *The final* Credo *energy distribution after the application of all the Level 5 event selection criteria. All simulated atmospheric muon events can be removed by an energy cut of* $\log(E_{Credo}/\mathrm{GeV}) > 4.5$. *The line colors and panels are the same as in figure 5.17.*

$\log E_{Credo} - \log E_{vis} = 0.05$, which is equivalent to an energy resolution of $\Delta E/E \approx 12\%$. μ can be understood as the bias or systematic energy shift between the reconstructed energy and E_{vis}. With $\mu = -0.08$, the reconstructed energy is a underestimated by about 17%. The energy bias can be removed by adding 0.08 to all reconstructed energies (in $\log(E)$) or similarly, by multiplying all reconstructed energies by a factor of 1.20. This global energy scale correction was applied to all reconstructed energies for the data as well as for the simulation, and all reconstructed energies quoted from now on contain this correction factor.

5.5.6 Average upper limit

The influence of a final energy cut on the average upper limit of the diffuse astrophysical neutrino flux was studied. The concept of the average upper limit will be introduced briefly in the next paragraph.
The following short introduction to the concept of the average upper limit is based on [78]. In case of a non-detection of an expected flux, the experimental results can be used to derive a limit on that flux. Let Φ be the expected flux, and n_s and n_b the number of expected signal events and background events, respectively. When the experiment is performed, a number of events, n_{obs}, is observed. A confidence interval for the limit is chosen, in this case the 90% confidence interval $\mu_{90} = [\mu_1, \mu_2]$, which is a function of the number of expected background events n_b and the number of observed events n_{obs}. For 90% of the experiments

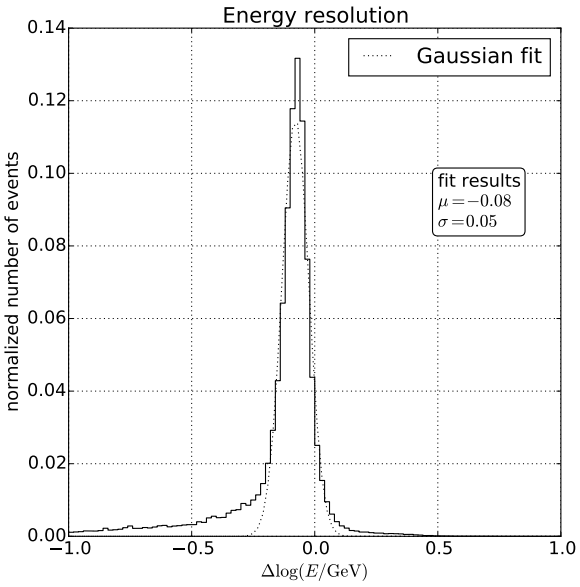

Figure 5.22: *The energy resolution for the simulated astrophysical electron neutrino flux for the Level 5 event selection.*

the interval μ_{90} includes the true value of μ. To give an example, an experiment observing 3 events with an expected background of 1.5 events results in a 90% confidence interval in the Feldman-Cousins approach [57] of $\mu_{90}(3, 1.5) = [0.0, 5.92]$. $\mu_2 = 5.92$ is the upper limit. In the following μ_{90} means this upper limit.
The upper limit on the flux Φ is then calculated according to

$$\overline{\Phi}_{90\%} = \Phi \cdot \frac{\mu_{90}\left(n_{obs}, n_b\right)}{n_s(\Phi)}. \tag{5.25}$$

The number of signal events $n_s(\Phi)$ is determined by the number of simulated astrophysical neutrinos according to the flux Φ. The higher the number of signal events is compared to $\mu_{90}\left(n_{obs}, n_b\right)$, the stronger the flux can be constrained. Therefore the event selection should be optimized in a way that the ratio $\mu_{90}\left(n_{obs}, n_b\right)/n_s(\Phi)$ becomes small. A problem is that the upper limit still depends on the number of observed events n_{obs}, which is unknown at the point of the event selection optimization. Assuming no signal, the upper limit can be generalized to an average upper limit, by marginalizing over all possible observed event numbers n_{obs} weighted by their Poisson probability of occurrence

$$\overline{\mu}_{90}\left(n_b\right) = \sum_{n_{obs}=0}^{\infty} \mu_{90}\left(n_{obs}, n_b\right) \frac{n_b^{n_{obs}}}{n_{obs}!} \exp(-n_b). \tag{5.26}$$

The resulting average upper limit $\overline{\mu}_{90}\left(n_b\right)$, which only depends on the number of expected

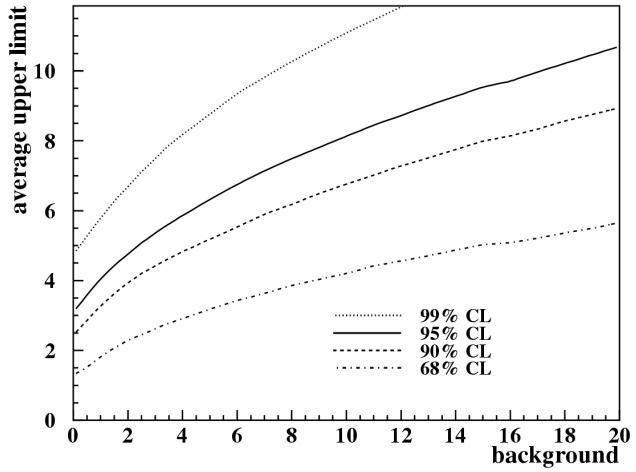

Figure 5.23: *Average upper limit $\overline{\mu}_{90}(n_b)$ as a function of the number of expected background events for different Poisson confidence levels. The plot was taken from [78].*

background events, is shown in figure 5.23 for different confidence levels. When the experiment is actually performed, the obtained limit will be different from $\overline{\Phi}_{90\%}$ since it depends on how the background fluctuates in the real experiment. The average upper limit tells what is to be expected on average if the real experiment is repeated infinite times.
Figure 5.24 shows how the average upper limit of the astrophysical neutrino flux depends on the final energy cut. One can see a minimum in the average upper limit at about $\log(E/\mathrm{GeV}) = 4.5$.

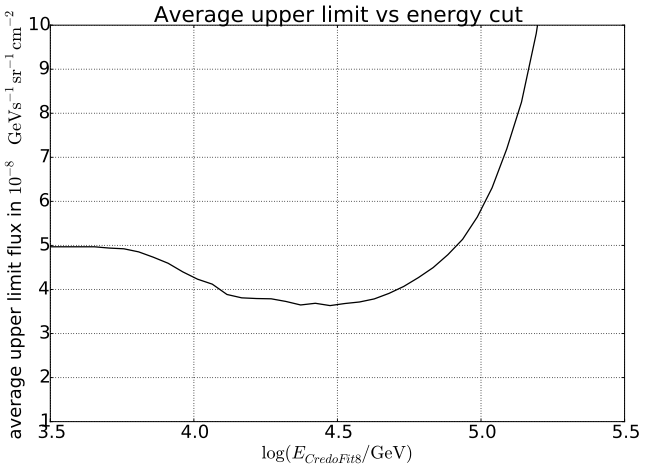

Figure 5.24: *The average upper limit of the astrophysical neutrino flux as a function of the final energy cut.*

5.5.7 Effective Area

The effective area $A_{eff}(E)$ is a geometrical measure of the detector efficiency at different energies E. With this one can obtain the expected differential event number dN/dE in the detector for a differential flux $d\Phi/dE$

$$\frac{dN}{dE}(E) = 4\pi \cdot \frac{d\Phi}{dE}(E) \cdot A_{eff}(E) \cdot t_{live} \tag{5.27}$$

with the data taking time of the detector t_{live} and the detector's solid angle of 4π.
The effective area can be calculated by

$$A_{eff}(E) = 2\pi r^2 \cdot \frac{N_{sel}(E)}{N_{sim}(E)} \tag{5.28}$$

wherein $N_{sel}(E)$ is the number of simulated events with energy E after the final event selection and $N_{sim}(E)$ is the number of events originally simulated in the radius r around the detector. Figure 5.25 shows a comparison of the effective areas with the event selection from section 5.6 and the sample "Ib" [5] of the previous cascade analysis with IceCube in its 40 string configuration (IC40). The effective area of IC59 is larger than the one of IC40, since the detector size of IC59 is about 50% larger than the one of IC40.

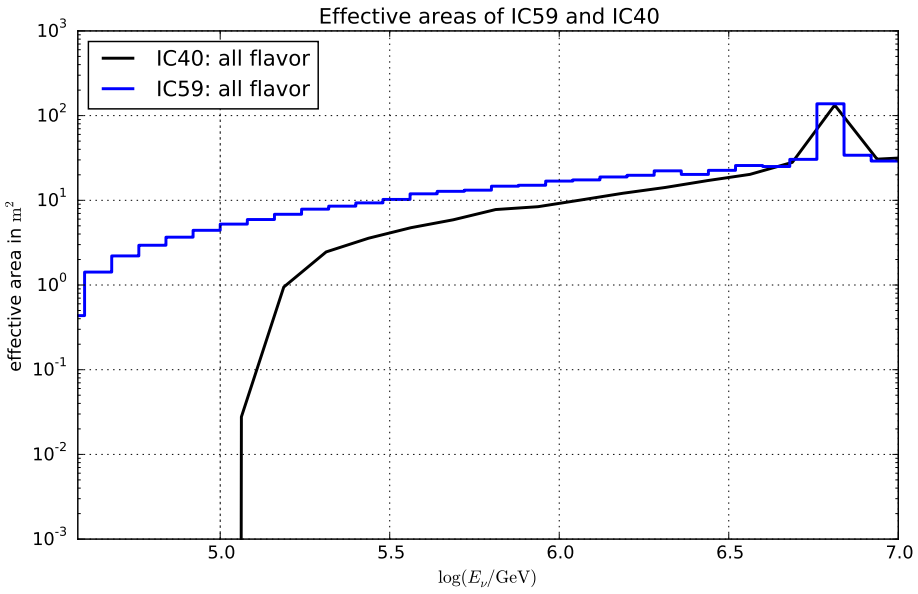

Figure 5.25: *The effective areas for the cut and count event selection (see section 5.6) in blue and the IC40 analysis in black. The peak at $E \approx 6.3$ PeV is the Glashow resonance (see [70]). The data points of the IC40 analysis are taken from [102].*

5.6 Cut and count analysis

As a first approach to analyze the data set, a cut and count analysis was performed. An additional energy cut was applied to the Level 5 event selection, to obtain a sample with the smallest possible number of background events. Therefore, the energy threshold of the analysis was chosen to be $\log(E/\mathrm{GeV} \geq 4.58$ ($E \geq 38$ TeV). Furthermore, this energy cut corresponds to the minimum region of the average upper limit (see section 5.5.6). For this event selection, table 5.4 shows the number of simulated events and data events (10% data sample).

	L4 rate (Hz)	L5 rate (Hz)	ratio L5/L4	L5 events (10% sample)
ν_e^{astro}	$(2.41 \pm 0.01) \cdot 10^{-7}$	$(9.77 \pm 0.05) \cdot 10^{-8}$	$4.1 \cdot 10^{-1}$	$(2.88 \pm 0.01) \cdot 10^{-1}$
ν_μ^{astro}	$(1.03 \pm 0.01) \cdot 10^{-7}$	$(1.89 \pm 0.03) \cdot 10^{-8}$	$1.8 \cdot 10^{-1}$	$(5.57 \pm 0.09) \cdot 10^{-2}$
ν_τ^{astro}	$(1.84 \pm 0.01) \cdot 10^{-7}$	$(6.30 \pm 0.05) \cdot 10^{-8}$	$3.4 \cdot 10^{-1}$	$(1.85 \pm 0.02) \cdot 10^{-1}$
ν_e^{conv}	$(3.38 \pm 0.01) \cdot 10^{-7}$	$(1.46 \pm 0.01) \cdot 10^{-8}$	$4.3 \cdot 10^{-2}$	$(4.29 \pm 0.02) \cdot 10^{-2}$
ν_μ^{conv}	$(2.58 \pm 0.04) \cdot 10^{-6}$	$(4.12 \pm 0.16) \cdot 10^{-8}$	$1.5 \cdot 10^{-2}$	$(1.21 \pm 0.05) \cdot 10^{-1}$
$(\nu_e + \nu_\mu)^{conv}$	$(2.92 \pm 0.04) \cdot 10^{-6}$	$(5.58 \pm 0.16) \cdot 10^{-8}$	$1.9 \cdot 10^{-2}$	$(1.64 \pm 0.05) \cdot 10^{-1}$
ν_e^{prompt}	$(1.94 \pm 0.01) \cdot 10^{-7}$	$(3.75 \pm 0.01) \cdot 10^{-8}$	$1.9 \cdot 10^{-1}$	$(1.10 \pm 0.03) \cdot 10^{-1}$
ν_μ^{prompt}	$(6.58 \pm 0.05) \cdot 10^{-8}$	$(5.02 \pm 0.10) \cdot 10^{-9}$	$7.6 \cdot 10^{-2}$	$(1.48 \pm 0.03) \cdot 10^{-2}$
ν_τ^{prompt}	$(7.91 \pm 0.04) \cdot 10^{-9}$	$(1.36 \pm 0.01) \cdot 10^{-9}$	$1.7 \cdot 10^{-1}$	$(4.01 \pm 0.04) \cdot 10^{-3}$
$(\nu_e + \nu_\mu + \nu_\tau)^{prompt}$	$(2.68 \pm 0.01) \cdot 10^{-7}$	$(4.38 \pm 0.01) \cdot 10^{-8}$	$1.6 \cdot 10^{-1}$	$(1.29 \pm 0.01) \cdot 10^{-1}$
$\mu_{atmospheric}$	$(1.30 \pm 0.02) \cdot 10^{-4}$	$(2.26 \pm 0.85) \cdot 10^{-8}$	$1.7 \cdot 10^{-4}$	$(6.65 \pm 2.50) \cdot 10^{-2}$
$\mu_{atmospheric}^{coincident}$	$(2.77 \pm 0.60) \cdot 10^{-5}$	no statistics	no statistics	no statistics
signal	$(5.28 \pm 0.01) \cdot 10^{-7}$	$(1.80 \pm 0.01) \cdot 10^{-7}$	$3.4 \cdot 10^{-1}$	$(5.29 \pm 0.02) \cdot 10^{-1}$
total background	$(1.61 \pm 0.06) \cdot 10^{-4}$	$(1.22 \pm 0.09) \cdot 10^{-7}$	$7.6 \cdot 10^{-4}$	$(3.60 \pm 0.25) \cdot 10^{-1}$
10% data sample	$(1.24 \pm 0.06) \cdot 10^{-4}$	$(6.79 \pm 4.80) \cdot 10^{-7}$	$5.5 \cdot 10^{-3}$	2 ± 1.4

Table 5.4: *The rates of the Level 4 and Level 5 event selection. The simulated atmospheric muons are denoted as $\mu_{atmospheric}$ and the coincident ones with $\mu_{atmospheric}^{coincident}$. "10% data sample" represents the 10% sample of the measured data. ν_e^{astro}, ν_μ^{astro} or ν_τ^{astro} stand for the astrophysical electron, muon or tau neutrino signal each with a spectrum $dN/dE \cdot E^2 = 1.0 \cdot 10^{-8}\,\mathrm{GeV\,s^{-1}\,sr^{-1}\,cm^{-2}}$. "signal" is the sum of the three neutrino flavors. ν_e^{conv} and ν_μ^{conv} denote the conventional atmospheric electron and muon neutrino flux [82]. ν_e^{prompt}, ν_μ^{prompt} and ν_τ^{prompt} represent the prompt components of the atmospheric neutrino flux [55]. The "total background" is the sum of conventional and prompt atmospheric neutrino fluxes and the atmospheric muons and the coincident atmospheric muons.*

Non of the simulated coincident atmospheric muon events survived the Level 5 event selection. The application of only two cuts of the Level 5 event selection already removed all remaining coincident muons. Furthermore, the rate of the coincident atmospheric muons was about a factor of 10 lower than the rate of the (single) atmospheric muons.
Two data events in the 10% data sample with energies of 67 TeV and 52 TeV survive the final event selection. Expecting 0.36 events of total background in the 10% sample, one can calculate the probability to see two or more data events just due to a statistical upward

fluctuation of the background

$$P(\lambda = 0.36, k \geq 2) = \sum_{k=2}^{k=\infty} \frac{\lambda^k}{k!} \exp(-\lambda) = 1 - \exp(-\lambda) - \lambda \exp(-\lambda) = 0.05. \quad (5.29)$$

Therefore in 5% of the cases, the number of background events (0.36) can fluctuate statistically to two or more events.

5.6.1 Full data sample

Based on the presented event selection (see section 5.6), the IceCube collaboration gave its permission to study the complete IC59 data sample. Six additional events were found in the 90% data sample, which gives a total of 8 data events passing all the selection criteria. The total number of predicted background events from simulation is $N_{back} = 3.5 \pm 0.3$, for the livetime of 335 days of the IC59 data sample. So, there is a small excess in the data above the expected background.

Table 5.5 gives an overview of the properties of the found events and Figure 5.26 shows their energy spectrum. Figure 5.27 shows the x and y position of the found events compared to the vertex containment cut which was applied in the Level 4 event selection. The figures 5.28 - 5.35 show the 8 event displays each with its vertex coordinates and its energy.

event	sample	E/TeV	x/m	y/m	z/m	q/pe
1	10%	67	266	325	-397	5152
2	10%	52	-227	213	321	1404
3	90%	42	452	32	369	1108
4	90%	39	200	240	-259	2510
5	90%	61	123	8	43	2552
6	90%	43	442	192	400	567
7	90%	48	422	125	213	1948
8	90%	39	126	-98	61	3643

Table 5.5: *Event parameters in the 10% and 90% data samples: Columns are the energy in TeV, event coordinates x, y and z in meters, and the sum of the charge over all DOMs in number of photoelectrons (pe).*

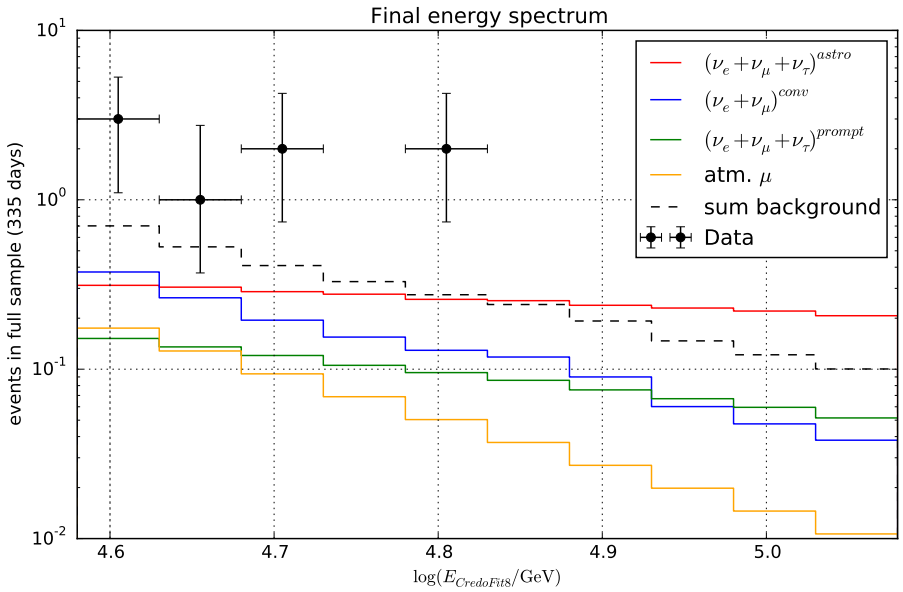

Figure 5.26: *The energy spectrum of the 8 data events found in the full IC59 sample. The error bars on the data are the 68 % Feldman-Cousins intervals [57]. The simulated atmospheric muon background is shown in orange and is obtained by the extrapolation described in equation 5.24. The simulated conventional and prompt atmospheric neutrino fluxes according to [82] and [55] are shown in blue and green, respectively. The red line shows the sum of the simulated astrophysical E^{-2} electron, muon and tau neutrino spectra (1:1:1). The total background consisting of the conventional and prompt atmospheric neutrinos, and the atmospheric muons is shown by the black dashed line.*

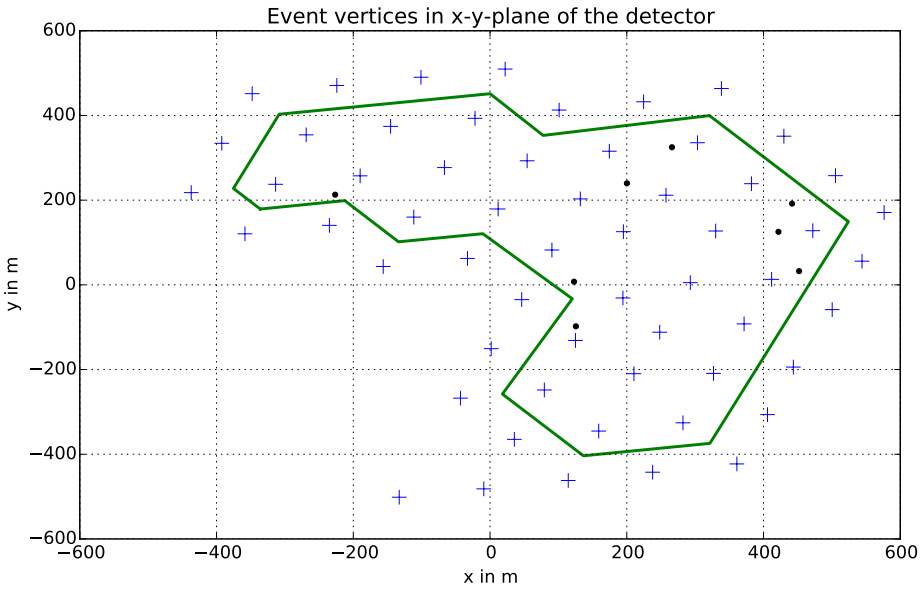

Figure 5.27: *The x and y positions (black dots) of the reconstructed vertices of the 8 data events found in the IC59 sample. The blue crosses (+) mark the string positions and the green line marks the vertex containment cut, which was applied in the Level 4 event selection.*

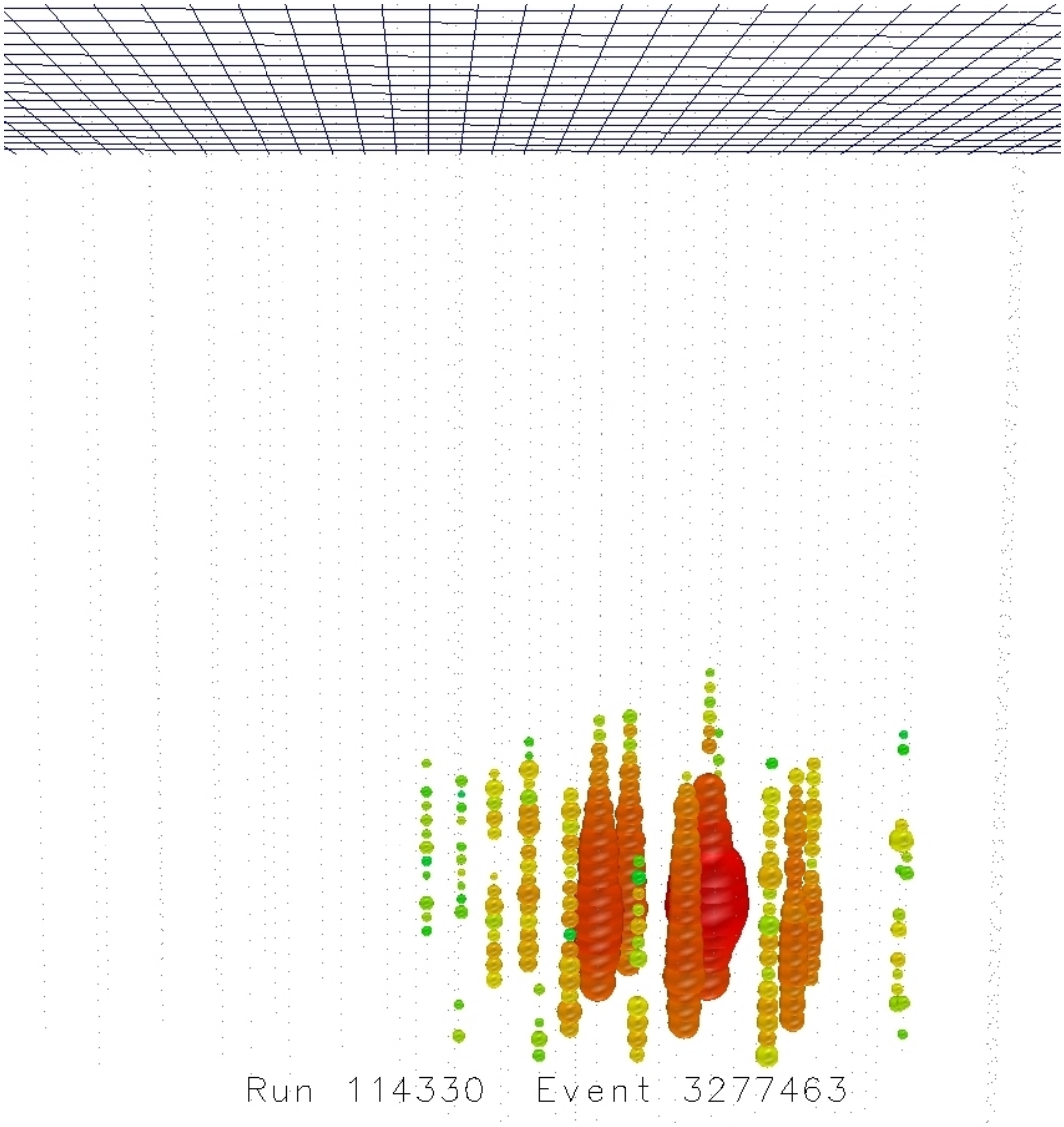

Figure 5.28: *The figure shows the first event with an energy of* $E = 67$ TeV *and vertex coordinates* $(x, y, z) = (266, 325, -397)$ m.

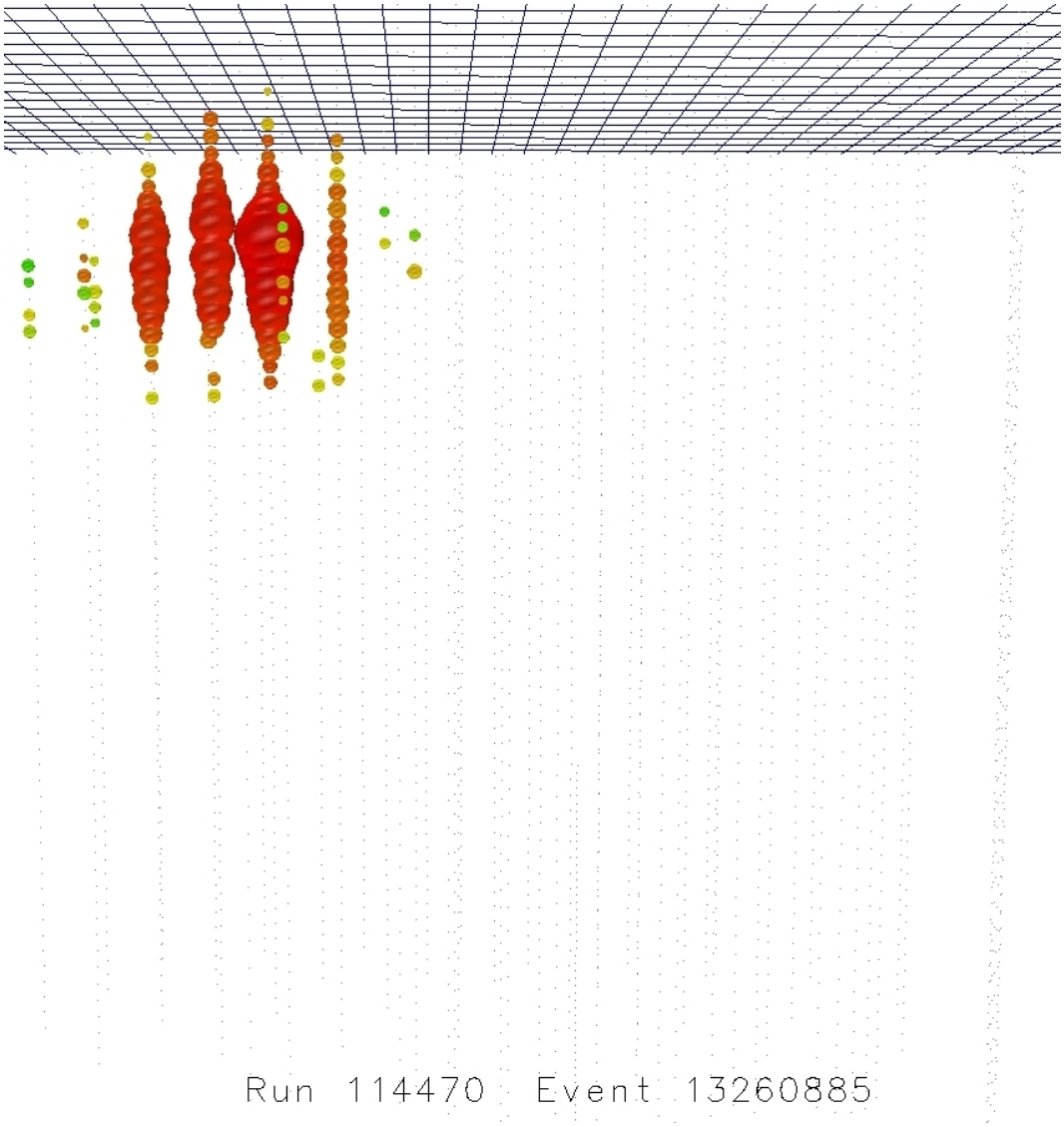

Figure 5.29: *The figure shows the second event with an energy of* $E = 52$ TeV *and vertex coordinates* $(x, y, z) = (-227, 213, 321)$ m.

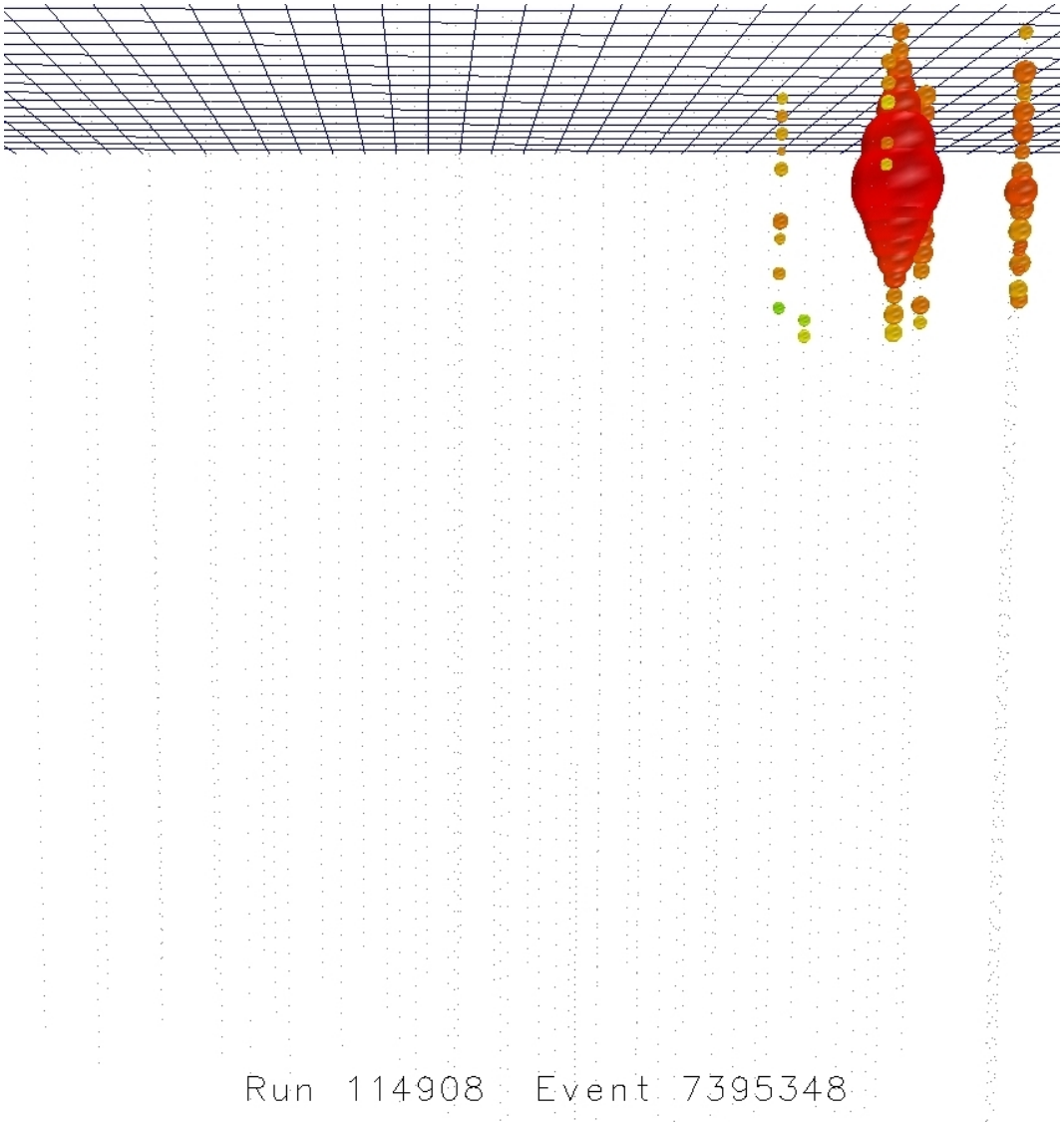

Figure 5.30: *The figure shows the third event with an energy of* $E = 42$ TeV *and vertex coordinates* $(x, y, z) = (452, 32, 369)$ m.

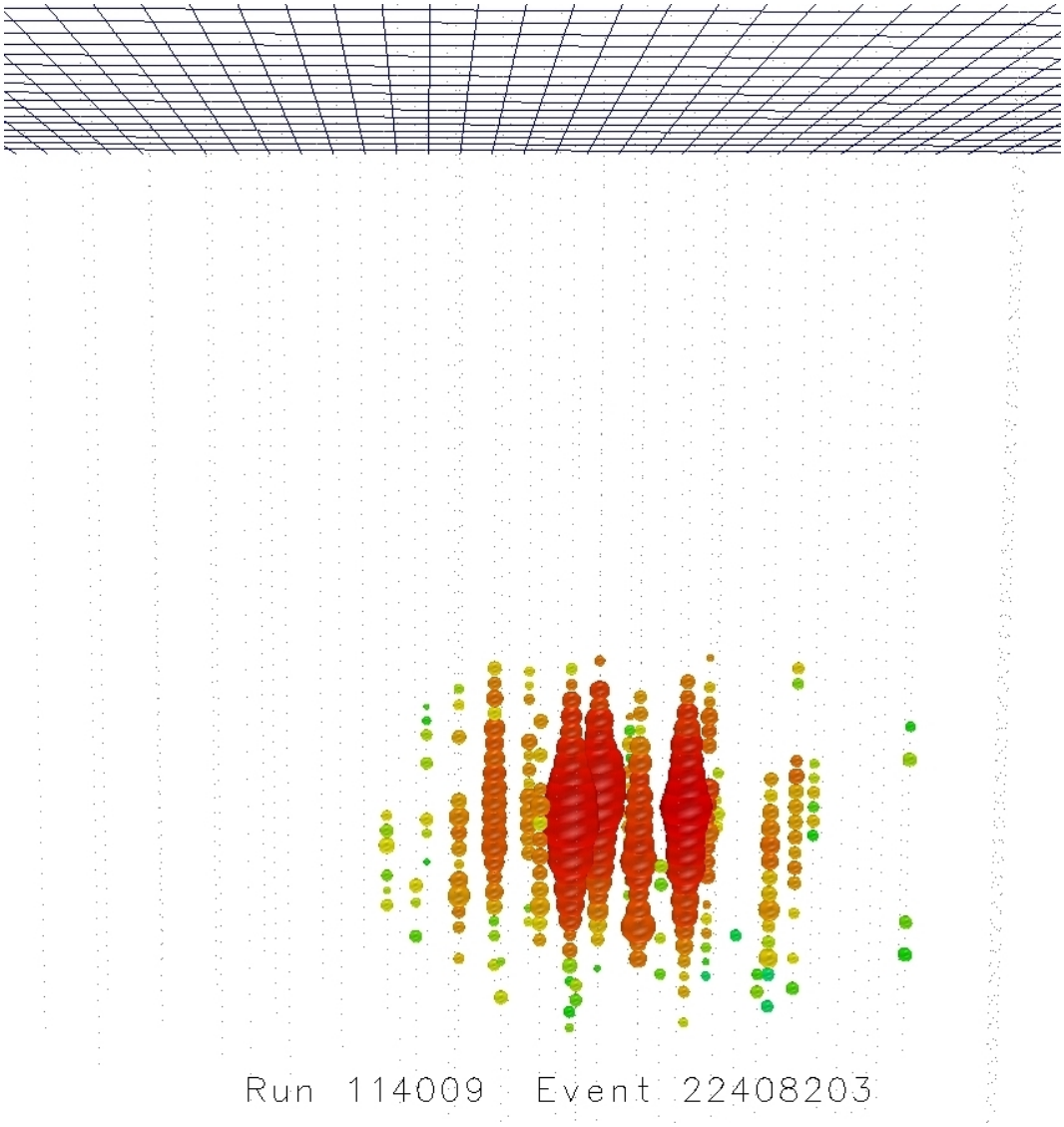

Figure 5.31: *The figure shows the fourth event with an energy of* $E = 39$ TeV *and vertex coordinates* $(x, y, z) = (200, 240, -259)$ m.

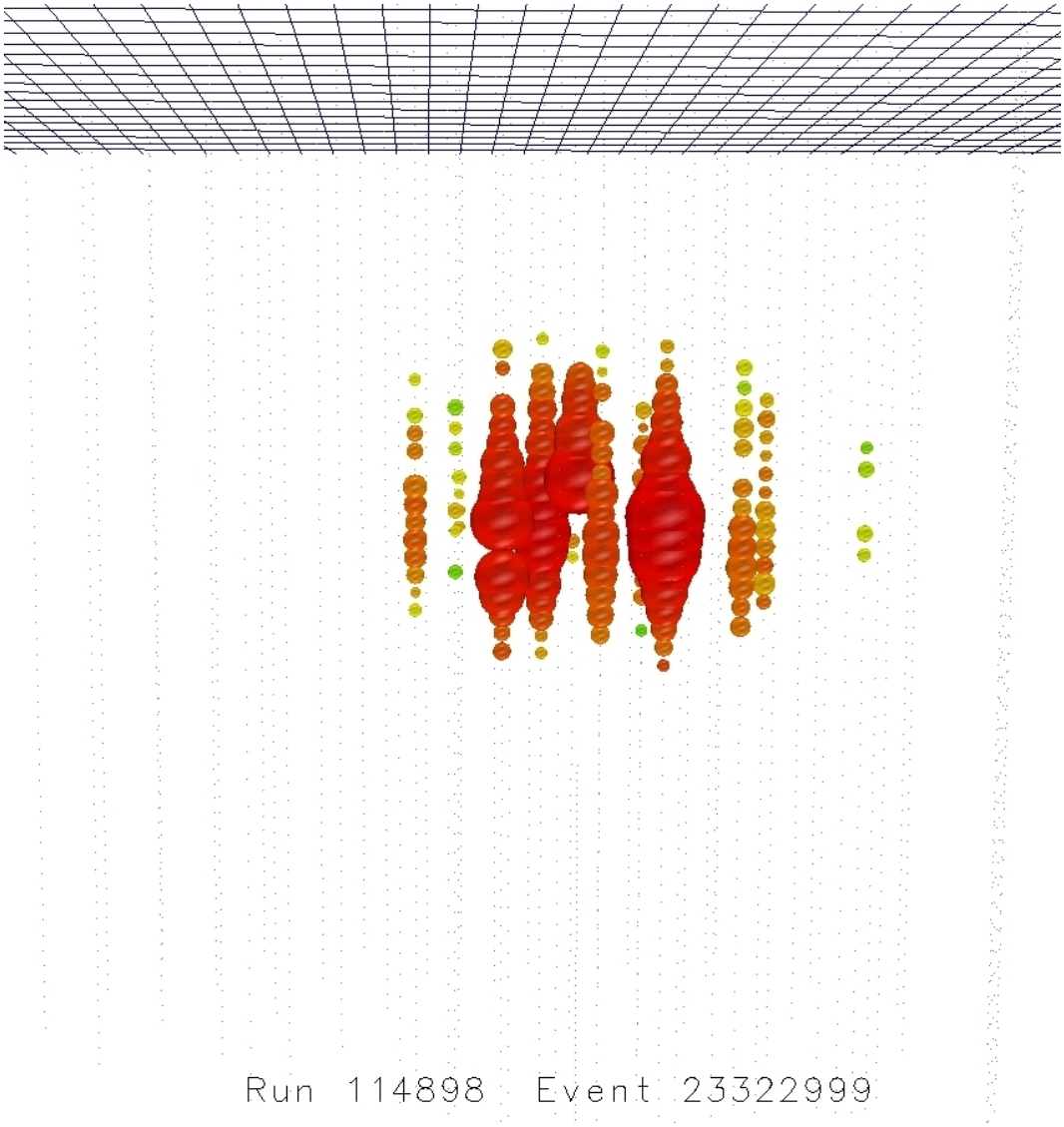

Figure 5.32: *The figure shows the fifth event with an energy of* $E = 61$ TeV *and vertex coordinates* $(x, y, z) = (123, 8, 43)$ m.

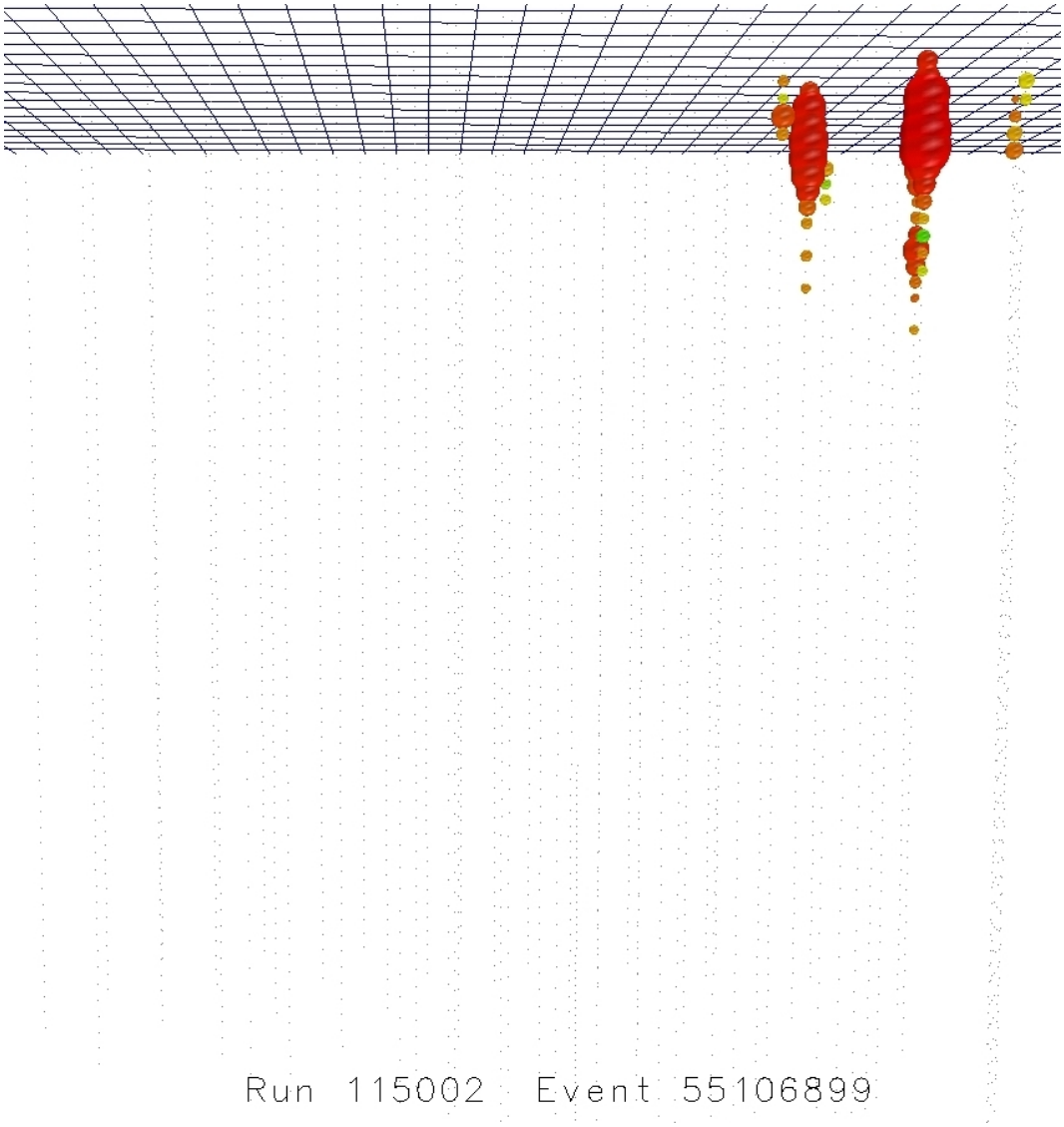

Figure 5.33: *The figure shows the sixth event with an energy of* $E = 43$ TeV *and vertex coordinates* $(x, y, z) = (442, 192, 400)$ m.

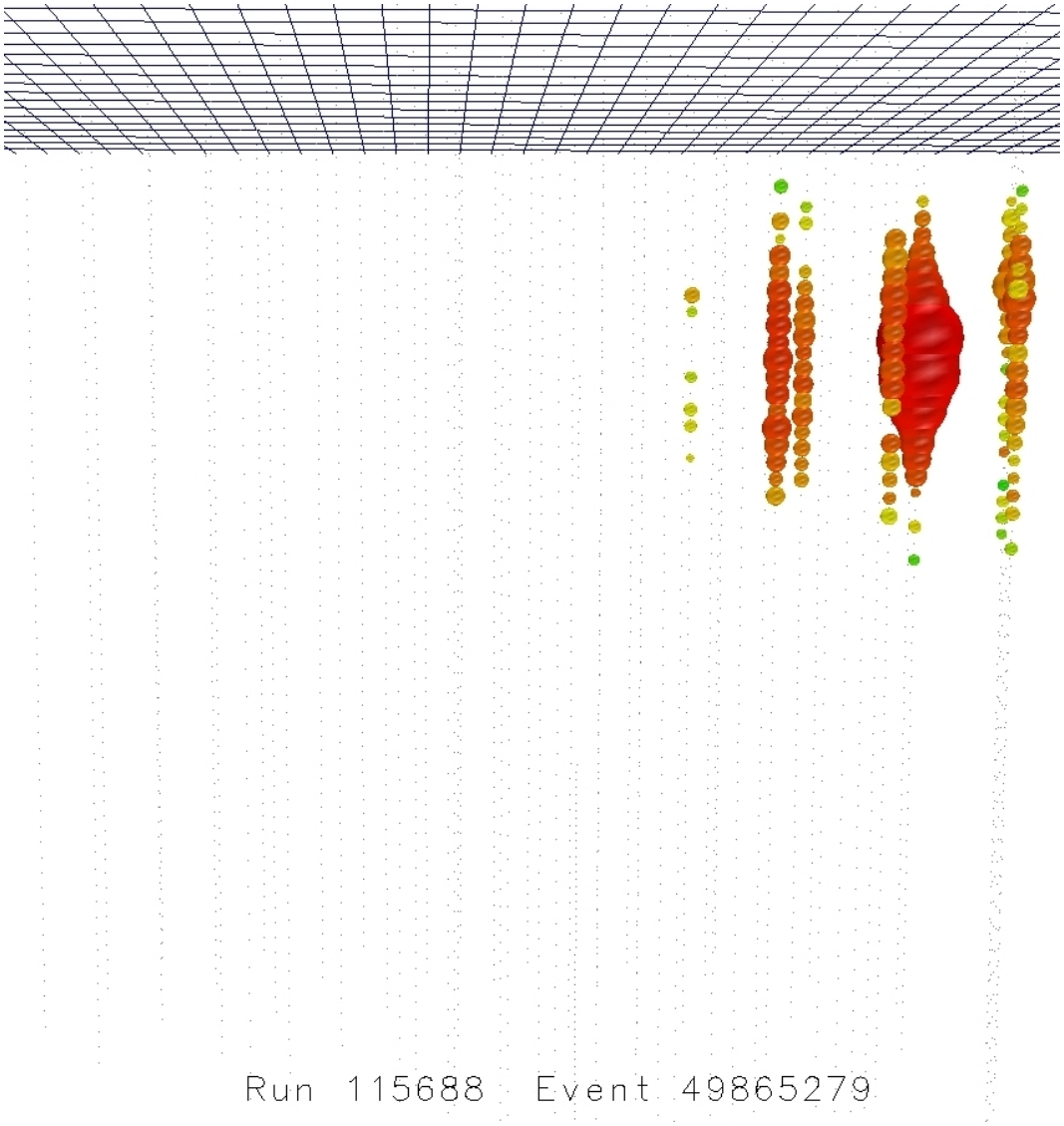

Figure 5.34: *The figure shows the seventh event with an energy of* $E = 48$ TeV *and vertex coordinates* $(x, y, z) = (422, 125, 213)$ m.

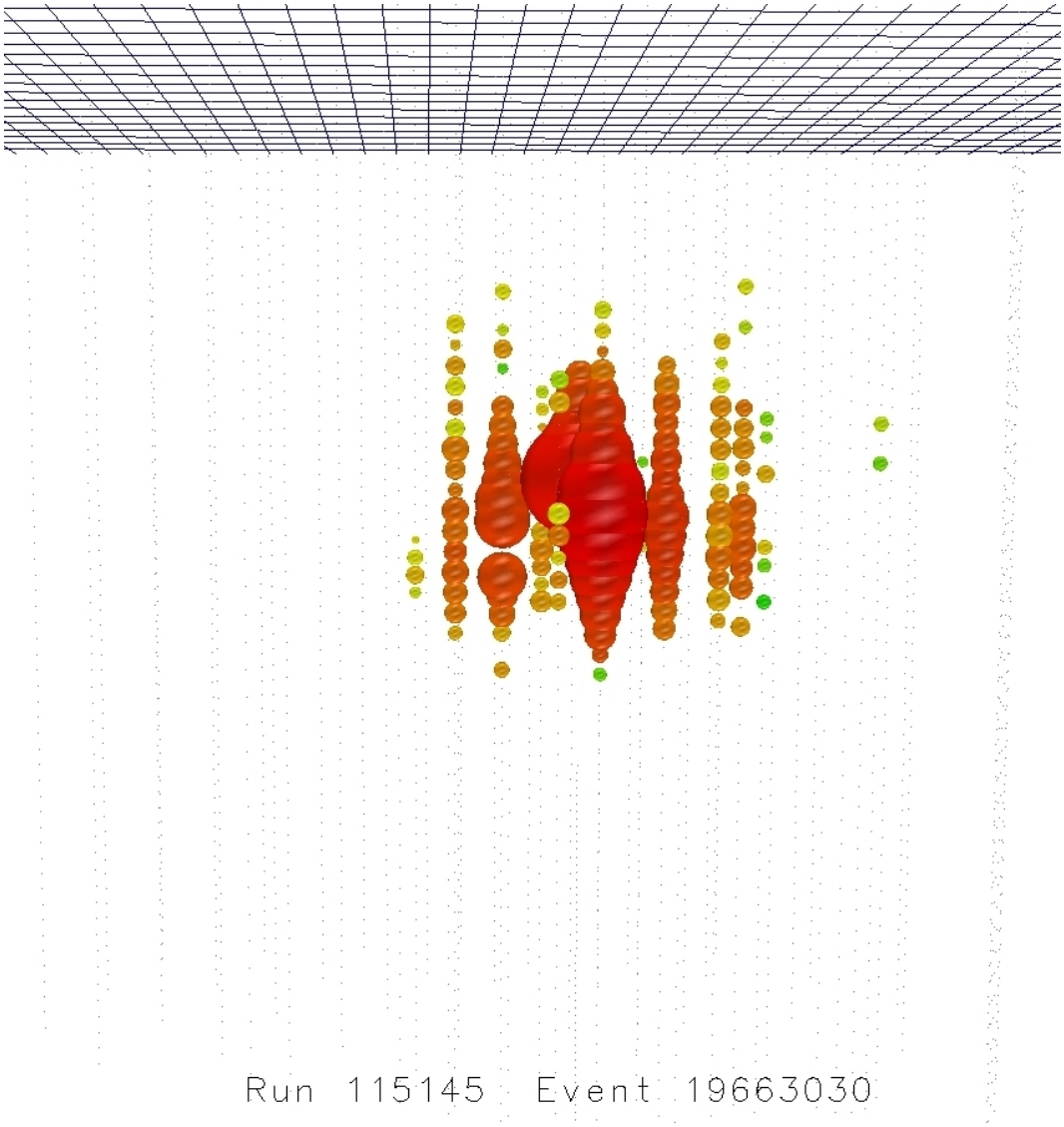

Figure 5.35: *The figure shows the eighth event with an energy of* $E = 39$ TeV *and vertex coordinates* $(x, y, z) = (126, -98, 61)$ m.

6 Likelihood Fit

A likelihood fit is applied to the energy distribution of the observed events to extract as much as possible information of the measured data. A likelihood fit is able to account for the different shapes of the energy spectra for the signal and the various background components. Therefore, it is more sensitive than a simple cut and count approach(see section 5.6).
The issue is to determine how the observed data events are best described. There are a number of components that can be used to model the data: the atmospheric muon flux, the conventional and prompt atmospheric neutrino flux and the diffuse astrophysical neutrino flux. The likelihood fit determines the contribution of each of these components to the observed data sample. If no astrophysical neutrino flux is required to reproduce the data, a limit on this flux can be obtained.
The maximum-likelihood fitting technique is described in general in the next section, followed by a discussion of the likelihood fit and the different hypotheses applied to this data.

6.1 Likelihood Method

This brief introduction to likelihood fits and hypothesis tests follows the review from the Particle Data Book [111]. Let's assume we have a measurement of N values $\boldsymbol{x} = (x_1, ..., x_N)$ which can be described by a probability density function (p.d.f.) $f(\boldsymbol{x};\boldsymbol{\theta})$ in which $\boldsymbol{\theta} = (\theta_1, ..., \theta_n)$ is a set of n unknown parameters. One then calls $L(\boldsymbol{\theta}) = f(\boldsymbol{x};\boldsymbol{\theta})$ the likelihood function, which is evaluated based on the data $\boldsymbol{x}$ and then only depends on the parameters $\boldsymbol{\theta}$. In the case that the x_i are statistically independent of each other, and each one can be described by the p.d.f. $f(x_i;\boldsymbol{\theta})$, then the likelihood function can be written as a product of these single factors

$$L(\boldsymbol{\theta}) = \prod_{i=1}^{N} f(x_i;\boldsymbol{\theta}). \tag{6.1}$$

With the maximum likelihood method one searches the estimates $\hat{\boldsymbol{\theta}}$ of $\boldsymbol{\theta}$ for the one, which maximizes the likelihood $L(\boldsymbol{\theta})$.
In general, it is numerically easier to work with $\ln L(\boldsymbol{\theta})$ instead of $L(\boldsymbol{\theta})$, since both are maximized by the same estimators $\hat{\boldsymbol{\theta}}$. These estimators can be found by searching for the maximum of the likelihood function

$$\frac{\partial \ln L(\boldsymbol{\theta})}{\partial \theta_i} = 0, \quad i = 1, ..., n. \tag{6.2}$$

In high dimensional phase spaces, these equations can often only be solved numerically. One often uses the negative logarithm of the likelihood ($-\ln L(\boldsymbol{\theta})$) and then seeks its minimum using minimization codes. In general, the maximum likelihood minimization provides unbiased estimators and also works efficiently on huge data samples.
For a set of maximum likelihood estimators, their covariance maxtrix $V_{ij} = cov[\hat{\theta}_i, \hat{\theta}_j]$ can be obtained by the calculation of the inverse matrix V^{-1} which is defined by

$$(\hat{V}^{-1})_{ij} = - \left. \frac{\partial^2 \ln L(\boldsymbol{\theta})}{\partial\theta_i \partial\theta_j} \right|_{\hat{\boldsymbol{\theta}}}. \tag{6.3}$$

In the large sample limit, the likelihood $L(\theta)$ has a Gaussian form. Then the error contour $\boldsymbol{\theta'}$ of the estimator $\hat{\boldsymbol{\theta}}$ can be calculated based on

$$-\ln L(\boldsymbol{\theta'}) = -\ln L(\hat{\boldsymbol{\theta}}) + s^2/2, \tag{6.4}$$

in which $(-\ln L(\hat{\boldsymbol{\theta}}))$ is the minimum of the likelihood at the value $\boldsymbol{\theta} = \hat{\boldsymbol{\theta}}$ and s is the number of standard deviations (σ). The interval $[\theta_i^{lower}, \theta_i^{upper}]$ that solves equation 6.4 is then a good approximate s-standard-deviation confidence interval for θ_i.
If one has a large sample of data, one can bin the data in a histogram resulting in a vector of data $\boldsymbol{n} = (n_1, ..., n_N)$. One can minimize the likelihood function $-\ln L(\boldsymbol{\theta})$ based on the bin entries. Assuming independent Poisson-distributed n_i, this leads to a p.d.f. for the number of observed counts n_i in bin i

$$f(n_i, \nu_i(\boldsymbol{\theta})) = \frac{\nu_i(\boldsymbol{\theta})^{n_i}}{n_i!} \exp(-\nu_i), \tag{6.5}$$

where ν_i is the expected number of counts given by $\boldsymbol{\theta}$. Alternatively, one can also maximize the likelihood ratio given by $\lambda(\boldsymbol{\theta}) = f(\boldsymbol{n}; \boldsymbol{\nu}(\boldsymbol{\theta}))/f(\boldsymbol{n}; \boldsymbol{n})$. This is equivalent to minimizing the follwing expression

$$\begin{aligned} -2\ln\lambda(\boldsymbol{\theta}) &= -2\ln\left(\prod_{i=1}^{N} \frac{f(n_i, \nu_i(\boldsymbol{\theta}))}{f(n_i, n_i)}\right) = -2\ln\left(\prod_{i=1}^{N} \frac{\nu_i(\boldsymbol{\theta})^{n_i}}{n_i^{n_i}} \exp(n_i - \nu_i(\boldsymbol{\theta}))\right) \\ &= 2\sum_{i=1}^{N}\left(\nu_i(\boldsymbol{\theta}) - n_i + n_i \ln\frac{n_i}{\nu_i(\boldsymbol{\theta})}\right), \end{aligned} \tag{6.6}$$

in which the last term becomes zero for $n_i = 0$.
A goodness-of-fit test can be applied to the data. For large enough $\nu_i(\boldsymbol{\theta})$, and if some further regularity conditions are fulfilled, one can apply Wilks' theorem [[131]] which states that the minimum of the likelihood ratio $-2\ln\lambda(\boldsymbol{\theta})$ (see equation 6.6) follows a χ^2 distribution. For N bins and m fitted parameters, the χ^2 distribution has $N - m$ degrees of freedom.

In likelihood fit applications, one sometimes has additional parameters $\boldsymbol{\alpha}$ which can only be determined by the data but which are not relevant for the fit result. These nuisance parameters appear then also in the likelihood $L(\boldsymbol{\theta}, \boldsymbol{\alpha})$. Since the nuisance parameters are unknown, the minimization of $-\ln L(\boldsymbol{\theta}, \boldsymbol{\alpha})$ depends on them. However, this can be solved by effectively removing the nuisance parameters by the construction of the profile likelihood given by

$$L_p(\boldsymbol{\theta}) = L(\boldsymbol{\theta}, \tilde{\boldsymbol{\alpha}}(\boldsymbol{\theta})). \tag{6.7}$$

$\tilde{\boldsymbol{\alpha}}(\boldsymbol{\theta})$ is defined as the $\boldsymbol{\alpha}$ which minimizes $-\ln L(\boldsymbol{\theta}, \boldsymbol{\alpha})$ for fixed $\boldsymbol{\theta}$. This profile likelihood can then be employed for the construction of tests or confidence intervals, for example, the (profile) likelihood ratio

$$\lambda_p(\boldsymbol{\theta}) = \frac{L_p(\boldsymbol{\theta})}{L(\hat{\boldsymbol{\theta}}, \hat{\boldsymbol{\alpha}})}, \tag{6.8}$$

in which $\hat{\boldsymbol{\theta}}$ and $\hat{\boldsymbol{\alpha}}$ are the maximum likelihood estimators. With $\lambda_p(\boldsymbol{\theta})$, one can then determine $\boldsymbol{\theta}$. The obtained intervals for the interesting parameters may not have the exact coverage probability for all possible values of the nuisance parameters. However, according to [111] the approximation is very good in nearly all cases of practical interest.

6.1.1 Parameters of the Likelihood Fit

In this thesis, the observed spectrum is fitted with four individual components: the atmospheric muon flux (see section 2.3), the conventional and prompt atmospheric neutrino flux (see section 2.2.4) and a potential astrophysical neutrino flux (see section 2.2.3). These components are described by various models predicting the number of events as a function of the energy.
The flux of astrophysical neutrinos is modeled as a power law

$$\frac{d\Phi}{dE} = N \cdot \left(\frac{E}{E_0}\right)^{-2} \tag{6.9}$$

with $E_0 = 100\text{TeV}$, and where $N = 10^{-18}\ \text{GeV}^{-1}\text{s}^{-1}\text{sr}^{-1}\text{cm}^{-2}$ is the flux normalization per flavor.[1]
The expected atmospheric muon background is simulated with five component CORSIKA (see section 4.2.2) and weighted according to the poly-gonato model [81]). The energy spectrum is extrapolated from an earlier level of event selection (see section 6.1.4).
The expected background of conventional atmospheric neutrinos (from π-meson and K-meson decay) is modeled according to Honda et al. [82] (see section 2.2.4) and the prompt atmospheric neutrinos (from charm meson decay) according to Enberg et al. [55] (see section

[1] The flux is often also written in the form of $d\Phi/dE = NE^{-2}$, with $N = 10^{-8}\ \text{GeVs}^{-1}\text{sr}^{-1}\text{cm}^{-2}$. The form chosen here in equation 6.9 has the advantage that the definition of N is independent of the power law index.

2.2.4). Since both models do not take into account the knee of cosmic rays, they are modified according to Gaisser's H3a model [62] (see section 2.2.4). The models have substantial uncertainties.
The parameters to be determined with the likelihood fit are the normalizations ϕ of these baseline models. There are three normalization parameters the normalization of the astrophyscial neutrino flux ϕ_{astro}[2], of the conventional atmospheric neutrino flux ϕ_{conv}, and of the prompt atmospheric neutrino flux ϕ_{prompt}. The two last ones, ϕ_{conv} and ϕ_{prompt}, can also be treated as nuisance parameters since this analysis main focus is to investigate the presence of an astrophysical neutrino flux.
In general, nuisance parameters describe systematic uncertainities, which can be expressed with a continous parameter. Assuming the systematic can be parametrized by β and let $\hat{\beta}$ and $\sigma(\beta)$ be our best estimate of β and its uncertainity, respectively. One defines the "pull" ζ of the nuisance parameter as follows

$$\zeta_\beta = \frac{\beta - \hat{\beta}}{\sigma(\beta)}. \tag{6.10}$$

The pull of a nuisance parameter β is the deviation from the expected value of this parameter $\hat{\beta}$ measured in units of its uncertainity $\sigma(\beta)$. Let's assume a set of nuiscance parameters $\boldsymbol{\beta} = \beta_1, ..., \beta_m$, then the deviation of the β_i from their expected values $\hat{\beta}_i$ is taken into account in the likelihood by adding a Gaussian term

$$\prod_{i=1}^{m} \exp\left(-\frac{1}{2}\zeta_i^2\right), \tag{6.11}$$

which leads to the final likelihood function (see equation 6.6)

$$-2\ln\lambda(\boldsymbol{\theta}, \boldsymbol{\zeta}) = 2\sum_{i=1}^{N}\left(\nu_i(\boldsymbol{\theta}, \boldsymbol{\zeta}) - n_i + n_i \ln\frac{n_i}{\nu_i(\boldsymbol{\theta}, \boldsymbol{\zeta})}\right) + \sum_{i=1}^{m}\zeta_i^2. \tag{6.12}$$

In the following, the nuisance parameters used for this analysis are briefly introduced. The systematic shifts described by the nuisance parameters are only applied to the simulation distributions, while the measured data events stay unchanged. The atmospheric muon background flux expectation $dN_\mu/dE \rightarrow \phi_\mu \cdot dN_\mu/dE$, can be shifted up or down. This leads to the nuisance parameter ϕ_μ and its pull

$$\zeta_\mu = \frac{\phi_\mu - \hat{\phi_\mu}}{\sigma(\phi_\mu)}, \quad \hat{\phi_\mu} = 1, \quad \sigma(\phi_\mu) = 0.5, \tag{6.13}$$

where $\sigma(\phi_\mu)$ is the width of the prior, its value is taken from a fit of the atmospheric muon flux (see section 6.1.4).
The uncertainty of the index of the cosmic ray spectrum is also taken into account by a shift

[2] Measured in units of $N = 10^{-18}$ GeV^{-1}s^{-1}sr^{-1}cm^{-2}, see equation 6.9.

of the cosmic ray index $\gamma_{CR} \rightarrow \gamma_{CR} + \Delta\gamma_{CR}$. This shift is expected to directly propagate to the spectra of atmospheric neutrinos. After changing this parameter, the spectrum is re-weighted in order to keep the same total number of neutrinos. This keeps the correlation to the regular normalization parameter small. The pull of the nuisance parameter $\Delta\gamma_{CR}$ is then defined as

$$\zeta_{CR} = \frac{\Delta\gamma_{CR}}{\sigma(\Delta\gamma_{CR})}, \quad \sigma(\Delta\gamma_{CR}) = 0.05 \tag{6.14}$$

The value of $\sigma(\Delta\gamma_{CR}) = 0.05$ was taken from Müller et al. [109].
The uncertainty in the reconstructed energies is mainly due to the ice models and the DOM efficiency, and can be taken into account by a scaling factor α_E for the reconstructed energies $E \rightarrow \alpha_E \cdot E$. The pull of the nuisance parameter α_E is defined as

$$\zeta_E = \frac{\alpha_E - \hat{\alpha}_E}{\sigma(\alpha_E)}, \quad \hat{\alpha}_E = 1, \quad \sigma(\alpha_E) = 0.15. \tag{6.15}$$

The energy resolution of cascades in IceCube is smaller than about 15% [101], therefore $\sigma(\alpha_E) = 0.15$.
Finally, also the normalization of the conventional atmospheric neutrino flux ϕ_{conv} can be treated as a nuisance parameter. Its pull is defined as

$$\zeta_{conv} = \frac{\phi_{conv} - \hat{\phi}_{conv}}{\sigma(\phi_{conv})}, \quad \hat{\phi}_{conv} = 1, \quad \sigma(\phi_{conv}) = 0.25. \tag{6.16}$$

Similar, the normalization of prompt atmospheric neutrino flux ϕ_{prompt} can be treated as a nuisance parameter, too. Its pull is defined as

$$\zeta_{prompt} = \frac{\phi_{prompt} - \hat{\phi}_{prompt}}{\sigma(\phi_{prompt})}, \quad \hat{\phi}_{prompt} = 1, \quad \sigma(\phi_{prompt}) = 0.4. \tag{6.17}$$

For the choice of the uncertainty values $\sigma(\phi_{conv})$ and $\sigma(\phi_{prompt})$ see section 2.2.4 and section 2.2.4. Table 6.1 shows the fit parameters as well as the nuisance parameters and their central values and uncertainity ranges.

6.1.2 Likelihood Implementation

For the likelihood analysis presented in the following, the likelihood software package "Gobal Likelihood Fit" was used. It was developed to fit the results of multiple IceCube analyses in order to check their internal consistency with each other, and to use all available high energy IceCube analyses for an overall fit of the diffuse astrophysical neutrino flux. More information about the "Global Diffuse Likelihood Fit" can be found in [123].
The "Gobal Likelihood Fit" was implemented in python, and the MIGRAD-algorithm from the pyminuit package (see [114]) is used as the default for the numerical minimization of the likelihood function.

fit parameter	nuisance parameter			
	parameter	expected value	uncertainty	pull
ϕ_{astro}	ϕ_μ	$\hat{\phi}_\mu = 1$	$\sigma(\phi_\mu) = 0.5$	ζ_μ
γ	$\Delta\gamma_{CR}$	0	$\sigma(\Delta\gamma_{CR}) = 0.05$	ζ_{CR}
ϕ_{conv}	α_E	$\hat{\alpha}_E = 1$	$\sigma(\alpha_E) = 0.15$	ζ_E
ϕ_{prompt}	ϕ_{conv}	$\hat{\phi}_{conv} = 1$	$\sigma(\phi_{conv}) = 0.25$	ζ_{conv}
	ϕ_{prompt}	$\hat{\phi}_{prompt} = 1$	$\sigma(\phi_{prompt}) = 0.4$	ζ_{prompt}

Table 6.1: *The fit parameters and the nuisance parameters taken into account for the likelihood fit. The normalizations of the conventional atmospheric neutrino flux ϕ_{conv} and the prompt atmospheric neutrino flux ϕ_{prompt} can be used either as free fit parameter or as nuisance parameter.*

6.1.3 Data Sample and Simulations

The likelihood fit is based on the data and simulated events, which survive the Level 5 event selection (see section 5.5). The energy range of the likelihood fit is 10 TeV $\leq E \leq$ 10 PeV[3], which allows to check the consistency of data and MC predictions at lower energies and increases the amount of information available. Therefore, the likelihood fit can constrain the background contributions better. This event selection will be called the likelihood fit event selection or the likelihood fit sample from now on. Figure 6.1 shows the energy spectrum used for the likelihood analysis.

6.1.4 Muon Background Estimation

The likelihood fit sample does not contain simulated muons for $E > 38$ TeV. This makes the proper muon background estimation challenging. It was not possible to simulate higher statistics of atmospheric muons due to limitations in computing power and time. The ansatz to solve this problem ([107]) which will be described briefly in the following, was developed in the framework of the Global Likelihood Fit.
To be able to predict the number of remaining atmospheric muons continously, and to avoid low MC statistics, the number of atmospheric muons was fit. Their energy spectrum (dN/dE) follows the cosmic ray flux with a power law index $\gamma \approx -3.7$. Of course this does not take the selection efficiency into account which is expected to vary with energy.
Since the remaining atmospheric muons in the likelihood fit event selection look similar to cascade-like events (otherwise they would have been cut away), one can instead use the relative electron neutrino efficiencies as a proxy, which are easier to determine due to much higher simulation statistics. The relative efficiency ϵ_{rel} as a function of the visible energy in

[3] For $E > 10$ TeV, one year livetime of atmospheric muon simulation is available (see section 4.2.3).

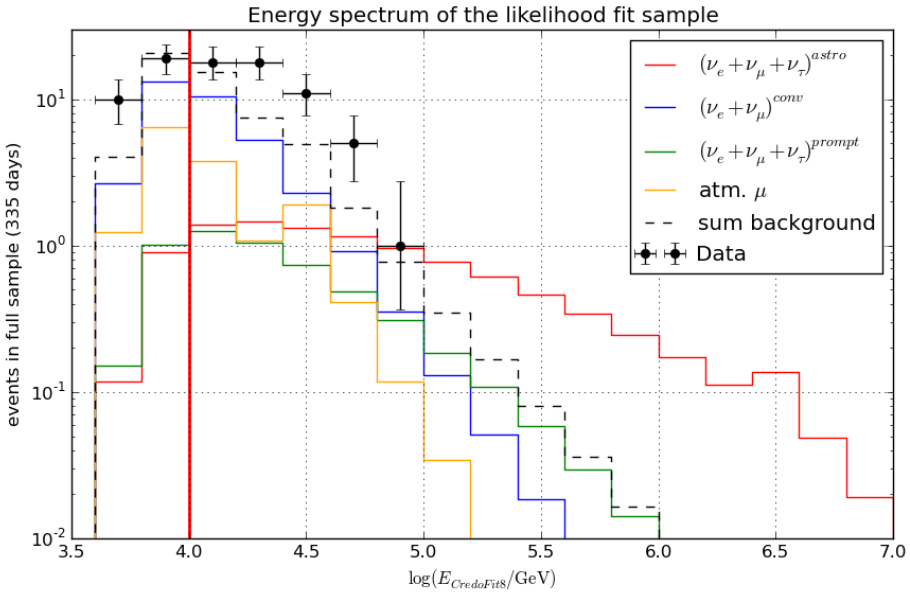

Figure 6.1: *The energy spectrum of Level 5 events in the full IC59 sample. The error bars on the data correspond to the 68 % Feldman-Cousins intervals [57]. The simulated atmospheric muon background is shown in orange. For* $\log(E/\mathrm{GeV}) > 4.58$*, the muon background is obtained by the extrapolation described in eq. 5.24. The simulated conventional and prompt atmospheric neutrino fluxes according to [82] and [55] are shown in blue and green, respectively. The red line shows the sum of the simulated astrophysical* E^{-2} *electron, muon and tau neutrino spectra (1:1:1). The total background, consisting of the conventional and prompt atmospheric neutrinos and the atmospheric muons, is shown by the black dashed line. The red vertical line corresponds to the energy threshold (*$\log(E/\mathrm{GeV}) > 4.00$*) chosen for the likelihood fit.*

the detector E_{vis} can be defined by

$$\epsilon_{rel}\left(E_{vis}\right) = \frac{n_{final}\left(E_{vis}\right)}{n_{interacting}\left(E_{vis}\right)} \tag{6.18}$$

wherein $n_{final}\left(E_{vis}\right)$ is the number of electron neutrinos surviving the final event selection and $n_{interacting}\left(E_{vis}\right)$ the number of simulated electron neutrinos interacting in the detector. Figure 6.2 shows the fractional selection efficiency and the spline used for interpolation.

Figure 6.3 shows the power-law fit ($dN/d\log E = N_0 \cdot (E/E_0)^{-\gamma_\mu}$) of the expected muon background taking into account the energy-dependent relative detector efficiency from figure 6.2. The fit was applied on the remaining simulated muon events after Level 5. The spectral index was fit to $\gamma_\mu = -3.57 \pm 0.52$ and the normalization adapted to represent the (4.3 ± 0.7) surviving simulated muon events above $E = 10\mathrm{TeV}$. This fit was used in the likelihood calculations for the muon background prediction.

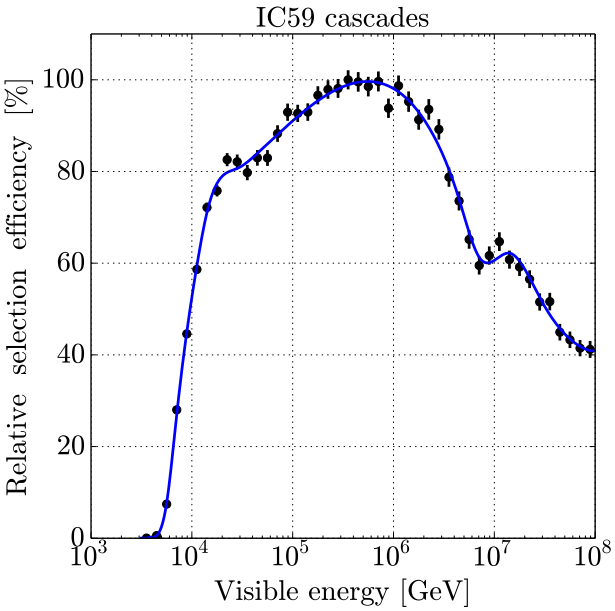

Figure 6.2: *The relative efficiency of a simulated electron neutrino to appear in the final event selection as a function of the energy E_{vis} (see section 5.5.5) it deposits in the detector, taken from [107].*

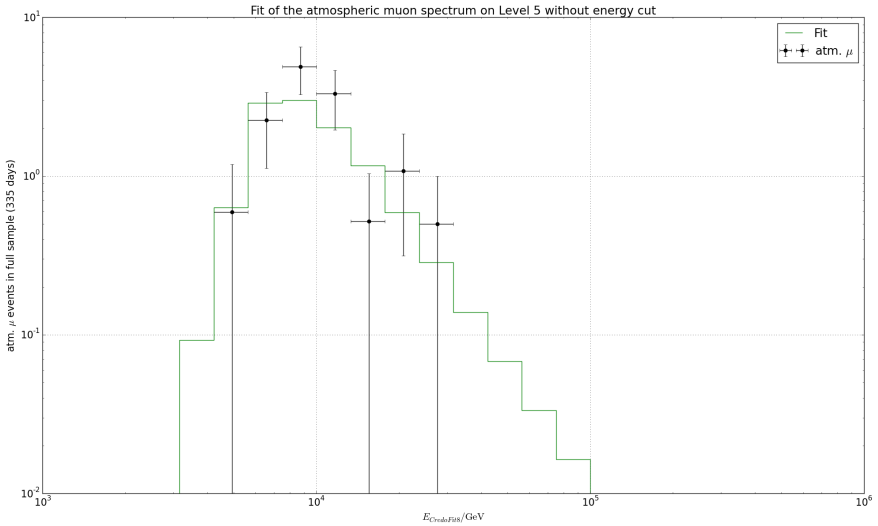

Figure 6.3: *The fit of the energy distribution of the remaining simulated atmospheric muons after Level 5. The fit model is a power law multiplied with the efficiency curve shown in figure 6.2. The black data points are the simulated muons. The green line shows the fit.*

6.1.5 Likelihood Tests

One can test the likelihood implementation by checking how well known input parameters are reconstructed. Therefore, data was sampled from the energy spectrum of the MC distributions with the normalizations of the baseline models (see section 6.1.1) $\phi_{astro} = \phi_{conv} = \phi_{prompt} = 1$ and $\gamma = 2$. These data samples were then fit with the likelihood fit. With a sufficiently large number of toy data sets, one can study the distribution of the reconstructed parameters in relation to the input parameters. This is shown for parameters of interest in figure 6.4.
For each parameter the mean (μ) and the standard deviation (σ) of the distribution were calculated (see "Histogram" in figure 6.4). Additionally, the distributions were fitted with a Gaussian and its mean and width were determined. One can see that the conventional flux normalization is reconstructed well but slightly shifted ($\mu = 0.89$) and has a width of $\sigma = 0.35$. The normalization of prompt atmospheric neutrino flux also has a small shift ($\mu = 1.03$) and width $\sigma = 0.20$, too. The astrophysical flux normalization is shifted to $\mu = 0.91$ and has a width of $\sigma = 0.35$. The shift of the astrophysical flux index γ is also small ($\mu = 2.01$) with a width of $\sigma = 0.35$.
Figure 6.5 shows the correlation between the reconstructed parameters. There are interdependences between the normalization of the astrophysical flux and the prompt flux, between the normlizations of the conventional and astrophysical flux and between normalizations of the conventional and prompt flux. A higher number of measured data events above the expected background can be absorbed in a larger normalization of either the prompt flux or the astrophysical flux in the given energy range. Only data events measured at higher energies can dissolve this ambiguity since the spectrum of the prompt flux is much steeper at higher energies than that of the expected astrophysical flux. Therefore, measured data events at very high energies (about hundreds of TeV) are important for the discovery of the astrophysical neutrino flux.

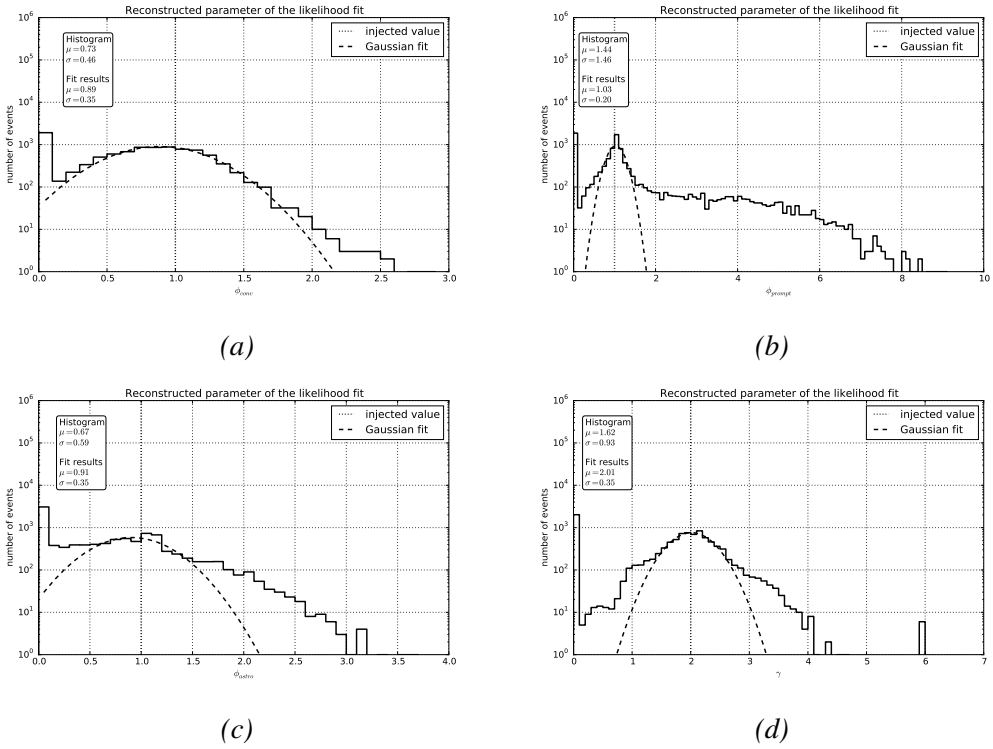

Figure 6.4: *The bias of the reconstructed parameter values of the conventional atmospheric neutrino flux normalization ϕ_{conv} (a), the normalization of the prompt flux ϕ_{prompt} (b), the normalization of the astrophysical neutrino flux (c), and the astrophysical neutrino flux index γ_{astro} (d). The dashed line shows the input parameter while the black line shows the distribution of the reconstructed parameters. For each parameter the mean μ and the standard deviation σ of the distribution were calculated ("Histogram"). Additionally, the distributions were fitted with a Gaussian and its mean μ and width σ were determined ("Fit results").*

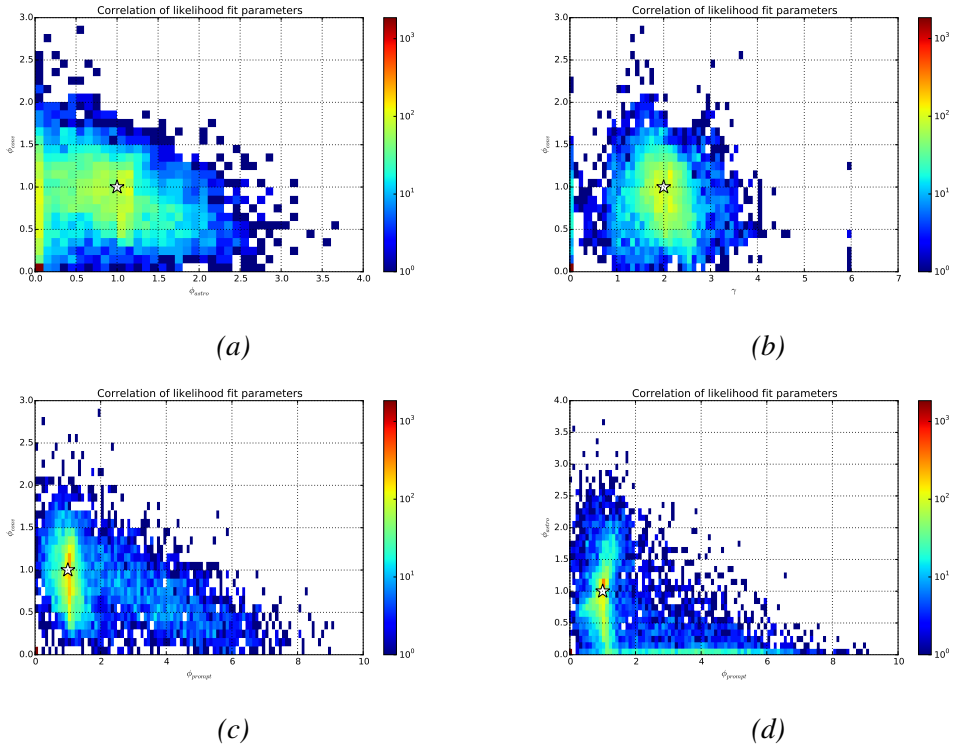

(a) *(b)* *(c)* *(d)*

Figure 6.5: *The correlation between the reconstructed parameter values of the astrophysical neutrino flux normalization ϕ_{astro} and the conventional flux normalization ϕ_{conv} (a), the astrophysical flux index γ and the conventional flux normalization ϕ_{conv} (b), the prompt atmospheric flux normalization ϕ_{prompt} and the conventional flux normalization ϕ_{conv} (c), and the prompt atmospheric flux normalization ϕ_{prompt} and the astrophysical neutrino flux normalization ϕ_{astro}. The star shows the inserted values of each pair of parameters. The colors represent how often a certain combination was reconstructed.*

6.2 Results

This section describes the application of the likelihod fit to the measured data events.
The fit parameters are the normalization of the conventional and prompt atmospheric neutrino flux ϕ_{conv} and ϕ_{prompt}, and the index γ and flux normalization ϕ_{astro} of a possible diffuse astrophysical neutrino flux (see section 6.1.1). Figure 6.6 shows the described baseline models and the measured data points.

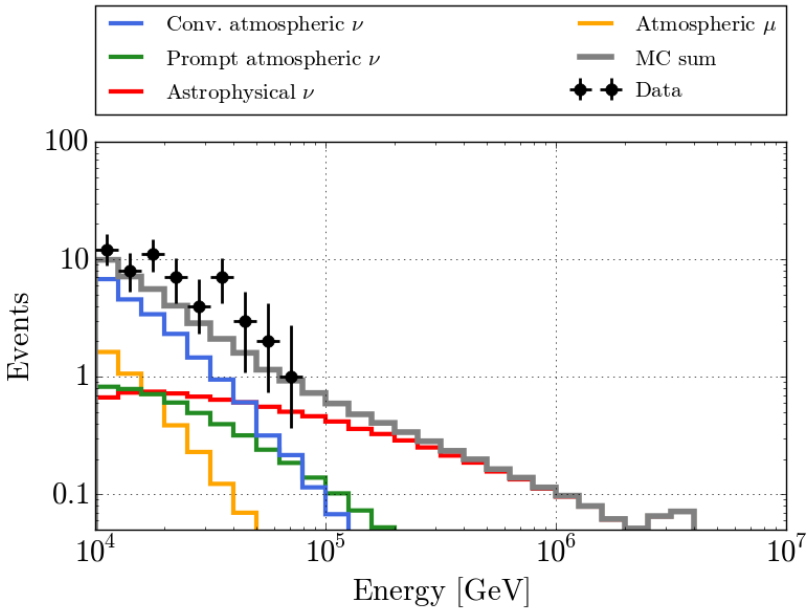

Figure 6.6: *The baseline models of the likelihood fit. The blue line shows the expected conventional atmospheric neutrino flux [82] and the green line the expected prompt atmospheric neutrino flux [55], both modified according to Gaisser's H3a model [62] (see section 6.1.1). The orange line shows the expected atmospheric muon flux (see section 6.1.4). The simulated astrophysical neutrino flux is plotted in red (see section 6.1.1). The gray line shows the sum of all simulated fluxes. The measured events of the full data sample (335 days) are represented by the black data points.*

Additional parameters - the nuisance parameters - take into account some systematic uncertainties and are also fit as described in section 6.1.
Different hypotheses have been fit to the data and are discussed in the following sections. In all cases the fit was performed in the range from $\log(E_{CredoFit8}/\text{GeV}) = 4.0$ ($E_{CredoFit8} = 10$ TeV) to $\log(E_{CredoFit8}/\text{GeV}) = 7.0$ ($E_{CredoFit8} = 10$ PeV).[4]

[4]The upper energy boundary of 10 PeV is chosen as in [123].

6.2.1 Hypothesis H0

In the H0 hypothesis, the normalizations of the astrophysical neutrino flux ϕ_{astro}, the conventional and prompt atmospheric neutrino flux ϕ_{conv} and ϕ_{prompt} were free fit parameters. The astrophysical neutrino flux index was fixed to $\gamma = 2$. The nuisance parameters ϕ_μ, $\Delta\gamma_{CR}$ and α_E were set according to table 6.1. Figure 6.7 shows the best fit results to the data for hypothesis H0.

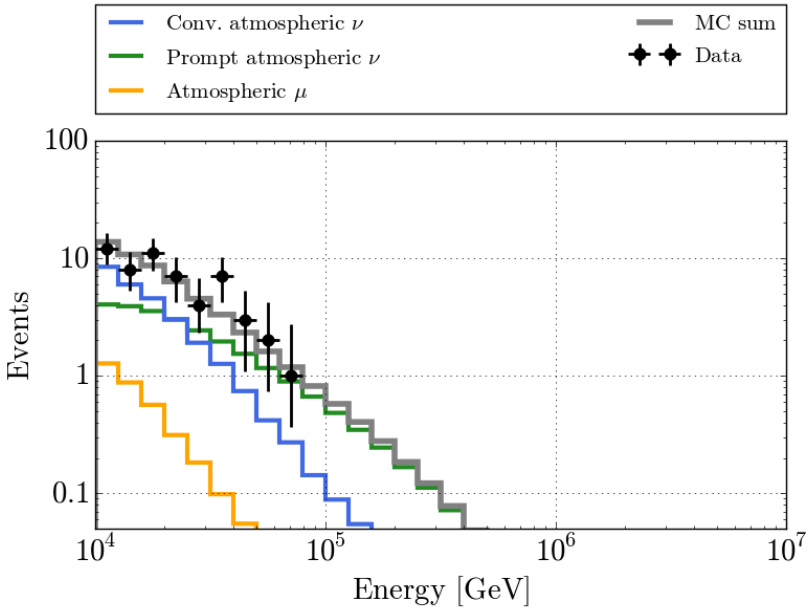

Figure 6.7: *The best fit likelihood results for hypothesis H0 applied to the data events (black markers). For a description of the lines and the models see figure 6.6. No astrophysical flux is fit to the data events. The conventional and prompt atmospheric neutrino fluxes are fit to higher values (compare with figure 6.6) to absorb the excess of data events.*

The normalization of the astrophysical flux was fit to zero. The excess of data events are accommodated by a 1.52 times higher normalization of the conventional atmospheric neutrino flux ([82] with the [62] modification) and a 5.34 times higher prompt atmospheric neutrino flux ([55] with the [62] modification). Table 6.2 shows the results of the fit and nuisance parameters for this hypothesis. The deviations of the pulls of the nuisance parameters from their mean values is smaller than about 1σ (see table 6.1). Figure 6.8 shows the scans of the likelihood for the fit and nuisance parameters.

Since the normalization of the astrophysical neutrino is fit to zero, one can derive an upper limit for it from the likelihood profile. Assuming that the number of neutrinos of each flavor arriving earth is the same ($\nu_e : \nu_\mu : \nu_\tau = 1 : 1 : 1$), the 90% confidence upper limit on an

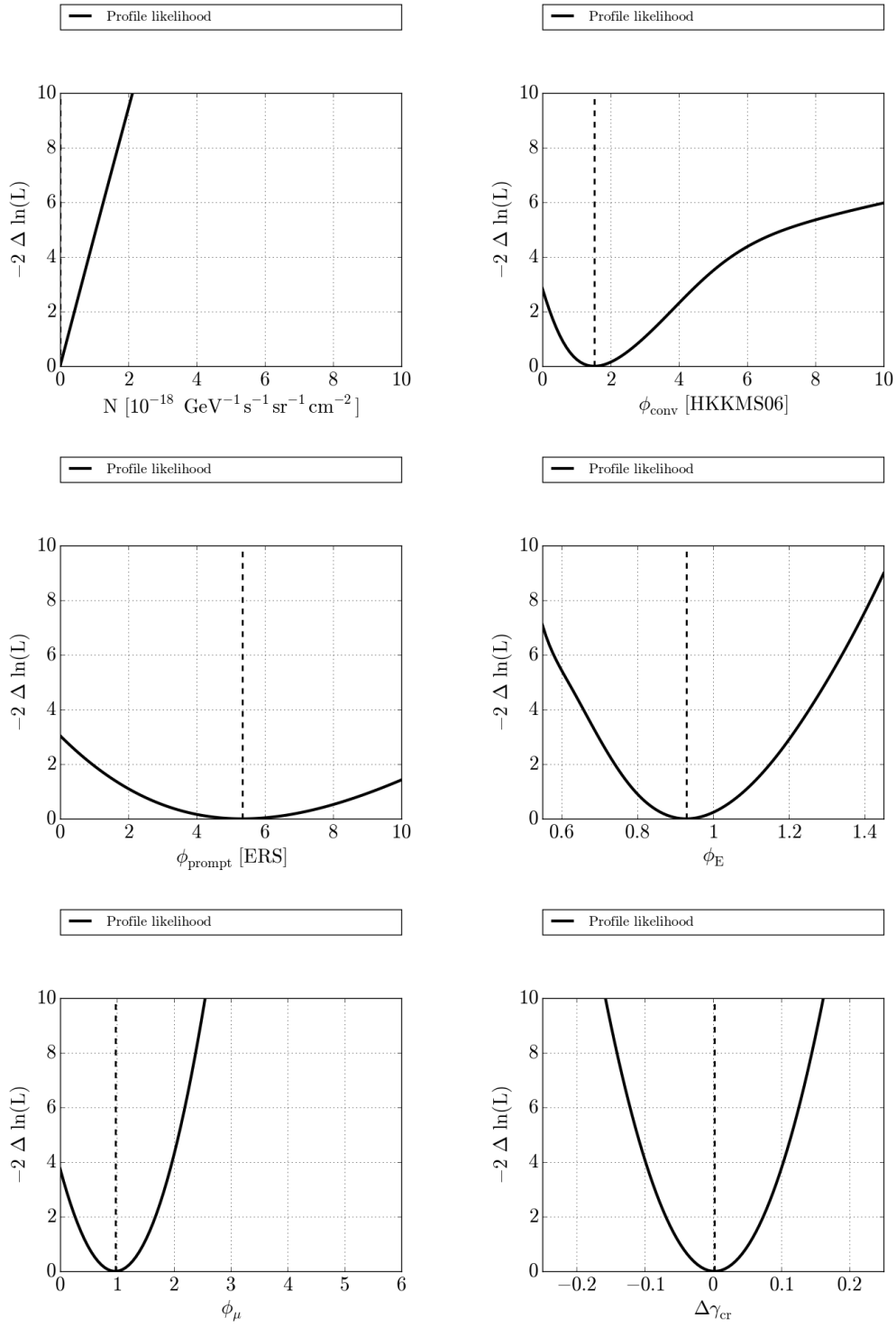

Figure 6.8: *The likelihood scans of the fit and nuisance parameters of hypothesis H0 (see section 6.1.1 and table 6.2). The minimum of each parameter is indicated by the dashed line.*

Likelihood fit results for H0	
$\phi_{conv} = 1.52^{+1.42}_{-0.96} \cdot \Phi_{Honda}$	$\zeta_\mu = -0.06^{+1.00}_{-1.00}$
$\phi_{prompt} = 5.34^{+3.82}_{-3.19} \cdot \Phi_{Enberg}$	$\zeta_E = -0.47^{+1.01}_{-0.90}$
$\phi_{astro} = 0^{+0.21}_{-0} \cdot N$	$\zeta_{CR} = +0.05^{+1.01}_{-1.01}$
$-2\ln(LLH) = 10.5$	

Table 6.2: *The likelihood fit and nuisance parameters (see section 6.1.1) for hypothesis H0 as well the likelihood value. Φ_{Honda} and Φ_{Enberg} are the models described in [82] and [55], modified by [62]. The parameter errors are the 68% confidence intervals from scanning the likelihood. The pulls ζ_μ, ζ_E and ζ_{CR} are defined in section 6.1.1.*

astrophysical flux with power-law index -2 is

$$E^2\Phi^{H0}_{astro,\,ul} = 1.70 \cdot 10^{-8}\ \mathrm{GeVs^{-1}sr^{-1}cm^{-2}}, \tag{6.19}$$

in the energy range 20 TeV $\leq E \leq$ 3.0 PeV.[5] It lies slightly below the Waxman-Bahcall upper bound of $E^2\Phi_{WB} < 3.4 \cdot 10^{-8}$ GeVs^{-1}sr^{-1}cm^{-2} [129].

6.2.2 Hypothesis H1

Hypothesis H1 checks if a restricted range for the normalization of the prompt atmospheric neutrino flux would lead to a non-vanishing astrophysical neutrino flux. Therefore, in hypothesis H1 the normalization of the prompt flux was treated as a nuisance parameter. Therefore a Gaussian penalty term with a width of ±40% of the normalization of Φ_{Enberg}, according to its theoretical uncertainty (see section 2.2.4), was added to the likelihood. Table 6.3 shows the results of the likelihood fit.

Since the normalization of the prompt atmospheric neutrino flux is restricted, the excess of data events results in an increase of the normalization of the conventional atmospheric neutrino flux $\phi_{conv} = 2.70^{+1.44}_{-0.97} \cdot \Phi_{Honda}$. Such a high conventional atmospheric neutrino flux is excluded by measurements [7]. The normalization of the astrophysical neutrino flux is still fit to zero. Figure 6.9 shows the best fit results to the data for hypothesis H1.

[5] The lower bound of the energy range is defined as the primary neutrino energy at which the upper limit is 5% higher than the upper limit (see equation 6.19). In order to determine this minimum energy, the upper limit calculation was iterated, increasing the primary energy cut on the simulated astrophysical neutrino events with each iteration. A minimum energy of 20 TeV was found using this method, which is described in [118]. The upper bound of the energy range is defined as the primary neutrino energy for which 95% of the simulated astrophysical neutrinos have smaller energies, giving a maximum energy of 3 PeV.

Likelihood fit results for H1	
$\phi_{conv} = 2.70^{+1.44}_{-0.97} \cdot \Phi_{Honda}$	$\zeta_\mu = -0.13^{+1.00}_{-1.00}$
$\phi_{prompt} = 1.08^{+0.40}_{-0.40} \cdot \Phi_{Enberg}$	$\zeta_E = -0.56^{+1.09}_{-0.84}$
$\phi_{astro} = 0^{+0.38}_{-0} \cdot N$	$\zeta_{CR} = -0.29^{+0.99}_{-0.99}$
$-2\ln(LLH) = 12.4$	

Table 6.3: *The likelihood fit and nuisance parameter (see section 6.1.1) for hypothesis H1 as well the likelihood value. Φ_{Honda} and Φ_{Enberg} are the models described in [82] and [55] modified by [62]. The parameter errors are the 68% confidence intervals from scanning the likelihood. The pulls ζ_μ, ζ_E and ζ_{CR} are defined in section 6.1.1.*

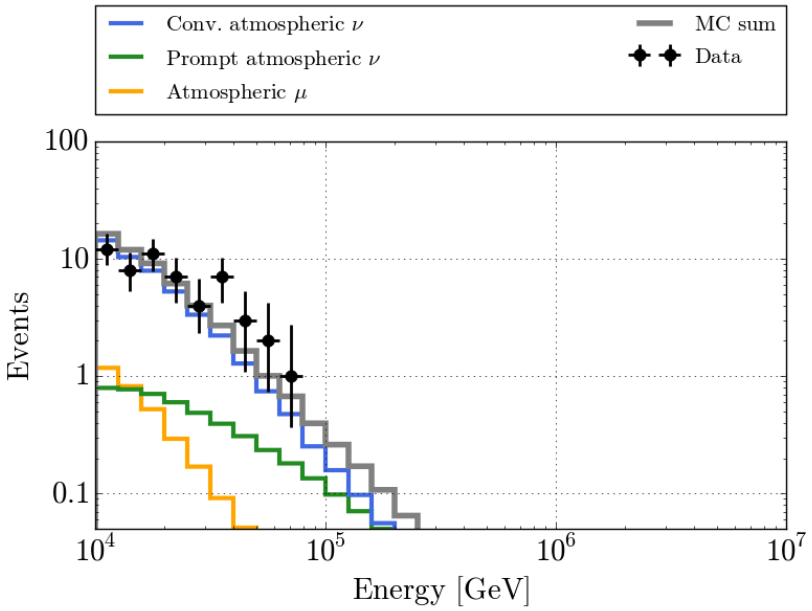

Figure 6.9: *The best fit likelihood results for hypothesis H1 applied to the data events (black markers). For a description of the lines and the models see figure 6.6. The astrophysical flux is still reduced to zero by the fit. The conventional atmospheric neutrino flux is instead fit to a higher value (compare with figure 6.6) to absorb the excess of data events. The prompt atmospheric neutrino flux was treated as a nuisance parameter and restricted to ±40% of its normalization as predicted by [55].*

6.2.3 Hypothesis H2

Hypothesis H2 is similar to H1 with an additional constraint placed on the conventional atmospheric neutrino flux normalization. This is now also treated as a nuisance parameter. Therefore, a Gaussian penalty term with a width of ±25% of the normalization of the value of Φ_{Honda} [82], was added to the likelihood (see section 2.2.4). Table 6.4 shows the best fit values for hypothesis H2. Figure 6.10 shows the best fit to the data.

Likelihood fit results for H2	
$\phi_{conv} = 1.20^{+0.22}_{-0.21} \cdot \Phi_{Honda}$	$\zeta_\mu = 0.17^{+0.97}_{-0.97}$
$\phi_{prompt} = 1.20^{+0.39}_{-0.39} \cdot \Phi_{Enberg}$	$\zeta_E = 1.29^{+0.92}_{-0.74}$
$\phi_{astro} = 0^{+0.48}_{-0} \cdot N$	$\zeta_{CR} = -0.25^{+0.99}_{-0.99}$
$-2\ln(LLH) = 16.3$	

Table 6.4: *The likelihood fit and nuisance parameters (see section 6.1.1) for hypothesis H2 as well the likelihood value. Φ_{Honda} and Φ_{Enberg} are the models described in [82] and [55] modified by [62]. The parameter errors are the 68% confidence intervals from scanning the likelihood. The pulls ζ_μ, ζ_E and ζ_{CR} are defined in section 6.1.1.*

The astrophysical flux normalization is still fit to zero in this scenario. Since the normalization of the atmospheric neutrino fluxes are now restricted, the nuisance parameter of the energy scale is now fit to a higher value ($\zeta_E = 1.29^{+0.92}_{-0.74}$) in order to absorb the excess in the data. Furthermore, the atmospheric muon rate increases slightly. Figure 6.11 shows the scans of the likelihood for the fit and nuisance parameters.
The 90% confidence upper limit on an all-flavor astrophysical neutrino flux with power-law index −2 is

$$E^2\Phi^{H2}_{astro,\,ul} = 3.2 \cdot 10^{-8}\ \mathrm{GeVs^{-1}sr^{-1}cm^{-2}}, \tag{6.20}$$

in the energy range 20 TeV ≤ E ≤ 3.0 PeV. Due to the contraints on the conventional and prompt atmospheric neutrino flux, the upper limit of the astrophysical neutrino flux is higher than in hypothesis H0 (see section 6.2.1).
The value of the minimum of the likelihood function is $-2\ln(LLH) = 16.3$, which is larger compared to the value $-2\ln(LLH) = 10.5$ of hypothesis H0 and $-2\ln(LLH) = 12.4$ of hypothesis H1, respectively.

6.2.4 Hypothesis H3

Hypothesis H3 is similar to hypothesis H2, but the index of the astrophysical neutrino flux is no longer fixed to $\gamma = 2$. It is now an extra fit parameter of the likelihood fit.

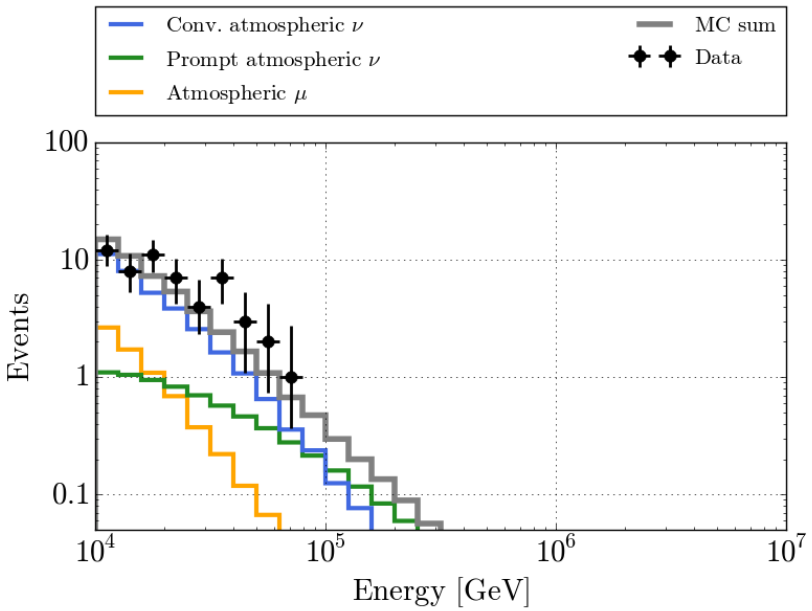

Figure 6.10: *The best fit likelihood results for hypothesis H2 applied to the data events (black markers). For a description of the lines and the models see figure 6.6. The astrophysical flux is still fit to zero. The prompt atmospheric neutrino flux was treated as a nuisance parameter and restricted to ±40% of its normalization predicted by [55], and also the conventional atmospheric neutrino flux was treated as a nuisance parameter and restricted to ±25% of its normalization as predicted by [82].*

Table 6.5 shows the best fit values for hypothesis H3. Figure 6.12 shows the best fit to the data.

The normalization of the conventional and prompt atmospheric neutrino flux are fit to the values predicted by their models ([82] and [55] modified by [62]). The values of the nuisance parameters are all relatively close to zero. Figures 6.13 and 6.14 show the scans of the likelihood for the fit and nuisance parameters for hypothesis H3. The astrophysical flux normalization is no longer zero in this scenario, but has a value of $1.37^{+1.08}_{-0.75} \cdot N$ (see equation 6.9). The excess of the data over the simulated background is now accommodated by the addition of the astrophysical neutrino flux. The minimum value of the likelihood is the same as for hypothesis H0, in which no astrophysical flux was found (see section 6.2.1). Considering only the value of the minimum of the likelihood, one can not decide between the two different hypotheses H3 and H0 with the data sample used in this analysis.
Under the assumption that the prompt atmospheric neutrino flux is within the uncertainties used in hypothesis H3, the existence of an astrophysical neutrino flux is preferred by 2.4σ, when hypothesis H3 is compared to hypothesis H2 applying Wilks' theorem [131]. However, the likelihood fit result for the index $\gamma = 3.14^{+0.36}_{-0.34}$ (see table 6.5) is a much larger value than expected for an astrophysical neutrino flux (see section 2.1.2) and lies more between the

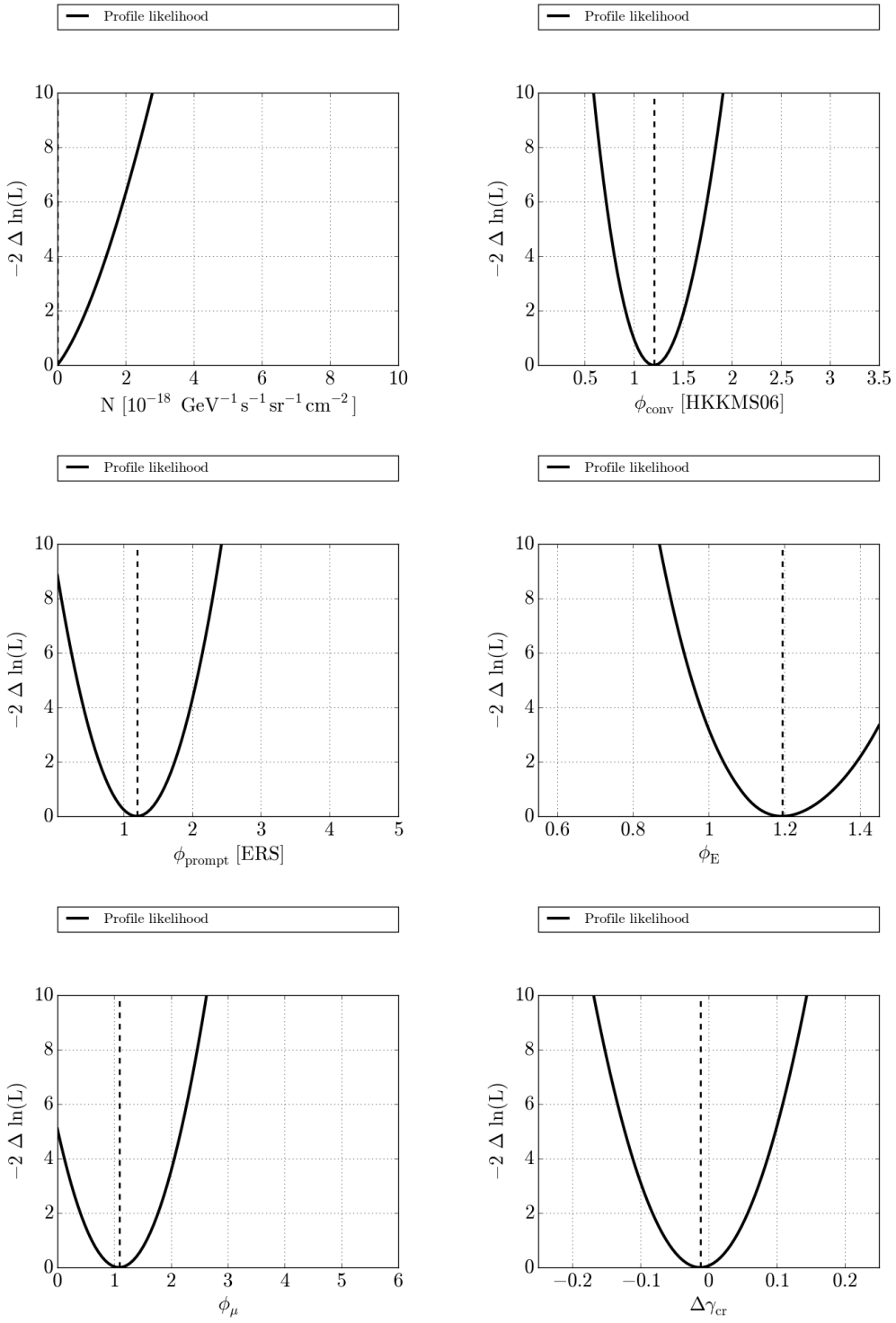

Figure 6.11: *The plot shows the likelihood scans of the fit and nuisance parameters of hypothesis H2 (see section 6.1.1 and table 6.4). The minimum of each parameter is indicated by the dashed line.*

Likelihood fit results for H3	
$\phi_{conv} = 0.99^{+0.25}_{-0.25} \cdot \Phi_{Honda}$	$\zeta_\mu = -0.10^{+1.00}_{-1.00}$
$\phi_{prompt} = 1.00^{+0.40}_{-0.40} \cdot \Phi_{Enberg}$	$\zeta_E = -0.46^{+0.99}_{-0.99}$
$\phi_{astro} = 1.37^{+1.08}_{-0.75} \cdot N$	$\zeta_{CR} = -0.03^{+1.00}_{-1.00}$
$\gamma = 3.14^{+0.36}_{-0.34}$	
$-2\ln(LLH) = 10.5$	

Table 6.5: *The likelihood fit and nuisance parameters (see section 6.1.1) for hypothesis H3 as well the likelihood value. Φ_{Honda} and Φ_{Enberg} are the models described in [82] and [55] modified by [62]. The astrophysical neutrino flux Φ_{astro} is measured in units of $N = 10^{-18}$ GeV^{-1}s^{-1}sr^{-1}cm^{-2} (see equation 6.9). The parameter errors are the 68% confidence intervals from scanning the likelihood. The pulls ζ_μ, ζ_E and ζ_{CR} are defined in section 6.1.1.*

indices of the conventional and prompt atmospheric neutrino flux (see section 2.2.4).

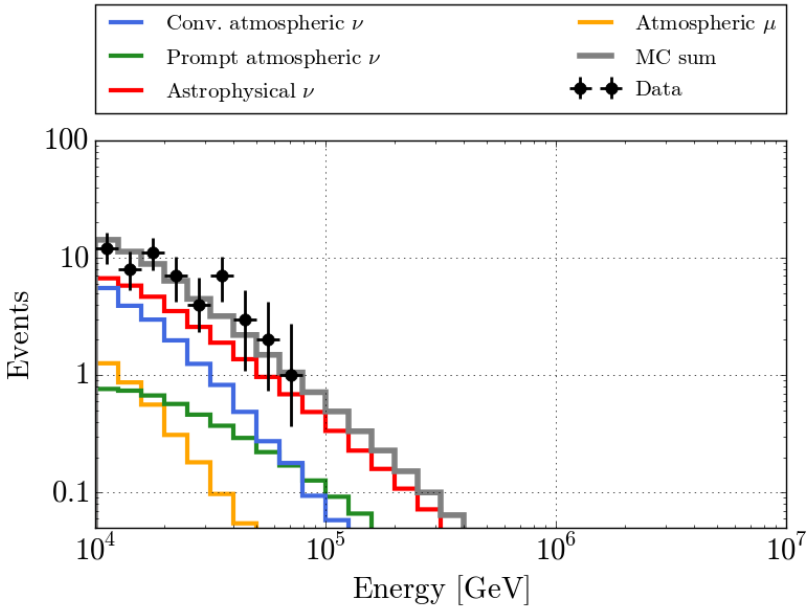

Figure 6.12: *The best fit likelihood results for hypothesis H3 applied to the data events (black markers). For a description of the lines and the models see figure 6.6. The prompt atmospheric neutrino flux was treated as a nuisance parameter and restricted to ±40% of its normalization predicted by [55]. Also the conventional atmospheric neutrino flux was treated as a nuisance parameter and restricted to ±25% of its normalization as predicted by [82]. A non-vanishing astrophysical neutrino flux component was obtained from the likelihood fit to the data (see table 6.5).*

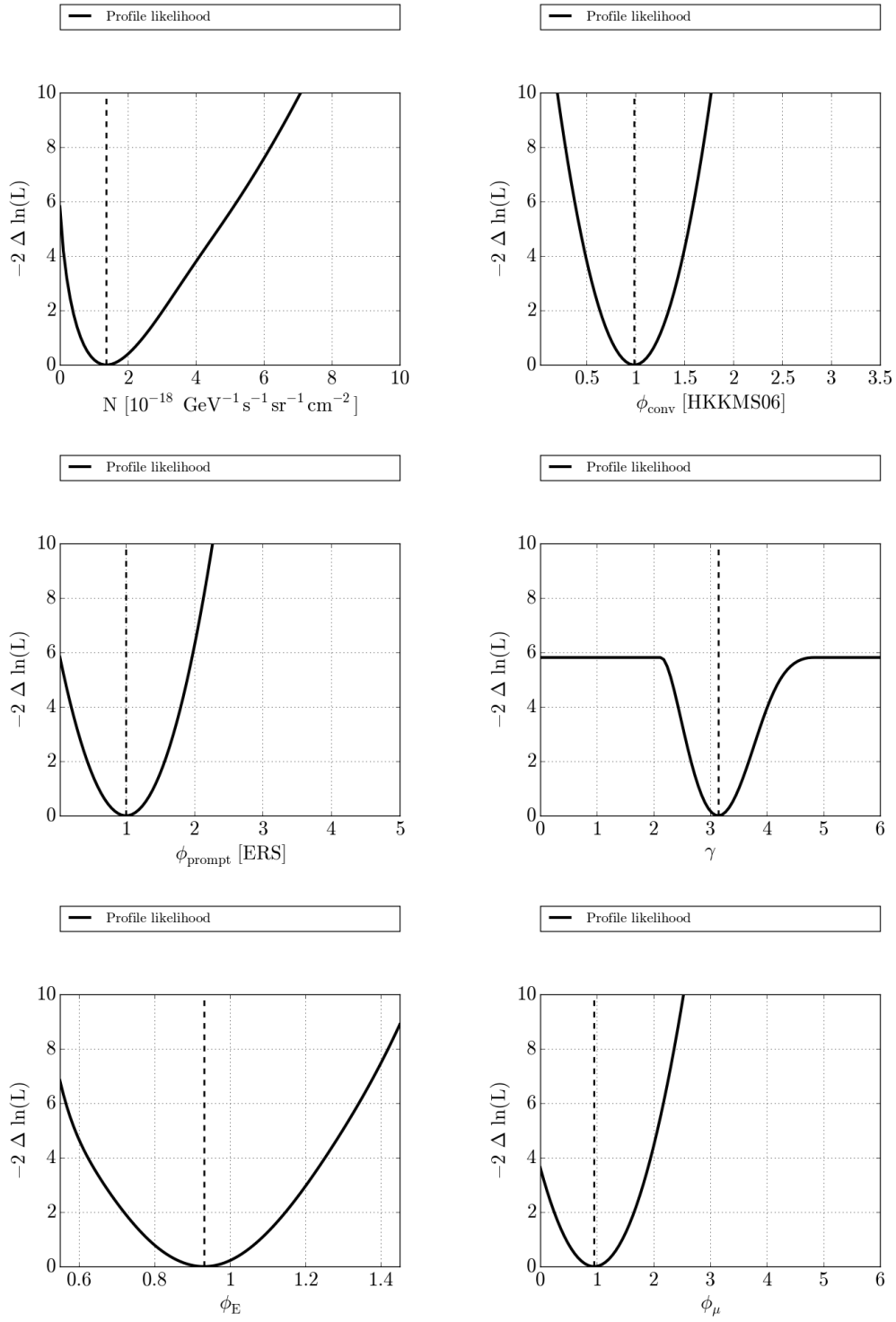

Figure 6.13: *The likelihood scans of the fit and nuisance parameters of hypothesis H3 (see section 6.1.1 and table 6.5). The minimum of each parameter is indicated by the dashed line.*

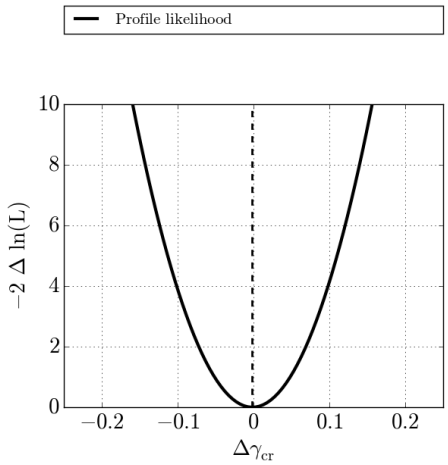

Figure 6.14: *The likelihood scans of the fit and nuisance parameters of hypothesis H3 (continuation of figure 6.13).*

6.3 Discussion

Meanwhile, the astrophysical neutrino flux was discovered by another IceCube analysis, consisting of two years of data. This analysis is introduced in the following and it results are compared to the results of the analysis of this thesis.
Compared to this new analysis and also to a previous IceCube analysis [5], the energies of the highest energy events found in this analysis were rather small. The significance of this effect was studied and is discussed in the following.

6.3.1 The astrophysical neutrino flux discovery with two years of IC79 and IC86 data

The analysis [1] is based on more recent data from 2010 to 2012 with a total livetime of 662 days. In the first year, the detector consisted of 79 strings, while in the second year it was complete (86 strings).
A fiducial volume event selection was introduced for the analysis. Only events which have their Cherenkov first light emission within the fiducial volume were accepted. If more than two of the first 250 observed photoelectrons of an event were recorded in the veto region, the event was rejected.
Another necessary requirement is that the event consists at least of 6000 photoelectrons. This ensures that muons entering the fiducial volume from outside would produce light in the veto region and therefore would be rejected. The muon background above the 6000 photoelectron threshold is reduced by 99.999%, while nearly all events from neutrinos with energies of some hundreds of TeV which occur in the fiducial volume are retained.
In the 662 days live time data set, 28 events were found with energies from 30 up to 1200 TeV. There are two PeV events in the sample, which belong to the group of highest energy neutrino events ever measured. The number of expected background events from atmospheric neutrinos and muons was $10.6^{+5.0}_{-3.6}$. Of these, 21 events were cascade-like, while the remaining 7 had clear muon tracks.

The data was fit with free parameters for the prompt and conventional atmospheric neutrino flux, as well as an E^{-2} power-law for a possible astrophysical neutrino flux component. In the energy range 60 TeV $< E <$ 2 PeV of the fit, the expected contribution from atmospheric background events is very small. Figure 6.15 shows the energy spectrum of the 28 data events and the expected atmospheric background contributions. Fitting an E^{-2} power law spectrum to the data, one obtains a flux normalization per flavor (assuming $\nu_e : \nu_\mu : \nu_\tau = 1 : 1 : 1$) of

$$E^2\Phi_{astro}^{per\ flavor} = (1.2 \pm 0.4) \cdot 10^{-8}\mathrm{GeVs}^{-1}\mathrm{sr}^{-1}\mathrm{cm}^{-2}, \tag{6.21}$$

as published in [1].
This is equal to an all-flavor flux of

$$E^2\Phi_{astro} = (3.6 \pm 1.2) \cdot 10^{-8}\mathrm{GeVs}^{-1}\mathrm{sr}^{-1}\mathrm{cm}^{-2}. \tag{6.22}$$

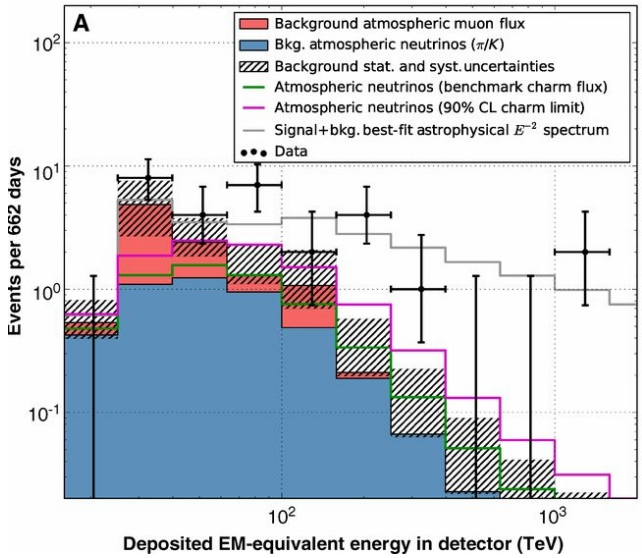

Figure 6.15: *The energy spectrum of the 28 measured events in [1]. The x-axis shows the reconstructed energy in the detector, which is a lower limit on the neutrino energy. The blue line shows the expected atmospheric neutrino rate and the red one shows the expected atmospheric muon rate. The hatched area denotes the combined statistical and systematic uncertainties of the total background. The best-fit E^{-2} astrophysical is shown by the gray line.*

Even though the current statistics are limited, the resulting flux normalization (see equation 6.22) would predict three to six additional events in the energy range from 2 PeV up to 10 PeV. Since these events are not present in the data sample, this maybe an indication of a softer energy spectrum (the best fit is $E^{-2.2\pm0.4}$) or a cutoff at about PeV energies.

6.3.2 Comparison of the finding of this work with IC79&IC86

An important difference between the analysis presented here and the analysis using both the data of IC79 and IC86 configurations called IC79&IC86 is clearly the number of events and their energies. While the 8 events found in the analysis presented in this thesis (for $E \geq 38$ TeV, see section 5.6) have reconstructed energies between 39 TeV and 67 TeV, 15 events out of 28 from the IC79&IC86 analysis have energies above 67 TeV, and 9 events have energies above 100 TeV, from which 6 have energies above 200 TeV. As one can see from the figure 6.15, these highly energetic events strongly constrain the astrophysical neutrino flux.
Figure 6.16 shows the comparison of the effective areas (see section 5.5.7) of this analysis, starting with values of about 0.4 m^2 (at 10^4 GeV) and increasing up to 100 m^2 for the highest energies, to the IC79&IC86 analysis. Qualitatively comparing the effective areas, one would expect more lower energy events in the the IC59 analysis, and more higher energy events in the IC79&IC86. Additionally, one expects at least a factor of two in the event number ratio

of the analyses, since the IC79&IC86 analysis contains two years of data.

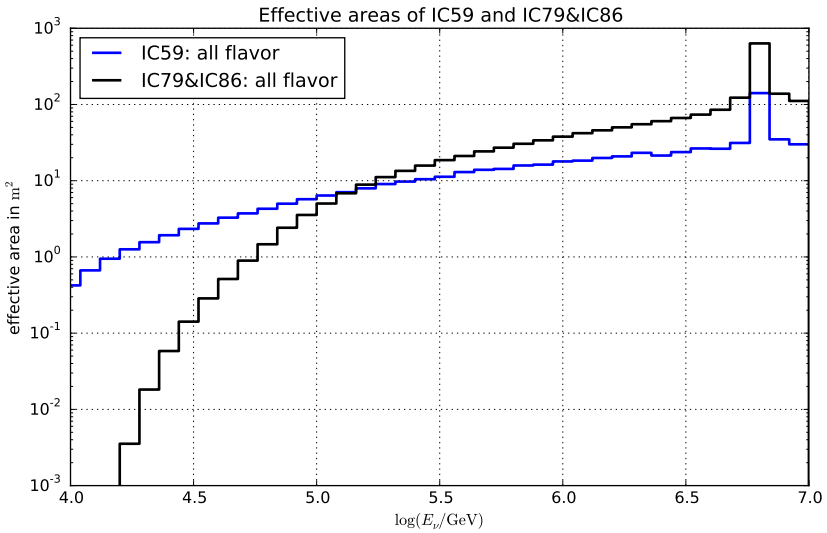

Figure 6.16: *The effective areas for this analysis (blue) and the IC79&IC86 analysis (black). The IC59 analysis is more sensitive at lower energies (< 100 TeV), while for higher energies, the IC79&IC86 analysis has a better sensitivity. The peak at E ≈ 6.3 PeV is the Glashow resonance (see [70]). The data points of the IC79&IC86 analysis are taken from Aartsen et al. [1].*

Comparing the astrophysical flux normalization of $E^2\Phi_{astro} = (3.6\pm1.2)\cdot10^{-8}\mathrm{GeVs}^{-1}\mathrm{sr}^{-1}\mathrm{cm}^{-2}$ (60 TeV $< E <$ 2 PeV) from equation 6.22 with the upper limit derived for hypothesis H0 from this analysis $E^2\Phi^{H0}_{astro,\,ul} = 1.7\cdot10^{-8}\mathrm{GeVs}^{-1}\mathrm{sr}^{-1}\mathrm{cm}^{-2}$ in the energy range of 20 TeV $\leq E \leq$ 3.0 PeV (90% confidence level, see section 6.2.1, equation 6.19), there is a small disagreement. However, the upper limit $E^2\Phi^{H2}_{astro,\,ul} = 3.2\cdot10^{-8}\mathrm{GeVs}^{-1}\mathrm{sr}^{-1}\mathrm{cm}^{-2}$ derived for hypothesis H2, which presents a more realistic scenario with contraints on the normalizations for the conventional and prompt atmospheric neutrinos (see section 6.2.3), lies within the error range of the IC79&IC86 flux normalization measurement.

6.3.3 Comparison of the observed energies to other IceCube data sets

A previous analysis [5] found 4 neutrino candidate events above an energy threshold of 100 TeV. One may ask why no higher energy events were found in this analysis. In order to quantify the probability to find only events with energies smaller than 100 TeV, a Monte Carlo simulation was performed.
Assuming that the highest energy events would be obtained from the astrophysical neutrino flux, one can simulate their energy distribution using the effective area (see figure 6.16). In the 335 days of this analysis, one would expect about 12 neutrino events in the energy range

from $E = 10$ TeV up to $E = 100$ PeV using the astrophysical neutrino flux from [1]. Figure 6.17 shows the probability density function (p.d.f.) of the fractional differential event number dN/dE.

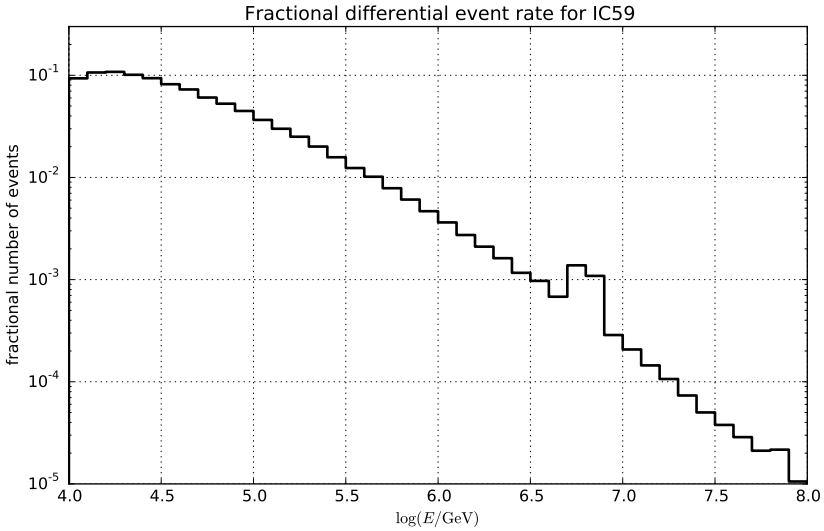

Figure 6.17: *The probability density function of astrophysical neutrino events as a function of energy, using the effective areas of this analysis (see figure 6.16) and the astrophysical neutrino flux measured by Aartsen et al. [1].*

Event samples were drawn according to the p.d.f. The number of events k in each sample was drawn from a Poisson distribution $P(k, \lambda)$ with a mean $\lambda = 12$. Then for each event in the sample of length k, an energy was drawn from the pdf. This was done $1 \cdot 10^7$ times and the number of cases when all events had energies smaller than 100 TeV was counted. Varying the seeds and the number of simulations showed that the result stays constant for $1 \cdot 10^7$ simulation runs. The probability to measure only events with energies below 100 TeV is about 1% for the astrophysical neutrino spectrum measured in [1]. Taking into account the error on the flux measurement, the probability increases from 1% to 4%.
Interestingly, a recent IceCube analysis [7] has measured a slightly different astrophysical neutrino spectrum for a lower energy threshold, resulting in an all-flavor flux of

$$\Phi_\nu(E) = 6.18^{+1.05}_{-0.78} \cdot 10^{-18} (E/10^5 \mathrm{GeV})^{-2.46 \pm 0.12} \,\mathrm{GeV s^{-1} sr^{-1} cm^{-2}}, \tag{6.23}$$

in the energy range of 25 TeV $\leq E \leq$ 1.4 PeV. This energy range is similar to the energy range of the analysis presented here. Using this astrophysical neutrino flux results in a probability of about 1% to obtain an event sample in which all events have energies less than 100 TeV. Taking into account the quoted errors of the flux measurement, the probability can increase from 1% up to 21%. Due to the statistics of small numbers it appears plausible that only events with energies below 100 TeV have been found in the analysis presented in this

thesis.

6.3.4 Conclusion

In the IC59 data sample, an excess of data events over the total simulated background was found. To further study this excess, a likelihood fit was applied to the data sample, which is able to take into account the different energy spectra of the signal and background contributions. No astrophysical neutrino flux is necessary to explain the excess in the data. An upper limit of the astrophysical neutrino flux of $E^2\Phi^{H0}_{astro,\,ul} = 1.7 \cdot 10^{-8}$ GeVs^{-1}sr^{-1}cm^{-2} in the energy range 20 TeV $\leq E \leq$ 3.0 PeV is calculated for hypothesis H0 (see section 6.2.1). This limit is lower than prior limits of IceCube analyses [113, 118] and lies below the Waxman-Bahcall bound $E^2\Phi_{WB} \lesssim 3.4 \cdot 10^{-8}$ GeVs^{-1}sr^{-1}cm^{-2}. If the normalizations of the conventional and prompt atmospheric neutrino flux are contraint like in hypothesis H2, which is a more realistic scenario, the upper limit on the astrophysical neutrino flux is $E^2\Phi^{H2}_{astro,\,ul} = 3.2 \cdot 10^{-8}$ GeVs^{-1}sr^{-1}cm^{-2}, which is compatible with the flux finally measured by the IC79&IC86 analysis.
The excess of data events in this analysis is absorbed into higher normalizations of the conventional prompt atmospheric neutrino flux. The IC59 data sample is not able to resolve the ambiguities between the spectra of the conventional and prompt atmospheric neutrino flux and the astrophysical neutrino flux. This can be understood by the rather small energies $E <$ 100 TeV of the data events found. An excess of data events at energies of about several hundreds of TeV is challenging to explain without an astrophysical neutrino flux component. Using a recent IceCube measurement of the astrophysical neutrino flux, it was shown that the probabilty to only find neutrino events with energies below 100 TeV, can be up to 21%. Figure 6.18 shows the upper limit of this thesis in comparison to other upper limits and measurements of the astrophysical neutrino flux from IceCube. Although this analysis did not detect a diffuse astrophysical neutrino flux, it provided a better upper limit compared to prior analyses. Furthermore, it contributes events to the overall IceCube neutrino candidate event collection, which are used in the global likelihood fit analysis to constrain the astrophysical neutrino spectrum as well as the the prompt atmospheric neutrino flux.

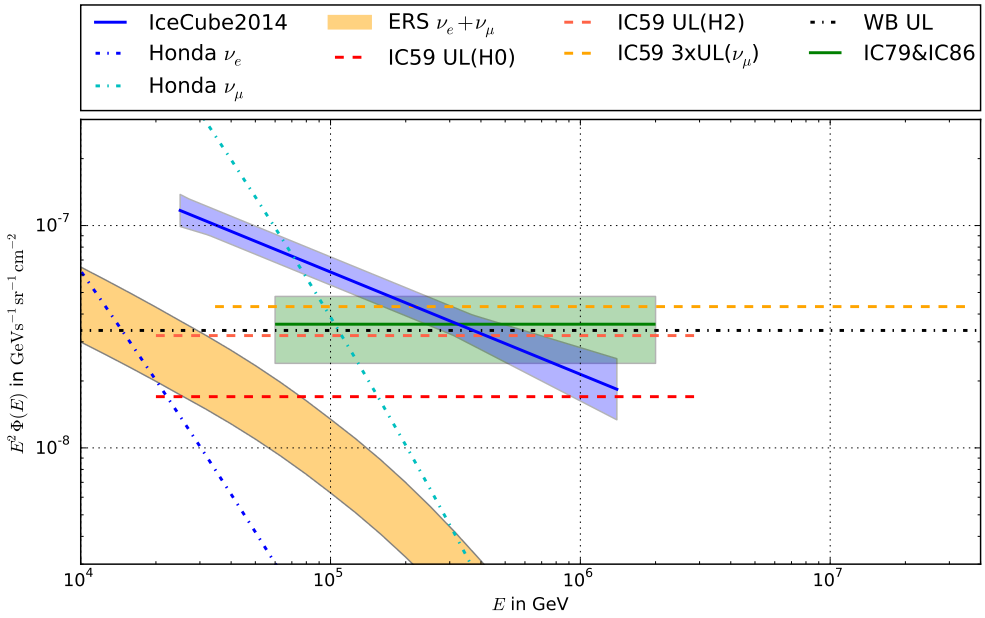

Figure 6.18: *Astrophysical neutrino flux upper limits and measurements. All fluxes are multiplied with E^2. The black dash-dot line shows the all-flavor Waxman-Bahcall upper limit [129] (see section 2.2.3). The blue and cyan dash-dot lines show the conventional atmospheric electron and muon neutrino flux, respectively, according to [82] with the modification from [62] (see sections 2.2.4 and 2.2.4). The orange area shows the lower and upper model prediction for the prompt atmospheric neutrino flux of the sum of electron and muon neutrinos, according to [55] with the modification from [62] (see section 2.2.4). The red dashed line and the pale red dashed line show the all-flavor upper limit on the astrophysical neutrino flux of this thesis for hypothesis H0 and hypothesis H2, respectively. The orange dashed line shows the muon neutrino upper limit of [117, 118], which is multiplied by 3 to convert it into an all-flavor upper limit. The green and the blue solid lines show the measurements of the astrophysical neutrino flux of the IC79&IC86 [1] (see section 6.3.1) and the IceCube2014 [7] analysis, respectively. The green and blue shaded areas show the uncertainties of the measured spectra.*

7 Summary

This thesis presented a search for the diffuse astrophysical neutrino flux ($d\Phi/dE = N_0 \cdot E^{-2}$) in 335 days of IceCube data from May 2009 to May 2010. IceCube is a 1 km^3 neutrino detector located at South Pole, which was completed at the end of 2010. IceCube consists of 86 strings frozen into the Antarctic ice at a depth from 1500 m to 2500 m, each equipped with 60 Digital Optical Photomultipliers (DOMs). When the data for this analysis was taken, the IceCube detector was still in construction and consisted only of 59 strings (IC59).
Neutrinos interacting with nuclei in the ice produce charged particles, which emit Cherenkov light. Based on the Cherenkov light recorded by the DOMs, the vertex of the neutrino interaction and the neutrino energy can be estimated. The analysis is sensitive to neutral current interaction of all three neutrino flavors, and charged-current interactions of electron and tau neutrinos. These interactions in the detector create so-called cascade events, which have a spherical hit patern. If a cascade is fully contained in the instrumented volume, it has a good energy resolution, since all the energy is deposited in the detector.
The expected neutrino signal is small, of the order of 10 μHz at Trigger Level. It is hidden in the large background of atmospheric muons, which results in a data rate of about 1.6 kHz in the detector at Trigger Level. These muons are created in the interactions of cosmic rays with the atmosphere. As they pass through the detector, they emit Cherenkov light, resulting in characteristic muon tracks. The differences in the hit patterns and other event properties are used to reduce the large muon background of the analysis.
In addition to muons, atmospheric neutrinos are also created in the interaction of cosmic rays with the atmosphere. The decay of the generated pions and kaons creates the so-called conventional atmospheric neutrino flux. The prompt atmospheric neutrino flux originates from the decay of hadrons containing charm quarks. They can only be distinguished from the astrophysical neutrino signal due to their different energy spectra.
The signal and background events are simulated within the IceCube simulation framework. In order to avoid a confirmation bias, the analysis was developed on a 10% subsample of about 34 days of the full data sample.
Atmospheric muons which undergo a catastrophic bremsstrahlung loss in the detector can appear like neutrino interactions if their muon tracks are too weak to be identified. This can happen for example, if they move into the detector over a corner or parallel to a detector boundary. Since these events are indistinguishable from neutrino interations, they must be rejected as well as possible. Therefore, a special event selection (Level 4) was developed in this analysis to remove these ambiguous events. It is built upon earlier common IceCube event selection levels. The Level 4 also contains additional quality selections on the events. The Level 5 event selection was then developed to reduce the remaining atmospheric muon background as much as possible in order to obtain a sample in which the number of expected

astrophysical neutrino events is about the same or larger than the number of background events. To obtain a reliable prediction of the number of remaining atmospheric muons on final level, a huge simulation sample of atmospheric muons is necessary. Using a new method for the simulation of atmopsheric muons (Five component Corsika) and an optimized scheme to generate it, this analysis was the first to achieve a livetime of more than one year of simulated atmospheric muon events with energies $E \geq 10$ TeV.
After the Level 5, a cut and count analysis based on an additional energy cut of $E > 38$ TeV was applied to the remaining 90% of the IC59 data sample. In the full data sample, 8 events with energies between 39 TeV and 67 TeV were found, while the number of predicted background events from the simulation was $N = 3.6 \pm 0.3$.
To further investigate this small excess, a maximum likelihood fit, containing templates for the different expected background fluxes, signal flux and nuisance parameters, e.g. the energy scale, was applied to the Level 5 event selection for an energy threshold of 10 TeV. No astrophysical neutrino flux was required to describe the excess in the data. Instead, it was absorbed by higher flux normalizations of the conventional and prompt atmospheric neutrino flux. A 90% confidence level upper limit on the all-flavor astrophysical neutrino flux was calculated to be $E^2\Phi_{astro,\,ul} = 1.7 \cdot 10^{-8}\mathrm{GeVs}^{-1}\mathrm{sr}^{-1}\mathrm{cm}^{-2}$ in the energy range of 20 TeV $\leq E \leq$ 3.0 PeV. This limit is lower than prior limits of other IceCube analyses. If the normalizations of the conventional and prompt atmospheric neutrino flux are contraint, which is a more realistic scenario, the upper limit of the astrophysical neutrino flux is $E^2\Phi_{astro,\,ul} = 3.2 \cdot 10^{-8}$ $\mathrm{GeVs}^{-1}\mathrm{sr}^{-1}\mathrm{cm}^{-2}$, which is compatible with the astrophysical neutrino flux finally detected by IceCube.
Although this analysis did not detect a diffuse astrophysical neutrino flux, it contributes events to the overall IceCube neutrino candidate event collection, which is used in the global likelihood fit analysis to further constrain the astrophysical neutrino spectrum as well as the the prompt atmospheric neutrino flux.

Bibliography

[1] Aartsen, M., et al., 2013; 'Evidence for High-Energy Extraterrestrial Neutrinos at the IceCube Detector'. *Science*, vol. 342:1242856. DOI:10.1126/science.1242856

[2] Aartsen, M., et al., 2014; 'Determining neutrino oscillation parameters from atmospheric muon neutrino disappearance with three years of IceCube DeepCore data'. *ArXiv e-prints*. Arxiv:1410.7227

[3] Aartsen, M., et al., 2014; 'Observation of High-Energy Astrophysical Neutrinos in Three Years of IceCube Data'. *Phys.Rev.Lett.*, vol. 113:101101. DOI:10.1103/PhysRevLett.113.101101

[4] Aartsen, M., et al., 2014; 'Search for a diffuse flux of astrophysical muon neutrinos with the IceCube 59-string configuration'. *Phys.Rev.*, vol. D89:062007. DOI:10.1103/PhysRevD.89.062007

[5] Aartsen, M., et al., 2014; 'Search for neutrino-induced particle showers with IceCube-40'. *Phys. Rev. D*, vol. 89:102001. DOI:10.1103/PhysRevD.89.102001

[6] Aartsen, M., et al., 2014; 'Searches for Extended and Point-like Neutrino Sources with Four Years of IceCube Data'. *The Astrophysical Journal*, vol. 796(2):109. DOI:10.1088/0004-637X/796/2/109

[7] Aartsen, M., et al., 2015; 'Atmospheric and astrophysical neutrinos above 1 TeV interacting in IceCube'. *Phys.Rev.*, vol. D91(2):022001. DOI:10.1103/PhysRevD.91.022001

[8] Abbasi, R., Abdou, Y., Abu-Zayyad, T., et al., 2010; 'Calibration and characterization of the IceCube photomultiplier tube'. *Nuclear Instruments and Methods in Physics Research A*, vol. 618:139. DOI:10.1016/j.nima.2010.03.102

[9] Abbasi, R., Abdou, Y., Abu-Zayyad, T., et al., 2011; 'Measurement of the atmospheric neutrino energy spectrum from 100 GeV to 400 TeV with IceCube'. *Physical Review D*, vol. 83(1):012001. DOI:10.1103/PhysRevD.83.012001

[10] Abbasi, R., Abdou, Y., Abu-Zayyad, T., et al., 2011; 'Search for neutrino-induced cascades with five years of AMANDA data'. *Astropart.Phys.*, vol. 34:420. DOI:10.1016/j.astropartphys.2010.10.007

[11] Abbasi, R., Abdou, Y., Abu-Zayyad, T., et al., 2012; 'The design and performance of IceCube DeepCore'. *Astroparticle Physics*, vol. 35(10):615 . DOI:10.1016/j.astropartphys.2012.01.004

[12] Abbasi, R., et al., 2009; 'The IceCube Data Acquisition System: Signal Capture, Digitization, and Timestamping'. *Nucl.Instrum.Meth.*, vol. A601:294. DOI:10.1016/j.nima.2009.01.001

[13] Abbasi, R., et al., 2011; 'First search for atmospheric and extraterrestrial neutrino-induced cascades with the IceCube detector'. *Phys.Rev.*, vol. D84:072001. DOI:10.1103/PhysRevD.84.072001

[14] Abbasi, R., et al., 2013; 'IceTop: The surface component of IceCube'. *Nucl.Instrum.Meth.*, vol. A700:188. DOI:10.1016/j.nima.2012.10.067

[15] Abraham, J., et al., 2004; 'Properties and performance of the prototype instrument for the Pierre Auger Observatory'. *Nucl.Instrum.Meth.*, vol. A523:50. DOI:10.1016/j.nima.2003.12.012

[16] Achterberg, A., Ackermann, M., Adams, J., et al., 2006; 'First year performance of the IceCube neutrino telescope'. *Astroparticle Physics*, vol. 26(3):155 . DOI:10.1016/j.astropartphys.2006.06.007

[17] Ackermann, M., Ahrens, J., Bai, X., et al., 2006; 'Optical properties of deep glacial ice at the South Pole'. *Journal of Geophysical Research (Atmospheres)*, vol. 111(D10):D13203. DOI:10.1029/2005JD006687

[18] Adriani, O., Barbarino, G., Bazilevskaya, G., et al., 2014; 'Measurement of boron and carbon fluxes in cosmic rays with the PAMELA experiment'. *Astrophys.J.*, vol. 791:93. DOI:10.1088/0004-637X/791/2/93

[19] Adriani, O., et al., 2011; 'PAMELA Measurements of Cosmic-ray Proton and Helium Spectra'. *Science*, vol. 332:69. DOI:10.1126/science.1199172

[20] Ageron, M., et al., 2011; 'ANTARES: the first undersea neutrino telescope'. *Nucl.Instrum.Meth.*, vol. A656:11. DOI:10.1016/j.nima.2011.06.103

[21] Ahrens, J., et al., 2004; 'Muon track reconstruction and data selection techniques in AMANDA'. *Nucl.Instrum.Meth.*, vol. A524:169. DOI:10.1016/j.nima.2004.01.065

[22] Amenomori, M., Ayabe, S., Cui, S. W., et al., 2003; 'Multi-TeV Gamma-Ray Flares from Markarian 421 in 2000 and 2001 Observed with the Tibet Air Shower Array'. *The Astrophysical Journal*, vol. 598(1):242. DOI:10.1086/378350

[23] Andres, E., Askebjer, P., Bai, X., et al., 2001; 'Observation of high-energy neutrinos using Cherenkov detectors embedded deep in Antarctic ice'. *Nature*, vol. 410:441. DOI:10.1038/35068509

[24] Antoni, T., et al., 2003; 'The Cosmic ray experiment KASCADE'. *Nucl.Instrum.Meth.*, vol. A513:490. DOI:10.1016/S0168-9002(03)02076-X

[25] Apel, W., Arteaga, J., Badea, A., et al., 2010; 'The KASCADE-Grande experiment'. *Nucl.Instrum.Meth.*, vol. A620:202. DOI:10.1016/j.nima.2010.03.147

[26] Arnett, W., Bahcall, J., Kirshner, R., et al., 1989; 'Supernova 1987A'. *Ann. Rev. Astron. Astrophys.*, vol. 27:629. DOI:10.1146/annurev.aa.27.090189.003213

[27] Arons, J., 2003; 'Magnetars in the metagalaxy: an origin for ultrahigh-energy cosmic rays in the nearby universe'. *Astrophys.J.*, vol. 589:871. DOI:10.1086/374776

[28] Barger, V., Fu, L., Learned, J., et al., 2014; 'Glashow resonance as a window into cosmic neutrino sources'. *Phys.Rev.*, vol. D90(12):121301. DOI:10.1103/PhysRevD.90.121301

[29] Berezhnev, S., Besson, D., Budnev, N., et al., 2012; 'The Tunka-133 EAS Cherenkov light array: status of 2011'. *Nucl.Instrum.Meth.*, vol. A692:98. DOI:10.1016/j.nima.2011.12.091

[30] Berghaus, P., 2011; 'Atmospheric Muon Spectrum from Catastrophic Energy Losses in IceCube'. *International Cosmic Ray Conference*, vol. 4:103. DOI:10.7529/ICRC2011/V04/0085

[31] Berghaus, P., 2014; 'IC79 Atmospheric Muons and Event Characteristics'. Private communication

[32] Berghaus, Patrick, 2013; 'Atmospheric Muons as IceCube Signal'. *EPJ Web of Conferences*, vol. 52:09006. DOI:10.1051/epjconf/20125209006

[33] Beringer, J., et al., 2012; 'Review of Particle Physics: Atomic Nuclear Properties'. *Phys.Rev.*, vol. D86:010001. URL:http://pdg.lbl.gov/2012/AtomicNuclearProperties/HTML_PAGES/325.html

[34] Beringer, J., et al., 2012; 'Review of Particle Physics (RPP)'. *Phys.Rev.*, vol. D86:305. DOI:10.1103/PhysRevD.86.010001

[35] Biagi, S., 2013; 'Updated limits on diffuse fluxes of cosmic neutrinos with 2008-2011 ANTARES data'. *ArXiv e-prints*. Arxiv:1305.6442

[36] Bionta, R. M., Blewitt, G., Bratton, C. B., et al., 1987; 'Observation of a neutrino burst in coincidence with supernova 1987A in the Large Magellanic Cloud'. *Phys. Rev. Lett.*, vol. 58:1494. DOI:10.1103/PhysRevLett.58.1494

[37] Blümer, J., Engel, R., Hoerandel, J. R., 2009; 'Cosmic rays from the knee to the highest energies'. *Progress in Particle and Nuclear Physics*, vol. 63(2):293 . DOI:10.1016/j.ppnp.2009.05.002

[38] Boettcher, M., 2010; 'Models for the Spectral Energy Distributions and Variability of Blazars'. *ArXiv e-prints*. Arxiv:1006.5048

[39] Boyer, J., Knapp, B., Mannel, E., et al., 2002; 'FADC-based DAQ for HiRes Fly's Eye'. *Nucl.Instrum.Meth.*, vol. A482:457. DOI:10.1016/S0168-9002(01)01517-0

[40] Boyle, P., 2008; 'The Elemental Composition of High-Energy Cosmic Rays: Measurements with TRACER'. *Mod.Phys.Lett.*, vol. A23:2031. DOI:10.1142/S0217732308028260

[41] Cardillo, M., Tavani, M., Giuliani, A., 2014; 'The origin of Cosmic-Rays from SNRs: confirmations and challenges after the first direct proof'. *Nucl.Phys.Proc.Suppl.*, vol. B256-257:65. DOI:10.1016/j.nuclphysbps.2014.10.007

[42] Chirkin, D., Rhode, W., 2004; 'Muon Monte Carlo: A High-precision tool for muon propagation through matter'. *ArXiv e-prints*. Arxiv:hep-ph/0407075

[43] Conrad, J. M., Shaevitz, M. H., Bolton, T., 1998; 'Precision measurements with high-energy neutrino beams'. *Rev.Mod.Phys.*, vol. 70:1341. DOI:10.1103/RevModPhys.70.1341

[44] Consolandi, C., 2014; 'Primary Cosmic Ray Proton Flux Measured by AMS-02'. *ArXiv e-prints*. Arxiv:1402.0467

[45] Corsika Software, Retrieved 2014; 'Corsika Software'. URL:https://web.ikp.kit.edu/corsika/index.html

[46] Corsika User's Guide, Retrieved 2014; 'Corsika User's Guide'. URL:https://web.ikp.kit.edu/corsika/usersguide/corsika_tech.html

[47] Cowan, C., Reines, F., Harrison, F., et al., 1956; 'Detection of the free neutrino: A Confirmation'. *Science*, vol. 124:103. DOI:10.1126/science.124.3212.103

[48] Cowen, D., 2007; 'Tau neutrinos in IceCube'. *J.Phys.Conf.Ser.*, vol. 60:227. DOI:10.1088/1742-6596/60/1/048

[49] D'Agostino, M. V., 2009; *First Evidence For Atmospheric Neutrino-Induced Cascades with the IceCube Detector*. Ph.D. thesis, University of California, Berkeley. URL:http://arxiv.org/abs/0910.2555

[50] Danby, G., Gaillard, J., Goulianos, K. A., et al., 1962; 'Observation of High-Energy Neutrino Reactions and the Existence of Two Kinds of Neutrinos'. *Phys.Rev.Lett.*, vol. 9:36. DOI:10.1103/PhysRevLett.9.36

[51] Davis, R., Harmer, D. S., Hoffman, K. C., 1968; 'Search for Neutrinos from the Sun'. *Phys. Rev. Lett.*, vol. 20:1205. DOI:10.1103/PhysRevLett.20.1205

[52] DONUT Collaboration, 2001; 'Observation of tau neutrino interactions'. *Physics Letters B*, vol. 504:218. DOI:10.1016/S0370-2693(01)00307-0

[53] DONUT collaboration, Retrieved 2014; 'DONUT collaboration'. URL:http://www-donut.fnal.gov

[54] Dziewonski, A., 1989; *Earth Structure, Global*. Van Nostrand Reinhold, New York. Published in The Encyclopedia of Solid Earth Geophysics, edited by David E. James

[55] Enberg, R., Reno, M. H., Sarcevic, I., 2008; 'Prompt neutrino fluxes from atmospheric charm'. *Phys.Rev.*, vol. D78:043005. DOI:10.1103/PhysRevD.78.043005

[56] Fabjan, C., Ludlam, T., 1982; 'Calorimetry in High-energy Physics'. *Ann.Rev.Nucl.Part.Sci.*, vol. 32:335. DOI:10.1146/annurev.ns.32.120182.002003

[57] Feldman, G. J., Cousins, R. D., 1998; 'A Unified approach to the classical statistical analysis of small signals'. *Phys.Rev.*, vol. D57:3873. DOI:10.1103/PhysRevD.57.3873

[58] Fermi, E., 1949; 'On the Origin of the Cosmic Radiation'. *Phys. Rev.*, vol. 75:1169. DOI:10.1103/PhysRev.75.1169

[59] Fermín, I. J. T., 2002; *Search for High Energy Neutrino Induced Cascades with the AMANDA-B10 Detector*. Ph.D. thesis, University of Pennsylvania. URL:http://repository.upenn.edu/dissertations/AAI3043964

[60] Gaisser, T. K., 2003; 'Atmospheric neutrino fluxes'. *Nucl.Phys.Proc.Suppl.*, vol. 118:109. DOI:10.1016/S0920-5632(03)01309-4

[61] Gaisser, T. K., 2007; 'Atmospheric Neutrinos'. *AIP Conf.Proc.*, vol. 944:140. DOI:10.1063/1.2818541

[62] Gaisser, T. K., 2012; 'Spectrum of cosmic-ray nucleons, kaon production, and the atmospheric muon charge ratio'. *Astropart.Phys.*, vol. 35:801. DOI:10.1016/j.astropartphys.2012.02.010

[63] Gaisser, T. K., Klein, S. R., 2014; 'A new contribution to the conventional atmospheric neutrino flux'. *Astropart.Phys.*, vol. 64:13. DOI:10.1016/j.astropartphys.2014.10.006

[64] Gaisser, T. K., Stanev, T., 2012; 'Neutrinos and cosmic rays'. *Astroparticle Physics*, vol. 39:120. DOI:10.1016/j.astropartphys.2012.08.004

[65] Gandhi, R., Quigg, C., Reno, M. H., et al., 1996; 'Ultrahigh-energy neutrino interactions'. *Astropart.Phys.*, vol. 5:81. DOI:10.1016/0927-6505(96)00008-4

[66] Gandhi, R., Quigg, C., Reno, M. H., et al., 1998; 'Neutrino interactions at ultrahigh energies'. *Phys. Rev. D*, vol. 58:093009. DOI:10.1103/PhysRevD.58.093009

[67] Gazizov, A., Kowalski, M. P., 2005; 'ANIS: High energy neutrino generator for neutrino telescopes'. *Comput.Phys.Commun.*, vol. 172:203. DOI:10.1016/j.cpc.2005.03.113

[68] Gerhardt, L., 2005; 'Sensitivity of AMANDA-II to UHE neutrinos'. *ArXiv e-prints*. International Conference on Cosmic Rays. URL:http://icrc2005.tifr.res.in/htm/Vol-Web/Vol-15/15111-usa-gerhardt-L-abs1-og25-oral.pdf

[69] Gerhardt, L., Klein, S. R., 2010; 'Electron and Photon Interactions in the Regime of Strong LPM Suppression'. *Phys.Rev.*, vol. D82:074017. DOI:10.1103/PhysRevD.82.074017

[70] Glashow, S. L., 1960; 'Resonant Scattering of Antineutrinos'. *Phys. Rev.*, vol. 118:316. DOI:10.1103/PhysRev.118.316

[71] Gonzalez-Garcia, M., Maltoni, M., Schwetz, T., 2014; 'Updated fit to three neutrino mixing: status of leptonic CP violation'. *JHEP*, vol. 1411:052. DOI:10.1007/JHEP11(2014)052

[72] Greisen, K., 1966; 'End to the Cosmic-Ray Spectrum?' *Phys. Rev. Lett.*, vol. 16:748. DOI:10.1103/PhysRevLett.16.748

[73] Gribov, V., Pontecorvo, B., 1969; 'Neutrino astronomy and lepton charge'. *Physics Letters B*, vol. 28(7):493 . DOI:10.1016/0370-2693(69)90525-5

[74] Haino, S., Sanuki, T., Abe, K., et al., 2004; 'Measurements of primary and atmospheric cosmic-ray spectra with the BESS-TeV spectrometer'. *Phys.Lett.*, vol. B594:35. DOI:10.1016/j.physletb.2004.05.019

[75] Hanson, K., Tarasova, O., 2006; 'Design and production of the IceCube digital optical module'. *Nucl.Instrum.Meth.*, vol. A567:214. DOI:10.1016/j.nima.2006.05.091

[76] Hess, V., 1912; 'Ueber die Bedeutung der durchdringenden Strahlung bei sieben Freiluftballonfahrten'. *Phys.Zeitschri.* URL:http://www.mpi-hd.mpg.de/hfm/HESS/public/HessArticle.pdf

[77] Hickford, S. V., 2012; *A Cascade Analysis for the IceCube Neutrino Telescope*. Ph.D. thesis, University of Canterbury. URL:http://ir.canterbury.ac.nz/handle/10092/10014

[78] Hill, G. C., Rawlins, K., 2003; 'Unbiased cut selection for optimal upper limits in neutrino detectors: The Model rejection potential technique'. *Astropart.Phys.*, vol. 19:393. DOI:10.1016/S0927-6505(02)00240-2

[79] Hillas, A. M., 1984; 'The Origin of Ultra-High-Energy Cosmic Rays'. *Ann. Rev. Astron. Astrophys.*, vol. 22:425. DOI:10.1146/annurev.aa.22.090184.002233

[80] Hirata, K., Kajita, T., Koshiba, M., et al., 1987; 'Observation of a neutrino burst from the supernova SN1987A'. *Phys. Rev. Lett.*, vol. 58:1490. DOI:10.1103/PhysRevLett.58.1490

[81] Hoerandel, J. R., 2003; 'On the knee in the energy spectrum of cosmic rays'. *Astropart.Phys.*, vol. 19:193. DOI:10.1016/S0927-6505(02)00198-6

[82] Honda, M., Kajita, T., Kasahara, K., et al., 2007; 'Calculation of atmospheric neutrino flux using the interaction model calibrated with atmospheric muon data'. *Phys.Rev.*, vol. D75:043006. DOI:10.1103/PhysRevD.75.043006

[83] Hulth, P., et al., 1996; 'The AMANDA experiment'. *ArXiv e-prints*. Arxiv:astro-ph/9612068

[84] IceCube Collaboration, Aartsen, M. G., Abbasi, R., et al., 2013; 'Measurement of South Pole ice transparency with the IceCube LED calibration system'. *ArXiv e-prints*. Arxiv:1301.5361

[85] ICRC, 2011; *Study of South Pole ice transparency with IceCube flashers*. Papers submitted by the IceCube Collaboration to the 32nd International Cosmic Ray Conference, Beijing 2011/ part VI. URL:http://arxiv.org/abs/1111.2731

[86] K. Gaisser, T., 1990; *Cosmic Rays And Particle Physics*. Cambridge University Press

[87] Kahana, S., Cooperstein, J., Baron, E., 1987; 'Neutrinos from supernova 1987A'. *Physics Letters B*, vol. 196(3):259 . DOI:10.1016/0370-2693(87)90727-1

[88] Kampert, K.-H., 2013; 'Ultrahigh-Energy Cosmic Rays: Results and Prospects'. *Braz.J.Phys.*, vol. 43:375. DOI:10.1007/s13538-013-0150-1

[89] Kappes, A., Hinton, J., Stegmann, C., et al., 2007; 'Potential Neutrino Signals from Galactic Gamma-Ray Sources'. *Astrophys.J.*, vol. 656:870. DOI:10.1086/508936, 10.1086/518161

[90] Katz, U. F., Spiering, C., 2012; 'High-energy neutrino astrophysics: Status and perspectives'. *Progress in Particle and Nuclear Physics*, vol. 67:651. DOI:10.1016/j.ppnp.2011.12.001

[91] Kiryluk, J., 2014; 'IC22 results extraterrestrial neutrino-induced cascades'. Private communication

[92] Kistler, M. D., Beacom, J. F., 2006; 'Guaranteed and Prospective Galactic TeV Neutrino Sources'. *Phys.Rev.*, vol. D74:063007. DOI:10.1103/PhysRevD.74.063007

[93] Kotera, K., Olinto, A. V., 2011; 'The Astrophysics of Ultrahigh-Energy Cosmic Rays'. *Annual Review of Astronomy and Astrophysics*, vol. 49:119. DOI:10.1146/annurev-astro-081710-102620

[94] Kowalski, M. P., 2003; *Search for Neutrino-Induced Cascades with the AMANDA-II Detector*. Ph.D. thesis, Humboldt-Universität zu Berlin. URL:http://edoc.hu-berlin.de/dissertationen/kowalski-marek-paul-2004-01-13

[95] Landau, L., Pomeranchuk, I., 1953; 'Limits of applicability of the theory of bremsstrahlung electrons and pair production at high-energies'. *Dokl.Akad.Nauk Ser.Fiz.*, vol. 92:535

[96] Lundberg, J., Miočinović, P., Woschnagg, K., et al., 2007; 'Light tracking through ice and water-Scattering and absorption in heterogeneous media with Photonics'. *Nuclear Instruments and Methods in Physics Research Section A: Accelerators, Spectrometers, Detectors and Associated Equipment*, vol. 581(3):619 . DOI:http://dx.doi.org/10.1016/j.nima.2007.07.143

[97] M. Lesiak-Bzdak and A. Stoessl for the IceCube Collaboration, 2013; *Search for extraterrestrial neutrino-induced cascades using IceCube 79-strings*. Papers submitted by the IceCube Collaboration to the 33nd International Cosmic Ray Conference, Rio de Janeiro. URL:http://arxiv.org/abs/1309.7003

[98] M.Ackermann, et al., 2006; 'Optical properties of deep glacial ice at the South Pole'. *Journal of Geophysical Research*, vol. 111(D13):D13203+. DOI:10.1029/2005jd006687

[99] Maestro, P., Ahn, H. S., Allison, P., et al., 2009; 'Measurements of cosmic-ray energy spectra with the 2^{nd} CREAM flight'. *Nuclear Physics B Proceedings Supplements*, vol. 196:239. DOI:10.1016/j.nuclphysbps.2009.09.045

[100] Maurin, D., Melot, F., Taillet, R., 2014; 'CRDB: a database of charged cosmic rays'. *Astron.Astrophys.*, vol. 569:A32. DOI:10.1051/0004-6361/201321344

[101] Middell, E., 2008; *Reconstruction of Cascade-Like Events in IceCube*. Master's thesis, Humboldt-Universität zu Berlin

[102] Middell, E., 2014; 'Effective area values of IC40'. Private communication

[103] Middell, E., 2014; 'Neutrino interaction event pattern'. Private communication

[104] Middell, E., Panknin, S., 2009; *Request for the Cascade Online Filter*. IceCube internal document, number 52559

[105] Migdal, A. B., 1956; 'Bremsstrahlung and Pair Production in Condensed Media at High Energies'. *Phys. Rev.*, vol. 103:1811. DOI:10.1103/PhysRev.103.1811

[106] Mohrmann, L., 2012; 'Background Monte-Carlo Production Studies'. Private communication

[107] Mohrmann, L., 2014; 'Muon background estimation for the Global Diffuse Likelihood Fit'. Private communication

[108] Mohrmann, L., Middell, E., 2012; 'Background Monte-Carlo Production Studies'. Private communication

[109] Muller, D., 2012; 'Direct observations of galactic cosmic rays'. *Eur.Phys.J.*, vol. H37:413. DOI:10.1140/epjh/e2012-30017-2

[110] Nunokawa, H., Parke, S. J., Valle, J. W., 2008; 'CP Violation and Neutrino Oscillations'. *Prog.Part.Nucl.Phys.*, vol. 60:338. DOI:10.1016/j.ppnp.2007.10.001

[111] Olive, K., et al., 2014; 'Review of Particle Physics'. *Chin.Phys.*, vol. C38:090001. DOI:10.1088/1674-1137/38/9/090001

[112] Pandel, D., 1996; *Bestimmung von Wasser- und Detektorparametern und Rekonstruction von Myonen bis 100 TeV mit dem Baikal-Neutrinoteleskop NT-72*. Master's thesis, Humboldt-Universität zu Berlin

[113] Panknin, S., 2011; *Search for Neutrino-Induced Cascade Events in the IceCube Detector*. Ph.D. thesis, Humboldt-Universität zu Berlin. URL:http://edoc.hu-berlin.de/frontpage.php/dissertationen/panknin-sebastian-2011-09-15

[114] pyminuit package documentation, Retrieved 2014; 'pyminuit package documentation'. URL:http://code.google.com/p/pyminuit

[115] Rädel, L., Wiebusch, C., 2013; 'Calculation of the Cherenkov light yield from electromagnetic cascades in ice with Geant4'. *Astroparticle Physics*, vol. 44:102. DOI:10.1016/j.astropartphys.2013.01.015

[116] S. Longair, M., 1992; *High Energy Astrophysics*. Cambridge University Press

[117] Schukraft, A., 2013; 'A view of prompt atmospheric neutrinos with IceCube'. *Nucl.Phys.Proc.Suppl.*, vol. 237-238:266. DOI:10.1016/j.nuclphysbps.2013.04.105

[118] Schukraft, A., Wiebusch, C., 2013; *Search for a diffuse flux of extragalactic neutrinos with the IceCube neutrino observatory*. Ph.D. thesis, RWTH Aachen University, Aachen. Ausgezeichnet mit dem Hertha-Sponer-Preis 2014 der Deutschen Physikalischen Gesellschaft.; Aachen, Techn. Hochsch., Diss., 2013. URL:http://publications.rwth-aachen.de/record/229692

[119] Simona Toscano, 2011; 'IC59 cascade Level 3 Credo script'. Private communication

[120] Simona Toscano, 2011; 'IceCube IC59 Cascade Level 3 cuts'. Private communication

[121] Spiering, C., 1999; 'Simulation and analysis methods for large neutrino telescopes. Workshop, Zeuthen, Germany, July 6-9, 1998'. *DESY Proceedings*

[122] Tamm, I., 1939; 'Radiation Emitted by Uniformly Moving Electrons'. *J. Phys. U.S.S.R.*

[123] TAUP, 2013; *Measurement of the diffuse neutrino flux by a global fit to multiple IceCube results*. 13th International Conference on Topics in Astroparticle and Underground Physics, TAUP2013

[124] Vannoni, G., Aharonian, F., Gabici, S., et al., 2009; 'Acceleration and radiation of ultra-high energy protons in galaxy clusters'. *ArXiv e-prints*. Arxiv:0910.5715

[125] Voigt, B., 2008; *Sensitivity of the IceCube detector for ultra-high energy electron-neutrino events*. Ph.D. thesis, Humboldt-Universität zu Berlin. URL:http://edoc.hu-berlin.de/dissertationen/voigt-bernhard-2008-07-16/PDF/voigt.pdf

[126] Waxman, E., 1995; 'Cosmological origin for cosmic rays above 10**19-eV'. *Astrophys.J.*, vol. 452:L1. DOI:10.1086/309715

[127] Waxman, E., 2011; 'High energy cosmic ray and neutrino astronomy'. *ArXiv e-prints*. Arxiv:1101.1155

[128] Waxman, E., 2013; 'IceCube's Neutrinos: The beginning of extra-Galactic neutrino astrophysics?' *ArXiv e-prints*. Arxiv:1312.0558

[129] Waxman, E., Bahcall, J. N., 1999; 'High-energy neutrinos from astrophysical sources: An Upper bound'. *Phys.Rev.*, vol. D59:023002. DOI:10.1103/PhysRevD.59.023002

[130] Wiebusch, C. H. V., 1995; *The Detection of faint light in deep underwater neutrino telescopes*. Ph.D. thesis, RWTH Aachen. URL:http://web.physik.rwth-aachen.de/ wiebusch/Publications/Various/phd.pdf

[131] Wilks, S. S., 1938; 'The Large-Sample Distribution of the Likelihood Ratio for Testing Composite Hypotheses'. *The Annals of Mathematical Statistics*, vol. 9(1):60. DOI:10.1214/aoms/1177732360

[132] Winter, K. (Ed.) , 1991; *W. Pauli, On the Earlier and More Recent History of the Neutrino (1957)*. Cambridge University Press

[133] Yoon, Y. S., Ahn, H. S., Allison, P. S., et al., 2011; 'Cosmic-ray Proton and Helium Spectra from the First CREAM Flight'. *The Astrophysical Journal*, vol. 728:122. DOI:10.1088/0004-637X/728/2/122

[134] Zandanel, F., Tamborra, I., Gabici, S., et al., 2014; 'High-energy gamma-ray and neutrino backgrounds from clusters of galaxies and radio constraints'. *ArXiv e-prints*. Arxiv:1410.8697

[135] Zatsepin, G. T., Kuz'min, V. A., 1966; 'Upper Limit of the Spectrum of Cosmic Rays'. *Soviet Journal of Experimental and Theoretical Physics Letters*, vol. 4:78. URL:https://inspirehep.net/record/49999

Selbständigkeitserklärung

Hiermit erkläre ich, die Dissertation selbstständig und nur unter Verwendung der angegebenen Hilfen und Hilfsmittel angefertigt zu haben. Ich habe mich nicht anderwärts um einen Doktorgrad in dem Promotionsfach beworben und besitze keinen entsprechenden Doktorgrad. Die Promotionsordnung der Mathematisch-Naturwissenschaftlichen Fakultät habe ich zur Kenntnis genommen.

Berlin, den 10. März 2015 Arne Schönwald